EXPERIMENTAL AND NUMERICAL INVESTIGATIONS ON THE DURABILITY AND FRACTURE MECHANICS OF THE BONDED SYSTEMS FOR MICROELECTRONICS APPLICATION

Shu Guo

Dissertation submitted to the faculty of the

Virginia Polytechnic Institute and State University

in partial fulfillment of the requirements for the degree of

Doctor of Philosophy

in

Engineering Mechanics

David A. Dillard, Chairman

Ramesh Batra

John G. Dillard

John J. Lesko

Thomas C. Ward

August, 2003

Blacksburg, Virginia

Keywords: thermal residual stresses, interfacial fracture energy, subcritical crack growth, temperature, diffusion, wedge test, epoxy-glass interface, adhesion, blister test, thin film, residual stress, delamination, bending, stretching, adhesion, fracture mechanics, coating, single-lap joint, boundary conditions, clamp, simply-supported, spacer.

EXPERIMENTAL AND NUMERICAL INVESTIGATIONS ON THE DURABILITY AND FRACTURE MECHANICS OF THE BONDED SYSTEMS FOR MICROELECTRONICS APPLICATION

Shu Guo

(ABSTRACT)

Water-assisted crack growth at an epoxy/glass interface was measured as a function of applied strain energy release rate, G, and temperature using a wedge test geometry. The specimens consist of two glass plates bonded with a thin layer of proprietary epoxy adhesive. The crack fronts along the epoxy/glass interfaces were measured using an optical stereomicroscope. The relationship between G and the debonding rate, v, can be measured using this method, and the threshold value of strain energy release rate, G_{th}, can be determined from the measured data. Two types of testing procedures were conducted in this study: *ex situ*, i.e., pre-conditioned wedge tests and *in situ* ones, in which wedges were applied before the specimens were submerged into water. A preliminary model was developed based on the thermal activation barrier concept, and allows the prediction of G_{th} for the temperatures beyond the testing region.

Changes in interfacial strain energy release rate caused by thermal residual stresses in a triple-layered specimen were analyzed in Chapter Three. The method is based on linear elastic fracture mechanics and simple beam theory. The curvature of a bimaterial strip was chosen to characterize the residual stress in the specimen, and the strain energy release rate, caused by both tensile and compressive residual stresses in the adhesive, was derived for an asymmetric double cantilever beam (ADCB) geometry. The contribution of the thermal residual and mechanical stress to the global energy release rate was analyzed. The thermally induced energy release rate, G_T, is found to be independent of crack length, but is a function of residual stress level and geometric and material parameters of the specimen.

The adhesion of films and coatings to rigid substrates is often measured using blister geometries, which are loaded either by an applied pressure or a central shaft. The measurement will be affected if there are residual stresses that make a contribution to the energy release rate. This effect is investigated using analytical solutions based on the principle of virtual displacements. A geometrically nonlinear finite element analysis is conducted for comparison. Furthermore, the relationships among strain energy release rate, load, deflection, and fracture radius are discussed in detail in Chapter Four. Both analytical solutions and numerical results reveal that uniform tensile residual stresses reduce a specimen's deflection if it experiences plate behavior under small loads. However, this effect diminishes when membrane behavior is dominant.

The mechanics of a single-lap joint with different boundary conditions subjected to tensile loading are investigated. Closed-form solutions are obtained for a specimen configuration considering different clamping methods. Based on the approach pioneered by Goland and Reissner, the solutions reported in this paper provide a simple but useful way to understand the effects of boundary conditions on this test geometry. The solutions in this study suggest that different grip configurations mainly affect the response of the specimens if the grip position is close to the joint edge or the loads are small. Generally, the influence caused by different gripping methods is only limited to the boundary region, and the behavior of the joint part subjected to tensile loading is almost the same as that for a simply-supported case.

ACKNOWLEDGEMENTS

I wish to express my sincere appreciation to my advisor, Dr. David A. Dillard for his valuable time, advice, guidance and support through my study and research at Virginia Tech and for his steadfast patience, understanding, and encouragement over the last four years.

I also wish to acknowledge my other committee members Dr. John G. Dillard, Dr. Thomas C. Ward, Dr. Jack Lesko, and Dr. Ramesh Batra for serving on my advisory committee, as well as for useful suggestions and guidance on my research work. appreciation is extended to Dr. Scott Case for his presence in my defense. I would like to thank Kai-tak Wan, and Dr. Shuangyan Xu in the Adhesion Mechanics Lab for useful discussions and great help in this work. Thanks also extends to Sandra Case and Emmett O'Brian for their help on specimen preparation and instructive discussions on polymer chemistry.

I would like to gratefully acknowledge the support from Hewlett Packard Company and the Center for Adhesive and Sealant Science at Virginia Tech for this research. I wish to thank Dr. Paul Reboa, Joshua W. Smith of HP for their assistance and advice in the work.

I would like to thank the Engineering Science and Mechanics Department at Virginia Tech for providing research facilities. Thanks are also due to Ms. Shelia Collins and Ms. Loretta Tickle in the ESM Dept. and Ms. Linda Haney and Ms. Tammy Hiner at the Center for Adhesive and Sealant Science at Virginia Tech for their help over the years.

I owe my sincere appreciation to my family and friends, who have supported and encouraged me over the years. I specially want to thank my wife, Hailan Wu for her inspiration, her love, care, and support.

TABLE OF CONTENTS

LIST OF FIGURES

LIST OF TABLES

CHAPTER 1

INTRDUCTION

1.1 Format of this dissertation

In this dissertation, Chapters Two to Five were written as independent publishable papers. Chapter One gives a general introduction and overview of the dissertation, and Chapter Six summarizes the work in this dissertation. Therefore, portions of the Introduction and Conclusions in each chapter are similar to some portions in Chapter One and Six.

1.2 Motivation

1.2.1 Polymers in the electronics industry

Polymers have been widely used in the electronics industry for many years. The tremendous growth in circuit density and performance of both the chip and package depend on a synergistic relationship between advanced circuit designs, and materials, tools, and processes used to bring these designs to fruition. As the ability to engineer the properties of polymers has grown, the polymer industry has been able to supply an ever-increasing variety of materials, which ranges from radiation-sensitive resists used to pattern the circuitry on chips and boards, to the polymers used both as insulators and on chip carriers themselves, and the encapsulants used for mechanical and corrosion protection of these chips. Of all the electronic applications of polymers, molding and encapsulation consume almost half the amount of all polymers [1]. The unique chemical, physical and mechanical properties of epoxy resin systems have made them the predominant thermosetting polymers for potting, bonding, and encapsulating a wide variety of electrical and electronic components [2, 3]. The most widely recognized

property of epoxy resins is their excellent adhesion to a very broad range of substrates [4]. Epoxy resins also provide excellent insulating and dielectric characteristics, and they often retain these properties under severe operating conditions [4]. Furthermore, relative to many polymeric materials, epoxy resin systems have characteristically low moisture absorption [4]. Although many works have been conducted to investigate and improve the adhesion and reliability of encapsulants, some reliability issues still exist. With the presence of moisture at elevated temperatures above ambient conditions, the initiation and slow propagation of debonding between encapsulants and substrates are important problems that may influence the durability of the devices. One task of this dissertation is to **investigate subcritical crack propagation along an epoxy-glass interface**.

1.2.2 Residual stresses in multilayer and thin film structures

When layers of dissimilar materials are bonded, differences in the coefficient of thermal expansion (CTE), combined with a temperature change relative to the stress-free state, result in thermal residual stresses. These stresses, along with edge and internal flaws, may result in the development of interfacial cracks. One task of this dissertation is to **analyze the effect of residual stresses in the adhesive of a double cantilever beam (DCB)/wedge specimen on the actual strain energy release rate**.

Thin film technology has become irreplaceable in the electronics industry. The mechanical properties, such as the modulus and adhesion to the substrate, have a significant impact on a device's performance and reliability. Residual stresses can be introduced into the system by external factors, e.g. temperature, moisture, curing, or service life. Residual stresses within a film can lead to delamination due to the significant interfacial stresses that can occur near free edges and other flaws, which can produce damage in service conditions. Furthermore, the requirement of high density and speed of circuitry has made ultra thin films (<10 nm) necessary [3] in modern electronic devices. However, the film processing, and environmental factors of such devices always result in significant intrinsic residual stresses, which may affect the performance of such delicate devices as micro electromechanical systems (MEMs). Therefore, mechanical characterization of residual stress is essential for understanding and predicting the performance of thin film coated devices. Of the diverse test geometries for measuring the

adhesion of thin films to rigid substrates, blister geometries are widely accepted, and many people have used different blister geometries to measure residual stresses. However, the solutions available in the literature have treated thin films either as bending plates without stretching deformation or flexible membranes without bending rigidity. Therefore, one of the goals of this dissertation is to **present a complete solution for the circular blister geometry in the presence of uniform tensile residual stresses**.

1.2.3 Gripping conditions on a Single-lap Joint (SLJ) specimen

In order to obtain basic material properties of new developed adhesives, such as the ones used in the microelectronics industry, some fundamental testing methods are still irreplaceable. The single-lap joint (SLJ) is a geometry designed to measure shear modulus and apparent shear strength, and has been adopted in several ASTM standards due to its simplicity of specimen preparation and testing. The general way to mount a SLJ specimen in a universal test frame is to use mechanical grips, thus the boundary conditions are different from what are often assumed in a mathematical model [5], which are simply-supported. However, most people ignore this difference by directly using solutions available in literature. Therefore, one of the goals of this dissertation is to **investigate the effect of boundary conditions for a single-lap joint geometry**.

1.3 Literature Review

The literature reviews on the respective topics are included in each of the subsequent chapters in order to avoid massive duplication. Readers can find the details for the following topics in the respective chapters:

1. Chapter Two: Stress corrosion cracking in inorganic and adhesively bonded systems.
2. Chapter Three: Thermal residual stresses in layered materials
3. Chapter Four: Blister analysis
4. Chapter Five: Single lap joints

1.4 Overview of this dissertation

The goal of this dissertation is to address four aspects in adhesion science:

1. Measure and model the subcritical crack growth along a glass/epoxy interface using a wedge test.
2. Study the effect of residual stress on the actual strain energy release rate of a double cantilever beam geometry.
3. Analyze the effect of residual stress on circular blister geometries.
4. Investigate the effect of boundary conditions of a single lap joint specimen.

In Chapter Two, measurements of the water-assisted subcritical crack propagation along a glass/epoxy interface are presented. The crack growth rate was measured as a function of applied strain energy release rate and temperature using a wedge test geometry. The specimens consist of two glass plates bonded with a thin layer of a proprietary epoxy adhesive, and the crack fronts along the epoxy/glass interfaces are measured using an optical stereomicroscope. The relationship between the applied strain energy release rate (denoted as G) and debonding rate can be measured, thus the threshold value of G for the debonding to arrest (denoted as G_{th}) can be determined from the measured data. Two types of testing procedures were conducted in this study: *ex situ*, i.e., pre-conditioned wedge tests and *in situ* ones, in which wedges were applied before the specimens were submerged in water. A model is developed based on the thermal activation barrier concept, and allows for the prediction of G_{th}.

In Chapter Three, the strain energy release rate solution for a DCB specimen in the presence of thermal residual stresses is reported. The solution was derived using simple beam theory, and residual stress was characterized by the curvature of a bi-

material strip. The strain energy release rate (SERR), G_T, caused by thermal loading is given in terms of the material properties and temperature difference from stress free state. G_T is found to be a constant independent of crack length. This solution was incorporated in the analysis of subcritical crack propagation in Chapter Two.

In Chapter Four, the analytical solutions for a clamped circular film in the presence of uniform isotropic in-plane tension were presented using the principle of virtual displacements. The plate is subjected to either uniform pressure or a central point load. The solutions are very simple, yet agree well with FEA results and other analytical solutions involving more complicated expressions. Furthermore, the strain energy release rate, G, was derived for a blister debonded from a rigid substrate in the presence of uniform tensile residual stresses. The relationships among G, load, deflection and debond radius are discussed. In addition, the discrepancy between analytical solutions and numerical results was investigated.

In Chapter Five the mechanics of a single-lap joint with different clamped-clamped boundary conditions subjected to tensile loading are investigated. A closed-form solution is obtained for a specimen configuration considering different clamping methods. The solution reported in this paper provides a simple, yet useful way to understand the behavior of this test geometry.

Chapter Six lists the conclusions based on this dissertation and provides suggestions for further research directions.

1.5 References

1 Colclaster, B. A. (1980) *Microelectronics Processing and Device Design*, John Wiley, New York.

2 Lau, J. (1996) *Flip-chip Technologies*, McGraw Hill, N.Y.

3 Bauer, R. S. (1993) Application of epoxy in electronics, *Polymers for Electronics and Photonics*, edited by Wong, C. P., Academic Press, Inc. 287-331.

4 Jong, C.-A., Chin, T.-S., and Fang, W. (2001) Residual stress and thermal expansion behavior of TaO_xN_y films by the micro-cantilever method, *Thin Solid Films*, **401**, 291-297.

5 Goland, M. and Reissner, E. (1944) The stress in cemented joints. *Journal of Applied Mechanics*, **55**, 109-115.

CHAPTER 2

WATER–ASSISTED SUBCRITICAL CRACK GROWTH ALONG AN EPOXY-GLASS INTERFACE

(To be submitted to the *Journal of Adhesion*)

2.1 Abstract

Water-assisted crack growth at an epoxy/glass interface was measured as a function of applied strain energy release rate, G, and temperature using a wedge test geometry. The specimens consist of two glass plates bonded with a thin layer of a proprietary epoxy adhesive. The crack fronts along the epoxy-glass interfaces were measured using an optical stereomicroscope. The relationship between G and the debonding rate, v, can be measured using this method, and the threshold value of G for a debonding to start growing, G_{th}, can be determined from the measured data. Two types of testing procedures were conducted in this study: *ex situ*, i.e., pre-conditioned wedge tests and *in situ* ones, in which wedges were applied before the specimens were submerged in water. A model was developed based on the thermal activation barrier concept, and allows the prediction of G_{th} for temperatures beyond the testing region.

Keywords: subcritical crack growth, temperature, diffusion, wedge test, epoxy-glass interface, adhesion, water, moisture-assisted crack growth.

2.2 Introduction

Epoxy resins contain unique chemical, physical and mechanical properties that have made them the predominant thermosetting polymers for potting, bonding, and encapsulating a wide variety of electrical and electronic components in the electronics industry [1]. The most widely recognized property of epoxy resins is their excellent adhesion to a very broad range of substrates. Epoxy resins also provide excellent insulating and dielectric characteristics, and they retain these properties under severe operating conditions [1]. Furthermore, relative to many polymeric materials, epoxy resin systems have characteristically low moisture absorption.

Semiconductor packaging industries use fracture energy as the parameter for avoiding crack growth in designing and predicting durability for microelectronic packages [2]. Fracture mechanics can be used to predict failures of assemblies due to subcritical crack growth, which can be a dominant mechanism particularly when products operate under humid environments. Environmentally-assisted subcritical crack growth (stress corrosion cracking) in homogeneous materials and adhesive bonds is reviewed in this section.

Stress corrosion cracking (SCC) is a term used to describe failure in engineering materials that occurs by slow, environmentally induced crack propagation [3]. The crack propagation is a result of the combined and synergistic interaction of mechanical stress and ingressive species. SCC is often used to describe failures in metallic materials. However, other classes of homogeneous materials and adhesively bonded joints also exhibit delayed failure by environmentally induced crack propagation, [4-19]. For clarification, although SCC is used to describe our system, corrosion does not happen at debond tip of our specimens.

A typical subcritical crack velocity v as a function of the stress energy release rate can be seen in Figure 2.1 [3]. There is often, but not always, a threshold value of strain energy release rate G, i.e. G_{th}, below which a crack does not move. There are three distinct regions when G is above G_{th}. In region I, v is very sensitive to G. In this region, v

is controlled by the stress-activated chemical reaction of the agent with the bond at crack tip [3]. In region II, v approaches a plateau velocity, v^*, and is fairly insensitive to G. In this region, the rate controlling process is believed to be the transportation of the agent to the crack tip [20]. In region III, crack velocity is again very sensitive to the value of G. This region is also is observed to be dependent on different gaseous or liquid environments [21, 22] in ceramic systems.

Water-assisted subcritical crack propagation in glass has been studied by many researchers for more than three decades. Wiederhorn [20, 24, 25] used the double cantilever cleavage technique to study the effect of water vapor on crack propagation in soda-lime glass, and developed combined equations, using the static fatigue theory of Charles and Hilig [26, 27], to account for the experimental data in region I and II. Weidmann and Holloway [28] measured the subcritical crack growth in glass using the double torsion tests and obtained similar results. Using both the double cantilever beam and double torsion specimens, Wiederhorn *et al.* [22] investigated the effect of water and dielectric properties on crack growth in soda-lime-silica glass. Based on their results, crack growth in region I is controlled primarily by the chemical potential of water in the organic liquid, whereas in region II, crack growth is controlled by concentration of water and viscosity of the solution of water and organic fluid. In region III, the slope of the crack-growth curves can be correlated with the dielectric constant of the liquid. Evans [29] presented an analysis which enables the facture strength, under constant stress-rate conditions, to be predicted from fracture mechanics data during slow crack growth. Simmons and Freiman [30] investigated the effect of corrosion processes on subcritical crack growth in glass, and claimed that changes in crack-tip shape takes place as a crack propagates from the plateau into region I. Wan *et al.* [31] studied the subcritical propagation of an internal lenticular delamination at a healed mica interface, and found that the debond growth is stable for both the pressurized and point load driven case.

As to modeling the subcritical crack propagation, Doremus [32] modified the Hillig-Charles theory using different failure time-stress relations. He claimed that the results are simpler than the original one, and confirmed the conclusion of Hillig and Charles. The Hillig-Charles theory was also developed into a more complicated model

based on multi-barrier kinetics [33-35], which provided a general equation that is able to take into account the three regions. Several researchers [36-38] analyzed subcritical crack propagation as a thermally activated process, and provided various equations to predict experimental results. Michealske and Bunker [39] proposed a model to predict the subcritical crack growth in glass. The model is able to consider the stress enhanced hydrolysis reaction at crack tip. Maugis [40] presented a thorough review of subcritical crack growth, surface energy, facture toughness in a generalized fashion that can be applied to facture of glasses, ceramics, and brittle polymers. Mishin, *et al.* [41] extended a thermodynamic analysis of interfacial decohesion in the presence of mobile impurities to consider the arbitrary relation between the rate of decohesion and impurity of supply to the interface. They also proposed a dynamic model which can describe the whole region of decohesion rate.

The work on subcritical crack propagation along an interface is relatively limited compared with the massive work on monolithic materials. Mostovoy and Ripling [7] are among the earliest researchers to investigate SCC in adhesively bonded joints. They conducted the debonding measurement along an epoxy-aluminum interface using a contoured double cantilever beam (DCB) geometry. They observed mixed (cohesive + interfacial) failure mode and found that water lowers the load carrying capability at the interface, but toughens the cohesive debond tip. Their work is primarily experimental, so they didn't propose any model to predict SCC behavior on such interface. Adopting the Boeing wedge test, Cognard [8, 9] conducted a series of subcritical debonding measurements of an adhesive-stainless steel system. He found different behavior for different combinations of adhesive and liquid, yet only gave the data in Region II. Crosley and Ripling [10] proposed a thick DCB geometry for SCC measurement for adhesively bonded metal joints. Ritter [11-14] explored the SCC behavior of polymer-glass interface using various testing geometries, e.g. DCB specimen, four-point flexural sandwich specimen, and double cleavage drilled compression (DCDC) specimen. He proposed an empirical expression, $v = A G^n$, to mimic the experimental G-v data in Region I. A and n are constants that depend on the material system and environment. He found that silane-treated glass specimens are more resistant to crack growth than untreated ones. He also claimed that phase angles that differ from 15° to 54° have a negligible effect on

moisture-assisted crack growth. A phase angle is defined as $\tan^{-1}(K_{II}/K_I)$, or $\tan^{-1}\sqrt{G_{II}/G_I}$, where K and G are stress intensity factor and strain energy release rate respectively and subscripts I and II represent mode I (open) and mode II (shear), respectively. Arnott [15] used a constant load-point displacement rate method to test double cantilever beam specimens of aluminum alloy bonded with adhesive, and found that in humid air at elevated temperature, G depends strongly on load-point displacement rate. At high rates, G is equivalent to G_c, and at very low rates, the bond was degraded and G is equivalent to G_{th}. In a region between the two extremes, G is sensitive to load-point displacement rate because moisture degraded the bond at a rate similar to the crack velocity. Fernando, *et al.* [16] used a fracture mechanics approach to examine the effect of surface pretreatment on the fatigue behavior of adhesively bonded aluminum-alloy joints. They found that surface pretreatments such as phosphoric-acid anodization (PAA), and PAA followed by the application of primer, increased G_{th} significantly. Tai *et al.* [17] studied the delamination of automotive filled epoxy adhesives from different steel substrates upon exposure to distilled water and NaCl solutions using a three-point bend device, and found that the degree of delamination (length of debond) is affected by the concentration of NaCl, level of applied stress, and filler content in the adhesive. Frantizs [18] reported a new test device for measuring subcritical crack propagation along an adhesive-adherend interface. The test configuration consisted of a double torsion (DT) specimen and a graphite gauge for the measurement of crack length. Adhesive plasticization and crack-tip blunting were thought to contribute to the increase of durability in the brittle unmodified adhesive. Gurumurphy [19] investigated the stress corrosion behavior along a polymer/polymer interface using an asymmetric DCB (ADCB) specimen, and proposed a theory based on thermal activation energy to predict the experimental results.

In this chapter, the measurements of subcritical crack growth velocity for an interface between a filled proprietary epoxy and borosilicate glass is presented. Two testing procedures: *in situ* tests and *ex situ* (preconditioned) tests were conducted. Since the energy release rate provided to the crack tip in our tests is far below the critical value, region III was not included in our measurements. Thermal residual stress was considered

in this study, and a model has been proposed to describe the preconditioned subcritical crack propagation behavior and it fits the experimental results fairly well. Although the model has been developed for an epoxy/glass interface, it can, in general, be applied to a subcritical crack growth along other interfaces if the same failure mechanism is involved.

2.3 Experimental

2.3.1 Materials

Silicon is the ideal material for the adherends in this study because it is the most widely used inorganic material in the microelectronics industry. However, it was not chosen due to the high cost and difficulty in specimen preparation (high quality cutting (or sawing) facility is required). Furthermore, a crack front can not be directly observed through opaque silicon substrates. The author has attempted to measure the crack growth speed of the silicon specimens using a scanning acoustic microscopy (SAM) method, but the results were not reliable. Because the adhesion between the epoxy and silicon was so weak in such specimens, some uncontrolled factors, one of which is that specimens must be submerged in water before each scanning, can affect the measurement significantly. Actually, the latter SAM measurements with strongly bonded specimen illustrated better results. Therefore, borosilicate glass was chosen as an alternative adherend material for the wedge tests due to cost effectiveness, easy specimen preparation, and transparent nature, which makes the crack front easy to observe.

A proprietary filled epoxy resin was used as the adhesive because of its availability and opaque nature. The adhesive was provided by the Hewlett-Packard Company, and contains several metal oxide additives in order to control the viscosity, thermal, mechanical, and chemical properties in processing and service.

2.3.2 Specimen preparation

Figure 2.2 illustrates the specimen preparation procedure for the wedge specimens used in this study. A fixture was designed to improve the alignment for substrates and adhesive layer during specimen fabrication, which made specimen preparation easy and

consistent. Glass plates with a thickness of 0.7 mm were first cut into 10 mm × 100 mm strips as substrates using a diamond saw. After being cleaned with an acetone wipe, two glass strips were bonded together using the epoxy resin. A 0.25 mm thick, window-shaped PTFE gasket was used to control bond thickness and width and also to prevent the adhesive from flowing out of the bonded region. The clamped glass/adhesive sandwich specimens were then cured in a convection oven at 150°C for 30 minutes, as suggested by the manufacturer. The PTFE gasket in each specimen was pulled out after the specimen cooled down to room temperature. The removal of the gaskets was generally easy, and the specimens with gasket residue were disposed of so as to avoid any unexpected effect on the subsequent experiments. For the specimens in the *in situ* tests, an initial debond was introduced into each specimen by carefully tapping a wedge between the two adherends. As for the pre-conditioned specimens, wedges were tapped into the specimens after the desired pre-conditioning time.

2.3.3 Specimen conditioning and crack length measurement

Although various organic solutions can be present in the environment for some electronic devices, water is believed to be a common means for environmentally assisted crack growth. Therefore, deionized water was used as the conditioning liquid in our study.

Two different test methods were adopted in this study: conventional *in situ* wedge tests and preconditioned *ex situ* ones. The conventional *in situ* wedge tests were conducted initially, but the cracks stopped unexpectedly quickly (the interval between the last two crack length measurements was as long as five days with no observed debond propagation). Crack blunting was also observed in this testing method using an optical profiler as will be discussed later. Figure 2.3 shows the log v versus G data for the *in situ* wedge test at RT (room temperature), 40°C, and 60°C, respectively. At these three different temperatures, similar velocities at the plateau region of log v versus G data were observed. Figure 2.4 shows the velocity in the plateau region, v^*, as a function of testing temperature. Because v^* is related to the moisture diffusion along an interface, it should be a function of temperature [11, 16, 19], which is not illustrated in our experiments. The

interpretation of the *in situ* experiments will be discussed in detail later in this Chapter. To obtain meaningful crack propagation data, a modified pre-conditioned testing method was adopted in this study, and the procedure is as follows:

1. The as-prepared sandwich specimens were pre-conditioned in water at the desired temperatures (RT, 40°C, and 60°C, respectively) prior to inserting the wedges.
2. After different pre-conditioning periods, specimens were taken out of water, and wedges were inserted into the specimens.
3. The crack length was monitored over time at ambient, lab conditions using an optical stereomicroscope with a magnification range from 9X to 40X (The period between the last two crack length measurements was as long as five days).

The specimens were placed in a 100% relative humidity condition (in test tubes) at room temperature after each debonding length measurement to reduce moisture evaporation from the specimens during the observation period.

2.4 Results of the ex situ (pre-conditioned) tests

2.4.1 Log G vs. Log v

Figure 2.5 to Figure 2.7 show the G vs. v data on log-log scales, where G is the applied strain energy release rate and v the debond propagation rate, for the three pre-conditioning temperatures. Three to five specimens were tested at each condition. The debonding rate is calculated by dividing the distance between two subsequent crack tip observations by the elapsed time. Because the objective of this study is to investigate G_{th}, only the data close to this threshold state was collected. Based on the observation of these data, when the debonding rate v is below 10^{-7}~10^{-8} m/s, the debond propagation

reaches an arrest state, thus G_{th} is measured at such speeds. The dotted lines in these figures illustrate the threshold values taken. One noted observation in the *ex situ* wedge tests is that if a specimen was preconditioned sufficiently long, the initiated debond (with a wedge) kept growing at a velocity of 10^{-4} -10^{-5} m/s until the adherends completely separated (the whole process lasted less than one hour), even when no wedge was present during this process. The discussion in the following sections and Chapter Three suggests that the driving force for debond growth in this phenomenon is due to the thermal stresses in the specimens. This makes the actual G_{th} measurement after critical preconditioning time impossible because the SERR produced by thermal residual stresses is larger than actual G_{th}. Furthermore, such limiting preconditioning times were observed to be a function of temperature. By measuring the curvature of the bi-material part of the separated wedge specimens beyond limiting preconditioning times, the strain energy release rate, G_T, caused by thermal residual stress in the adhesive can be calculated. G_T was found to be in the region of the measured G_{th} for the specimens that were pre-conditioned close to the limiting preconditioning time (~ 0.1-0.5 J/m^2). If we shift the data points in Figure 2.5-2.7 by the corresponding thermally induced SERR, G_T, the actual G_{th} can be obtained. Because G_T is only significant compared with G_m (produced by a wedge) in the long term preconditioned specimens, only the results for such conditions were affected. For clarification, G_{th} discussed the following subsection is in fact the wedge induced part of the actual G_{th}.

2.4.2 Log G_{th} vs. Log t

From the G vs. v data, the relationship between wedge produced G_{th} and the corresponding pre-conditioning time t can be obtained, as shown in Figure 2.8. The error bars represent one standard deviation of the data for each condition. Increasing temperature decreases G_{th} significantly if the specimens were pre-conditioned for the same time, and as expected, the results of 40°C tests are between the results for RT and 60°C. The concave shape of the data trend implies that there exits a critical pre-conditioning time for each temperature beyond which an apparent G_{th} may not exist. G_{th} in this figure is caused by the wedges, and thermally induced SERR, G_T, is not included.

However, an accurate G_{th} is not easy to measure because G_T cannot be determined directly for the preconditioned specimens due to the change of residual stress and material properties, and water ingression in the specimens. Consideration of G_T is included in the following modeling.

2.5 Modeling for the pre-conditioned wedge tests

In order to capture the observed phenomena in the *ex situ* (pre-conditioned) wedge tests, a preliminary model is proposed based on the concept of a thermal activation barrier. This section describes the details of this model and a comparison between the experimental results and the predictions by the model is discussed.

2.5.1 Assumptions

The following three assumptions are used for building the model:

1 The decrease of G_{th} with preconditioning time is mainly due to the water's ingression into the adhesive layer between the adherends along the width direction. G_{th} is a function of relative moisture concentration in the adhesive joint. When the moisture concentration in the specimen is saturated, G_{th} approaches a constant value.

2 The diffusion kinetics of the moisture into the adhesive bonds follows Fick's Second Law.

3 The diffusion coefficient as a function of temperature follows an Arrehinus equation.

The first assumption is based on the fact that the adhesive's length is much larger than the width (length/width=20). Zanni-Deffarges *et al.* [42] used a similar approach to study an interfacial diffusion problem. Gledhill, *et al.* [43] predicted the fracture stress of the butt joint specimens exposed in aqueous environments using water diffusion data. The assumption of constant G_{th} after saturation is justified by the fact that G_T is the dominant contributor of total G_{th}, and it becomes almost unchanged after long term of

preconditioning. Figure 2.9 illustrates a schematic of the specimen configuration for the modeling. It is normally assumed that the diffusion of water into the bulk adhesive follow Fick's Second Law. Comyn [43] employed tritiated water to measure the water concentration in the adhesive bonded joint, and found good agreement with calculations based on Fickian diffusion. Therefore, the second assumption should be reasonable. The last assumption is based on the moisture diffusion results for bulk polymeric materials [44], which is adopted for this system.

2.5.2 Mathematical formulation

Based on the above assumptions, G_{th} can be expressed as follows

$$G_{th} = G_0\left[1-(1-h)\frac{\int_{-w/2}^{w/2} C(x,t)dx}{C_0 w}\right] \tag{1}$$

where G_0 is the threshold strain energy release rate prior to preconditioning, $C(x,t)$ is the moisture concentration at the adhesive joint, C_0 is the saturation concentration, and w is the bond width. Parameter controls the value of G_{th} after a long term preconditioning, and is chosen as 0.01 in the model in that G_0 ~ 17 J/m^2, and G_T~.0.1-0.2 J/m^2 after long term preconditioning.

Fickian diffusion kinetics can be expressed as:

$$\frac{\partial^2 C}{\partial x^2} = \frac{1}{D}\frac{\partial C}{\partial t} \tag{2}$$

where C is the moisture concentration at the bond, D is the diffusion coefficient, x is the coordinate, and t the time. Let the specimen occupy region $-w/2<x<w/2$, so that there is symmetry about $x=0$, and the boundary conditions may be expressed as

$$C = C_0,\ x = \pm\frac{w}{2},\ t \geq 0$$

$$\frac{\partial C}{\partial x} = 0,\ x = 0,\ t \geq 0$$

The diffusion coefficient D is expressed as:

$$D = D_0 Exp\left(\frac{-E_a}{RT}\right) \tag{3}$$

where D_0 is a constant, E_a is activation energy, R is ideal gas constant, and T is Kelvin temperature.

Adoptinging the solution of diffusion in a plane sheet [45], the solution of our problem can be expressed as follows:

$$C/C_0 = 1 - \frac{4}{p}\sum_{n=0}^{\infty}\frac{(-1)^n}{2n+1}e^{-(2n+1)^2 p^2 \frac{Dt}{w^2}}\cos\frac{(2n+1)p\,x}{w} \tag{5}$$

This solution can take into account several primary variables in the system: specimen width w, activation energy E_a, preconditioning time t, and diffusion coefficient D along the interface. Figure 2.10 shows this solution, and significant discrepancy is found between the model and experimental results shown in Figure 2.8. Limiting preconditioning times after which G_{th} becomes zero is not indicated in the model while they are observed in the experiments. However, residual stress is not considered in this model, but the experimental observations show that it plays an important role in the measurement, especially in long term measurement.

2.5.3 Consideration of residual stresses

The CTE mismatch between the adhesive and adherends causes tensile thermal residual stresses in the adhesive of the wedge specimens in our tests. The residual stress in a bimaterial strip causes the specimen to bend, thus the curvature of the bent bimaterial strip can be measured to characterize the residual stress. The curvature of a bimaterial

strip separated from an as-prepared wedge specimen was measured using the optical profiler and Figure 2.11 shows the interface screen of the measurement. Due to the existence of residual stress, an extra applied strain energy release rate, G_T, induced by the thermal stress, was present along with the wedge driven SERR, G_m, during the propagation of debonding. The debonding phenomenon was actually observed along the other glass/adhesive interface during the *in situ* tests as shown in Figure 2.12. The discussion in Chapter Three suggests that G_T is a function of the temperature difference from the stress free temperature and material properties of both the adhesive and adherends, but G_T is independent of debond length. Figure 2.13 shows G_T and G_m for the specimens in our experiments. When crack length is longer than 20 mm, G_T/G_m >10%, so G_T should be considered. On the other hand, with the presence of water at elevated temperatures, the thermal residual stress in the adhesive layer relaxes with time during preconditioning due to the viscoelastic nature and change in the adhesive's material properties. The traces of radius of curvature for the bimaterial strips submerged in water at three different temperatures are illustrated in Figure 2.14. Subsequently, G_T gets smaller with preconditioning as well. As shown in Chapter Three, $G_T \sim 1/r^2$, so we can obtain G_T as a function of preconditioning time by measuring the curvature of the bi-material part of the wedge specimens after they are preconditioned after different desired times. Figure 2.15 shows the results at 60°C, and the following empirical equation may be employed to calculate the change of G_T with preconditioning time based on this figure:

$$G_T(0) - G_T(t) = k(T)t^{1/2} \tag{6}$$

where $G_T(0)$ and $G_T(t)$ are the residual stress induced SERR prior to preconditioning and after the desired preconditioning time of t, respectively, and $k(T)$ is an empirical function of temperature. Because material properties of the adhesive change during preconditioning due to water ingression and the degradation in material, $k(T)$ can not be found directly using material properties, thus needs to be determined using experimental data. On the other hand, (6) is only true for relatively short time of preconditioning.

After a long period of preconditioning, (6) may not be accurate because stress relaxation is close to completion and moisture concentration in the specimen is close to saturation. Therefore, $G_T(t)$ becomes independent of time and temperature. Adapting the diffusion solution in (5), $G_T(t)$ can be expressed in a more general equation for the whole preconditioning period as follows:

$$G_T(0,T) - G_T(t,T) = [G_T(0,T) - G_{T\infty})]\left[1 - \frac{8}{p^2}\sum_{n=0}^{\infty}\frac{1}{(2n+1)^2}Exp\left(-\frac{(2n+1)^2 p^2}{4}K(T)t\right)\right] \quad (7)$$

where $G_T(t,T)$ is the thermal strain energy release rate, which is a function of time and preconditioning temperature, T. $K(T)$ represents the drop of $G_T(t,T)$ with time, can be expressed in a form similar as in (3): $K(T) = K_0 Exp(-E_a / RT)$. G_{T8} is the thermal energy release rate after the completion of stress relaxation. By Subtracting $G_T(t,T)$ from G_{th} in (1) to fit the experimental results in which residual stresses were not considered, the following parameters can be obtained: G_0, D_0, G_{T8} , K_0.

2.5.4 Modeling results

By applying a non-linear fitting technique using the data for one temperature, say, RT, the parameters in the model can be obtained. A typical value of activation energy for secondary bonding (Wan der Waals bonding), i.e. 10 *KJ*/mol was chosen in the fitting procedure. Figure 2.16 shows the results, and the data points are the additives of the experimental results and predicted G_T. Table 2.1 lists the parameters obtained from the fitting procedure. Interestingly, diffusion coefficient D calculated using this model is much larger than bulk diffusion results, and it suggests that interfacial diffusion may be the controlling mechanism for the degradation of G_{th} with preconditioning, because moisture tends to transport faster along a polymer-glass interface than in a bulk polymer [42]. Although the model ignores some issues in this problem, e.g. non-Fickian diffusion behavior, it still shows encouraging agreement with our experimental data. Also one of the most interesting features of this model is its capability of taking account residual

stress in the preconditioning process, thus the model provides a potential application to the system in which residual stress plays an important role.

2.6 Discussions on the in situ testing results

The results for the *in situ* wedge tests reported in Figure 2.3 do not exhibit the typical subcritical crack growth behavior, in which the debonding rate in region II is a function of temperature. However, the crack growth velocity at the plateau region of log G vs. log v data lies in the same range for the three tested temperatures. Here a qualitative explanation of this phenomenon is provided. During the *in situ* testing, the debonded part of adhesive is exposed to water, thus the diffusion of water along both the polymer/glass interface and into bulk polymer tends to change the residual stress in the specimen, causing G_T to decrease during the test. Therefore the actual driving force for debond growth decreases with time throughout the testing, which makes accurate G measurements difficult. Furthermore, the continuous exposure of fresh adhesive to water during debonding causes the residual stress distribution along the specimen to change with time as well. On the other hand, blunting of the debond tip was observed in the post-tested specimens using an optical profiler. Figure 2.17 shows the profile of the debond front from a in situ specimen tested at 60°C. The curved step is where the crack ceased during testing. For comparison, the profile of the debond front from an preconditioned tested specimen (at 60°C) was shown in Figure 2.18. The figure just illustrates part of the specimen because the profiler is capable to scan only a small area (5mm x 5mm) at each time. No blunting was observed in the whole region of preconditioned specimens. In order to clarify whether the step's height changes with time and water content in the adhesive, we measured the height using an optical profiler in a dry environment at 70°C (in a convection oven) for 10 days, and it didn't change with time (~11 μm), as shown in Figure 2.19. Therefore, the blunting deformation is primarily plastic, and is caused by softening of epoxy and the singular stress state around the crack front. This preliminary test also indicates that viscoelastic deformation and the swelling of the adhesive in the vicinity of crack front caused by water ingression is negligible compared with plastic deformation. These two factors make the *in situ* results

from our experiments look unreasonable. Indeed, the influence of the thermally induced SERR, G_T, is very significant in this study because the wedge induced SERR, G_m, is on the same order of G_T caused by thermally residual stress in the latter stage of the tests. However, if the adhesion between the adhesive and adherends is so strong that the external driving force is much larger than what the residual stresses produce, typical log G vs. log v results should be observed.

2.7 Conclusions

We have used a wedge test technique for measuring the water-assisted subcritical crack growth rate along a proprietary epoxy/polymer interface. Two testing methods were conducted: *in situ* tests and *ex situ* (preconditioned) ones. The *in situ* testing results did not illustrate typical stress corrosion cracking behavior. A subsequent investigation of residual stress and observation of crack blunting in *in situ* tests qualitatively reveals that the evolution of residual stress during testing and blunting of debond front due to plastic deformation in the vicinity of debond front causes crack growth to cease unexpectedly. Thus G_{th} and the observed debonding rate didn't demonstrate the expected temperature dependence. A modified *ex situ*, or pre-conditioned wedge test was conducted to investigate the effect of moisture concentration along the epoxy/glass interface on G_{th}. The experimental testing results, from the three temperatures (25°C, 40°C, and 60°C) tested, all show that G_{th} decreases with preconditioning time and that temperature accelerates this degradation process. Based on the thermal activation barrier concept, a model was developed to capture the mechanism. This model takes account of the primary variables in this system: geometry, diffusion coefficient, activation energy, pre-conditioning time, and residual stress.

2.8 References

1 Bauer, R. S. (1993) Application of epoxy in electronics, *Polymers for Electronics and Photonics*, edited by Wong, C. P., Academic Press, Inc. 287-331.

2 Jacobs, L. (1997). Technology gaps and research needs in electronic packaging-An industry perspective. *Presentation at Cornell Industry Alliance for Electronic Packaging*. Cornell University, New York.

3 Jones, R. H. and Ricker, R. E.(1992) *Mechanisms of stress-cross cracking, Stress-Corrosion Cracking*, Edited by Russell H. Jones, ASM International, Ohio, USA.

4 Fellers, J. F. and Kee, B. F. (1974) Crazing studies of polystyrene I. A new phenomenological observation. *Journal of Applied Polymers Science*, **18**, 2355-2365.

5 Kramer, E. J.(1979) Environmental cracking of polymers, *Developments in Polymer Fracture*, Vo. 1, Ed. by E. H. Andrews, 55-120.

6 Sumison, H. T. and Williams D. P. (1975) Environmentally induced cracking behavior of polymers, *Fatigue of Composite Materials*, **STP 569**, 226.

7 Mostovoy, S. and Ripling, E. J. (1969) Influence of water on stress corrosion cracking of epoxy bonds. *Journal of Applied Polymer Science*, **13**, 1083-1111.

8 Cognard, J. (1988) Use of the wedge test to estimate the lifetime of an adhesive joint in an aggressive environment, *International of Adhesion and Adhesives*, **6**, 215-219.

9 Cognard, J. (1988) Environmental attack on adhesive joints studied by cleavage fracture, *Journal of Adhesion*, **26**, 155-169.

10 Crosley, P. B. and Ripling, E. J. (1991) A thick adherend, instrumented double-cantilever-beam specimen for measuring debonding of adhesive joints, *Journal of Testing and Evaluation*, **9**, 24-28.

11 Ritter, J. E. and Conley, K. (1992) Moisture-assisted crack propagation at polymer/glass interfaces, *International Journal of Adhesion and Adhesives*, **13**, 245-250.

12 Conley, K. M., Ritter, J. E., and Larden, T. J. (1992) Subcritical crack growth along epoxy/glass interfaces, *Journal of Materials Science*, **6**, 2621-2629.

13 Ritter, J. E, Lardner, T. J., Stewart, A. J. and Parakash, G. C. (1995) Crack propagation in polymer adhesive/glass sandwich specimens, *Journal of Adhesion*, **49**, 97-112.

14 Ritter, J. E., Fox, J. R., Hutko, D. I. and Lardner, T. J. (1998) Moisture-assisted crack growth at epoxy-glass interface. *Journal of Materials Science*, **33**, 4581-4585.

15 Arnott, D. R. and Kindermann, M. R. (1995) Constant displacement rate method for testing epoxy adhesive bonds, *Journal of Adhesion*, **48**, 85-100.

16 Fernando, M., Harjoprayitno, W. W., and Kinloch, A. J. (1996) A fracture mechanics study of the influence of moisture on the fatigue behavior of adhesively bonded aluminum-alloy joints, *International Journal of Adhesion and Adhesives*, **16**, 113-119.

17 Tai, R. C. and Szklarska-Smialowska, Z. (1996) Delamination of filler-incorporated automotive epoxy adhesives from different steel substrates upon exposure to distilled water and NaCl solutions under applied bending stress, *Journal of Materials Science*, **31**, 1925-1935.

18 Frantizs, P. (1998) Environmental attack on adhesive joints (Part I: test equipment), *JSME International Journal*, **A41**, 231-242.

19 Gurumurphy, C. K., Kramer, E. J. and Hui, Chung-Yuen (2001) Water-assisted subcritical crack growth along an interface before polyimide passivation and epoxy underfill. *International Journal of Fracture*, **109**, 1-28.

20 Wiederhorn, S. M. (1967) Influence of water vapor on crack propagation in soda-lime glass. *Journal of American Ceramic Society,* **50**, 407-414.

21 Freiman, S.W. (1974) Effect of alcohol on crack propagation in glass, *Journal of American Ceramic Society,* **57**, 350-353.

22 Wiederhorn, S. M. Freiman, S. W., Fuller, E. R. and Simmons, C. J. (1982) Effect of water and other dielectrics on crack growth. *Journal of Materials Science,* **17**, 3460-3478.

23 Freiman, S.W. (1974) Effect of Alcohol on Crack Propagation in Glass, *Journal of American Ceramic Society,* **57**, 350-353.

24 Wiederhorn, S. M. and Boltz, L. H. (1970) Stress corrosion and static fatigue of glass. *Journal of American Ceramic Society,* **53**, 543-548.

25 Wiederhorn, S. M. (1975) Crack growth as an interpretation of static fatigue of glass. *Journal of Non-crystalline Solids*, **19**, 169-181.

26 Hillig, W. B. and Charles R. J. (1962) Surface, stress-dependent surface reaction, and strength, *High-strength Materials*, Edited by Zackey, V. E., John Wiley and Sons Inc., New York, 682-705.

27 Charles R. J. and Hillig, W. B. (1961) The kinetics of glass failure by stress corrosion. *Symposium on the mechanical strength of glass and ways of improving it*. Union Scientifique Continentable du Verre, France, 511-527.

28 Weidmann, G. W. and Holloway, D. G. (1974) Slow crack propagation in glass, *Physics and Chemistry of Glasses*, **15**, 116-122.

29 Evans A. G. (1972) A method for evaluating time dependent failure characteristics of brittle materials and its application to polycrystalline alumina. *Journal of Materials Science,* **7**, 1137-1146.

30 Simmons, C. J. and Freiman, S. W. (1981) Effect of corrosion processes on subcritical crack growth in glass, *Journal of the American Ceramic Society*, **62**, 683-686.

31 Wan, K.-T., Horn, R.G., Courmont S., Lawn, B. R. (1993) Pressurized internal lenticular cracks at healed mica interfaces. *Journal of Materials Research*, **8**, 1128-1136.

32 Doremus. R. H. (1980) Modification of Hilling-Charles theory for static fatigue of glass, *Engineering Fracture Mechanics*, **13**, 945-953.

33 Krautz, A. S. (1979) The theory of thermally activated process in brittle stress corrosion cracking, *Engineering Fracture Mechanics*, **11**, 33-42.

34 Krausz, A. S. (1978) The deformation and fracture kinetics of stress corrosion cracking, *International Journal of Fracture*, **14**, 5-15.

35 Brown, S. D. (1978) Multibarrier kinetics of brittle fracture: I, stress dependence of the subcritical crack velocity, *Journal of American Ceramic Society,* **62**, 515-523.

36 Pollet, J.-C. and Burns S. J. (1977) Thermally activated crack propagation-theory, *International Journal of Fracture*, **13**, 667-679.

37 Shoeck, G. (1990) Thermally activated crack-propagation in brittle materials, *International Journal of Fracture*, **44,** 1-14.

38 Wan, K-T, Lathabai, S. and Lawn, B. R. (1990) Crack velocity functions and thresholds in brittle solids, *Journal of European Ceramic Society,* **6**, 259-268.

39 Michalske, T. A. and Bunke, B. C. (1993) A chemical kinetics of model for glass fracture, *Journal of American Ceramic Society,* **76**, 2613-2618.

40 Maugis, D. (1985) Subcritical crack growth, surface energy, fracture toughness, stick-slip and embrittlement, *Journal of Materials Science*, **20**, 3041-3073.

41 Mishin, Y., Soforonis, P., and Bassani, J. L. (2002) Thermodynamic and kinetic aspects of interfacial decohesion, *Acta Materialia*, **50**, 3609-3622.

42 Zanni-Deffarges, M. P. and Shanahan, M. E. R. (1995) Diffusion of water into an epoxy adhesive: comparison between bulk behavior and adhesive joints, *International Journal of Adhesion and Adhesives*, **15**, 137-142.

43 Gledhill, R. A., Kinloch, A. J., and Shaw, S. J. (1980) A model for predicting joint durability, *Journal of Adhesion*, **11**, 3-15.

44 Comyn, J. (1987) Kinetics and mechanism of environmental attack, *Durability of Structural Adhesives* (Edited by Kinloch, A. J.), Applied Science Publishers, London.

45 Crank, J. (1957) *The Mathematics of Diffusion*, Oxford University Press, London, UK.

2.9 Tables

Table 2.1 Values of G_{th} parameters in the model

G_0 (J/m^2)	$G_{T\infty}$ (J/m^2)	K_0	D_0 (m^2/sec) x 10^{-7}
17	0.2	3.1	0.7

2.10 Figures

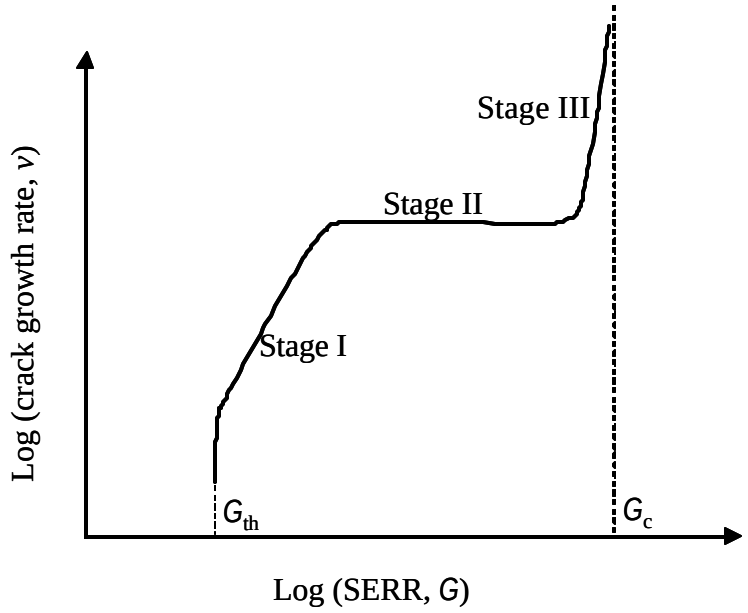

Figure 2.1 Schematic of a typical stress corrosion cracking (SCC) result. G_c represents the fracture energy and G_{th} is the arrest stress corrosion strain energy release rate below which stress corrosion cracking does not occur.

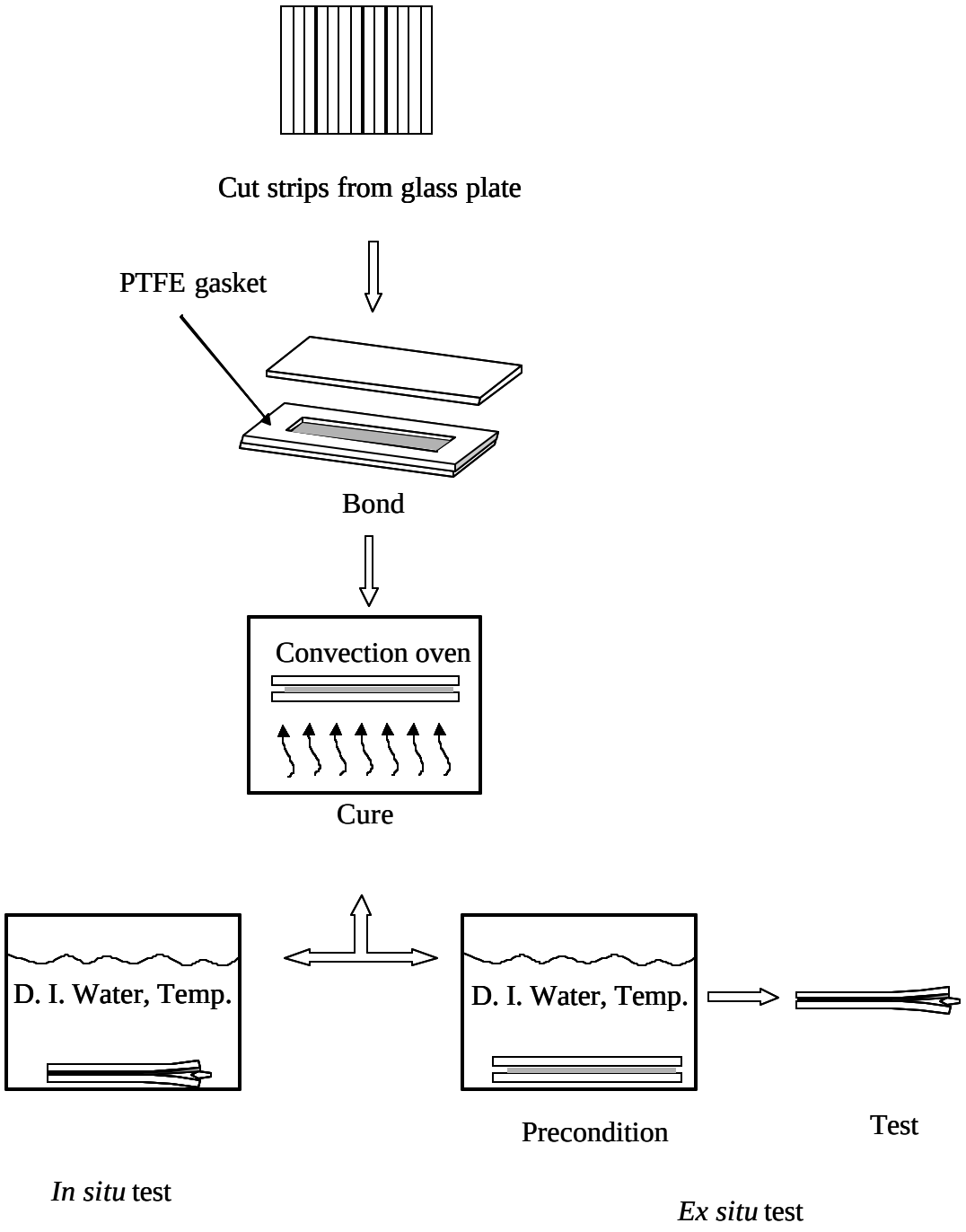

Figure 2.2 Schematic of the specimen preparation procedure for wedge tests. A PTFE gasket was used for controlling bond thickness and width.

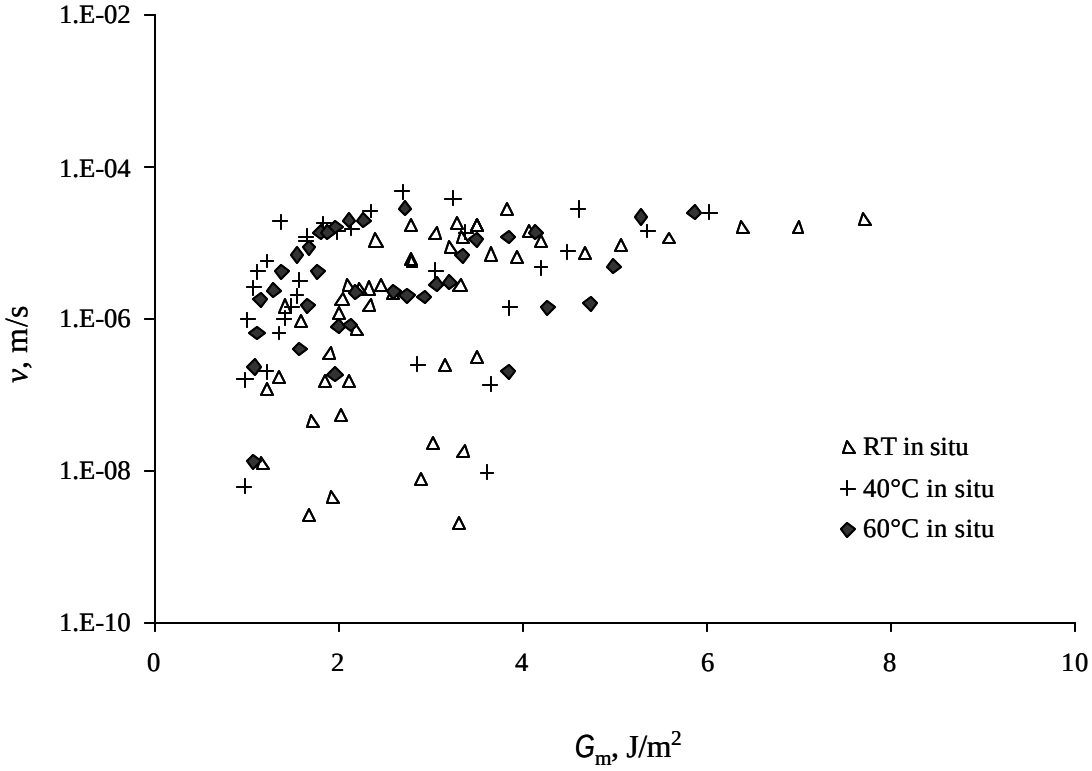
1.E-02
1.E-04
1.E-06
1.E-08
1.E-10
v, m/s
0
2
4
6
8
10
G_m, J/m^2
RT in situ
40°C in situ
60°C in situ

(a)

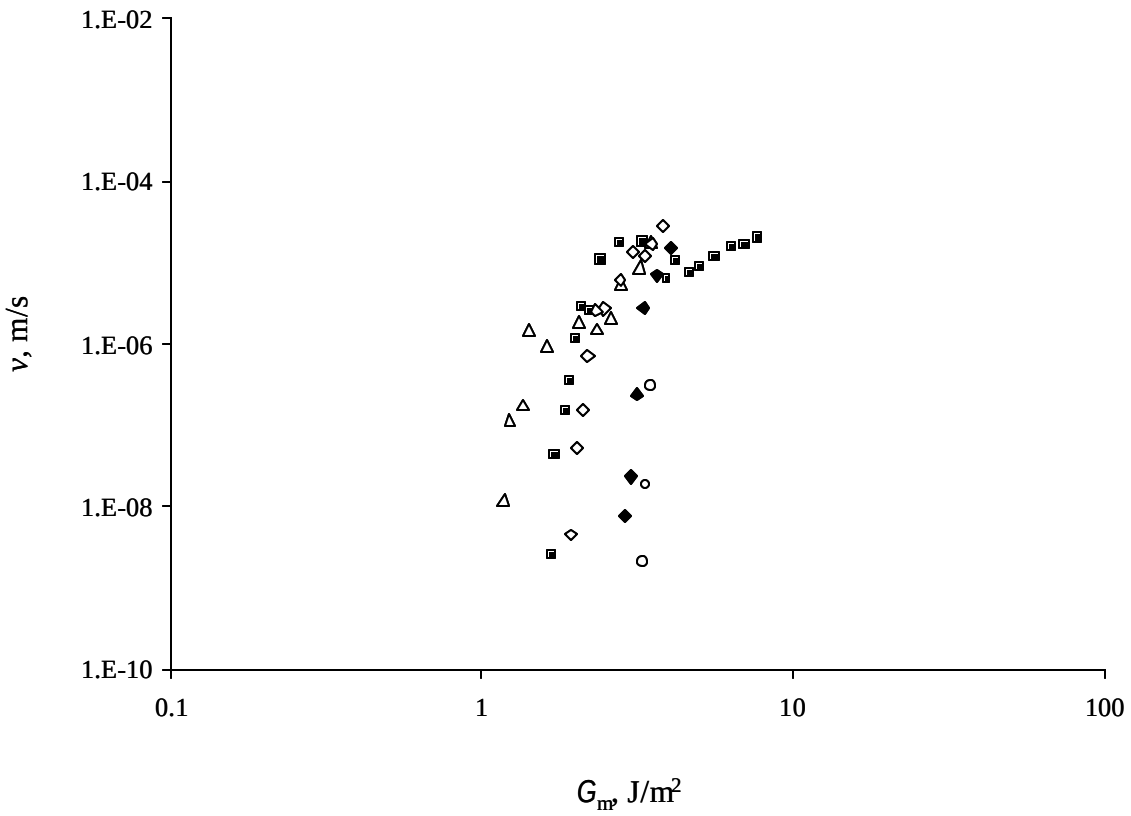

(b)

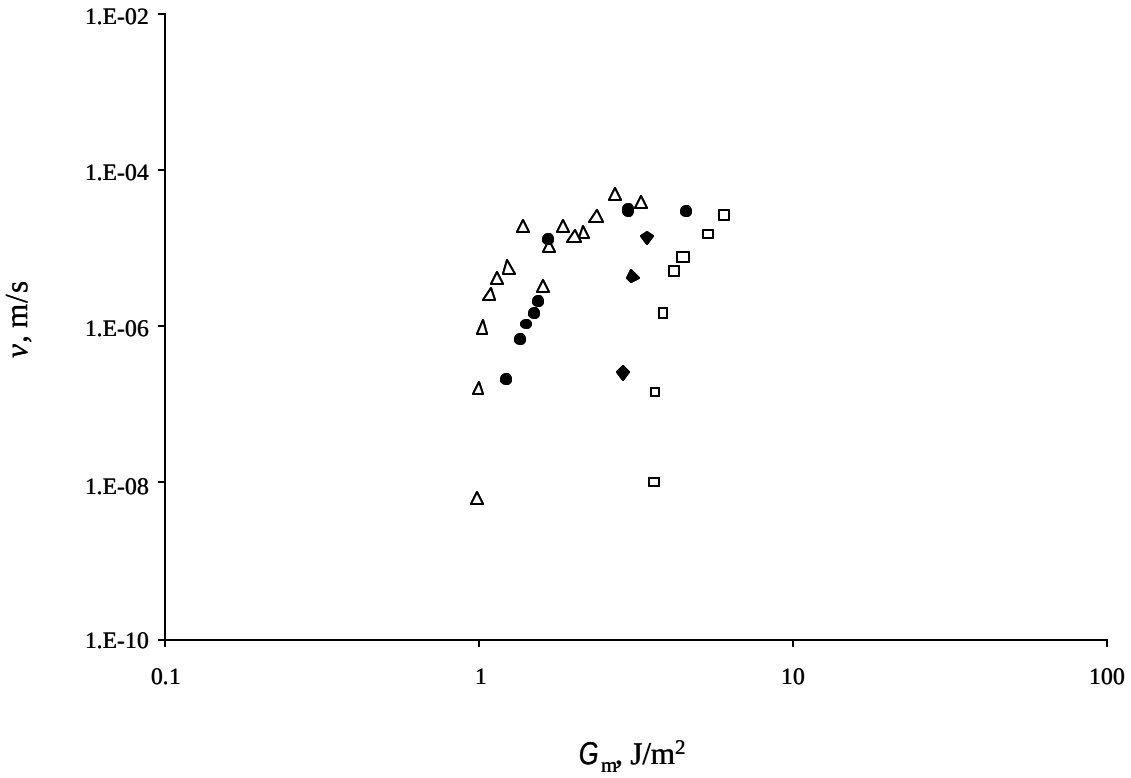

(c)

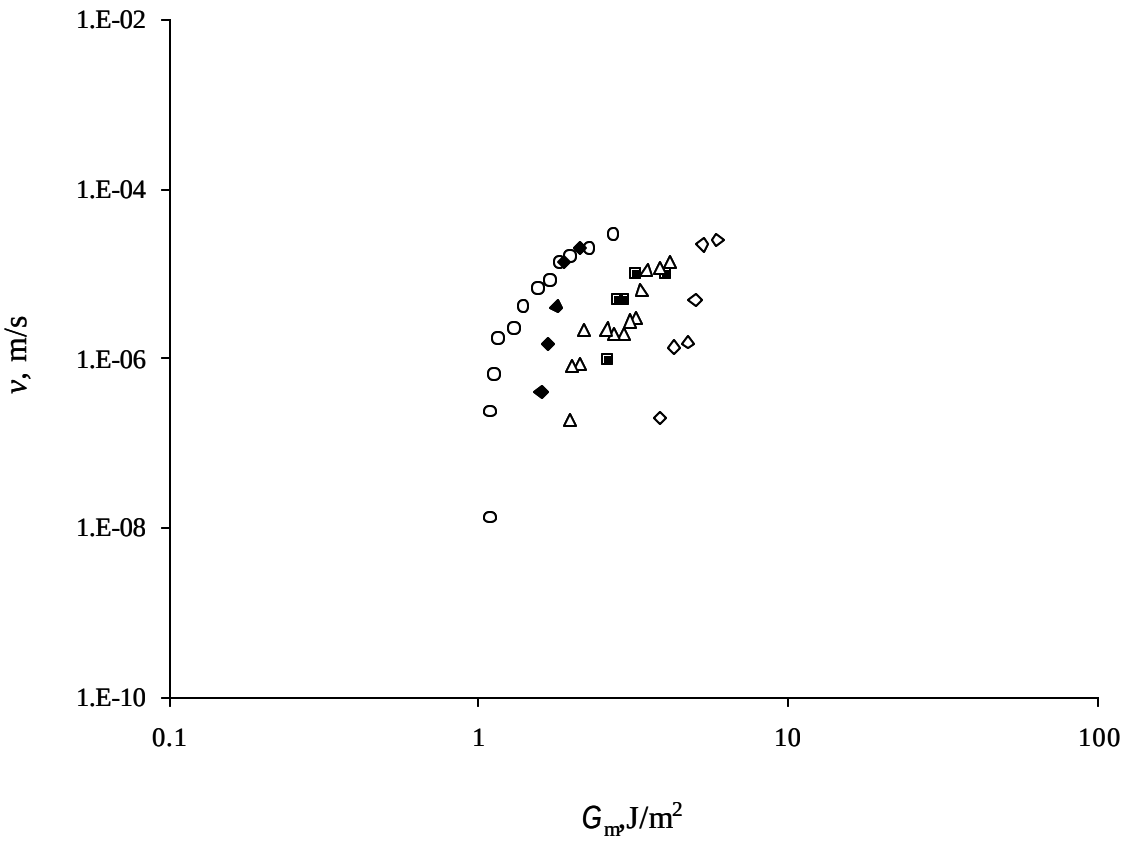

(d)

Figure 2.3 Crack propagation velocity, v (log scale), as a function of strain energy release rate, G, at the crack tip at different temperatures for the *in situ* wedge tests. (a) summary of all the data. (b) data from RT (25°C). (c) data from 40°C. (d) data from 60°C

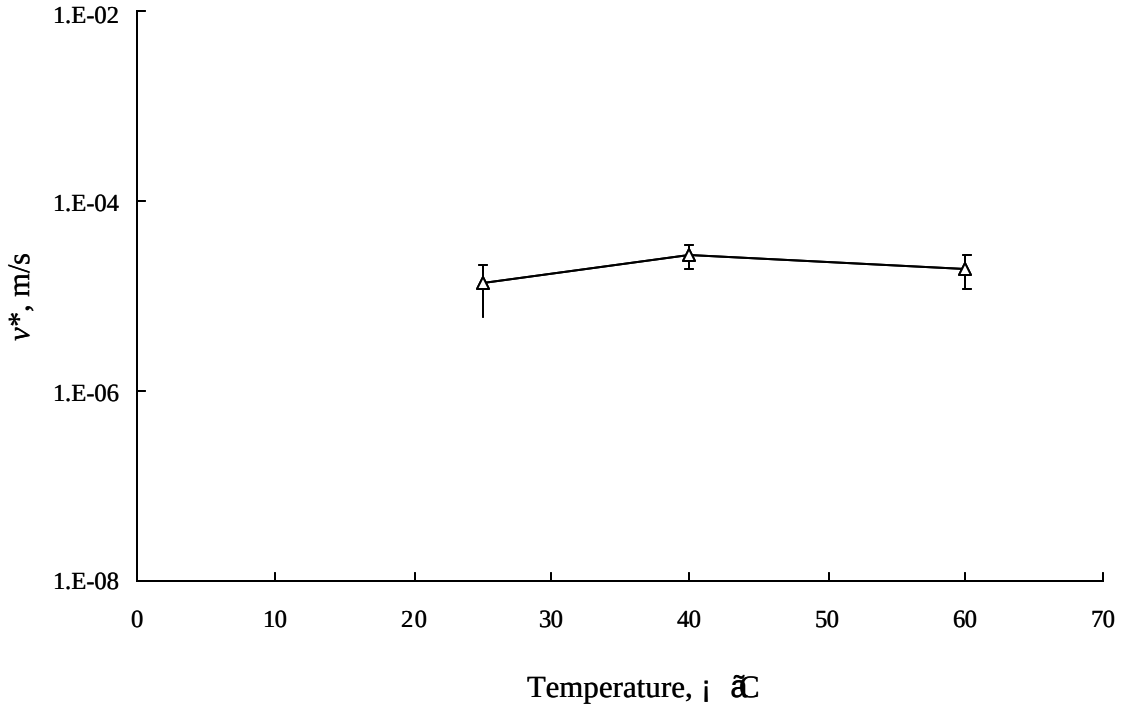

Figure 2.4 Crack propagation velocity, *v* (log scale), at the plateau region as a function of temperature for the *in situ* wedge tests.

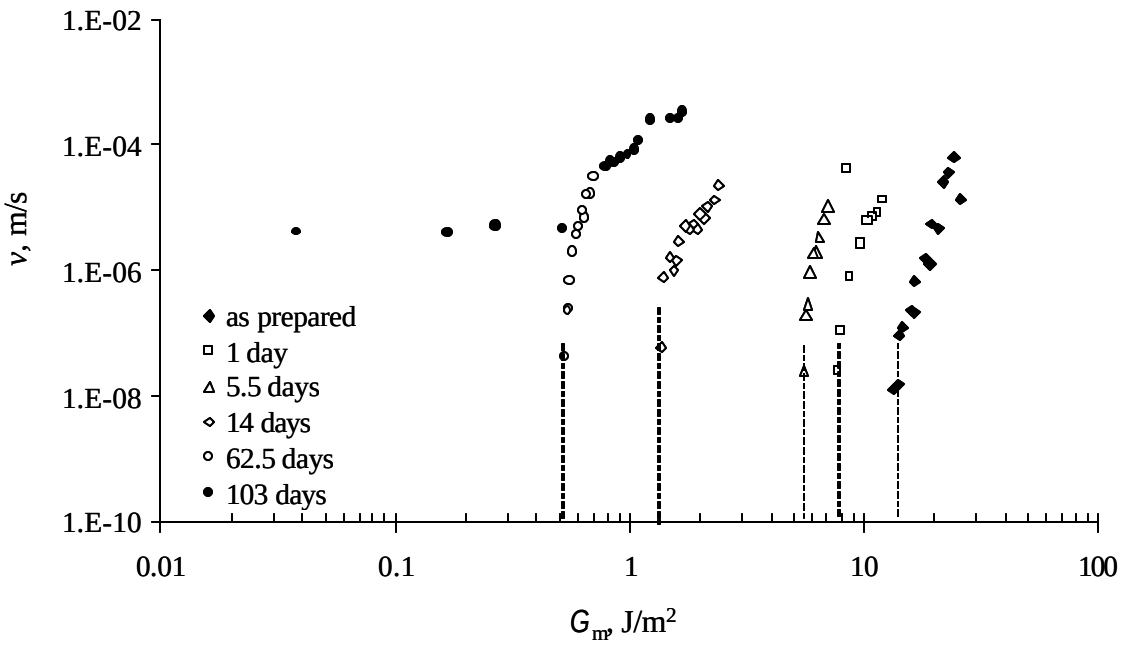
1.E-02
1.E-04
1.E-06
1.E-08
1.E-10
v, m/s
as prepared
1 day
5.5 days
14 days
62.5 days
103 days
0.01
0.1
1
10
100
G_m, J/m^2

(a)

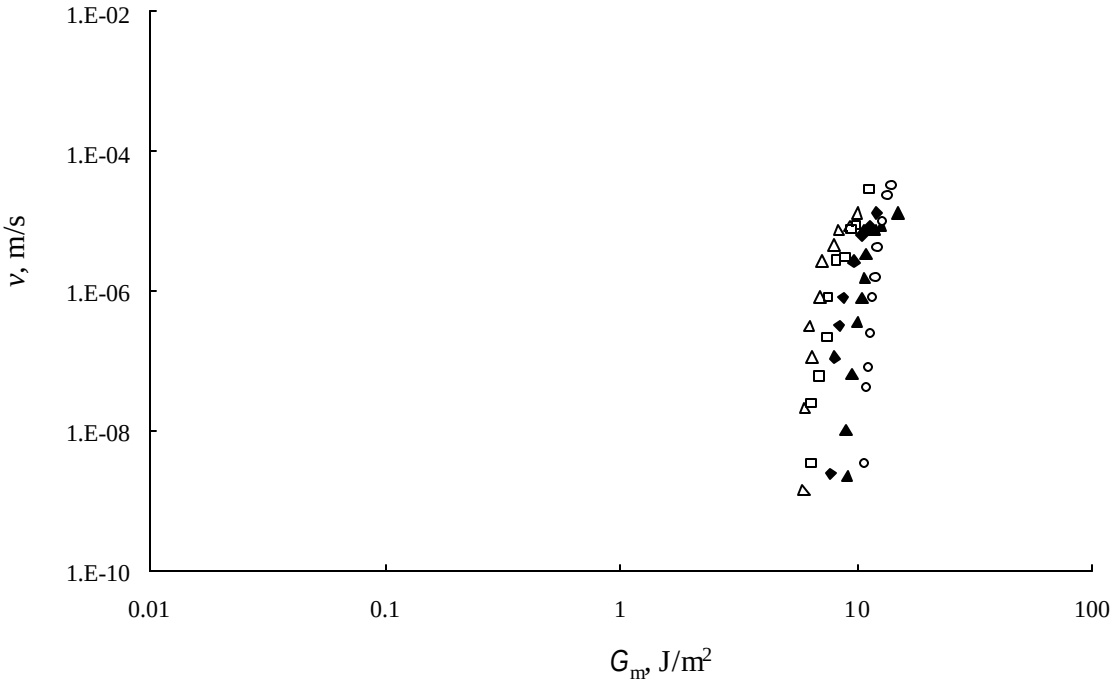

(b)

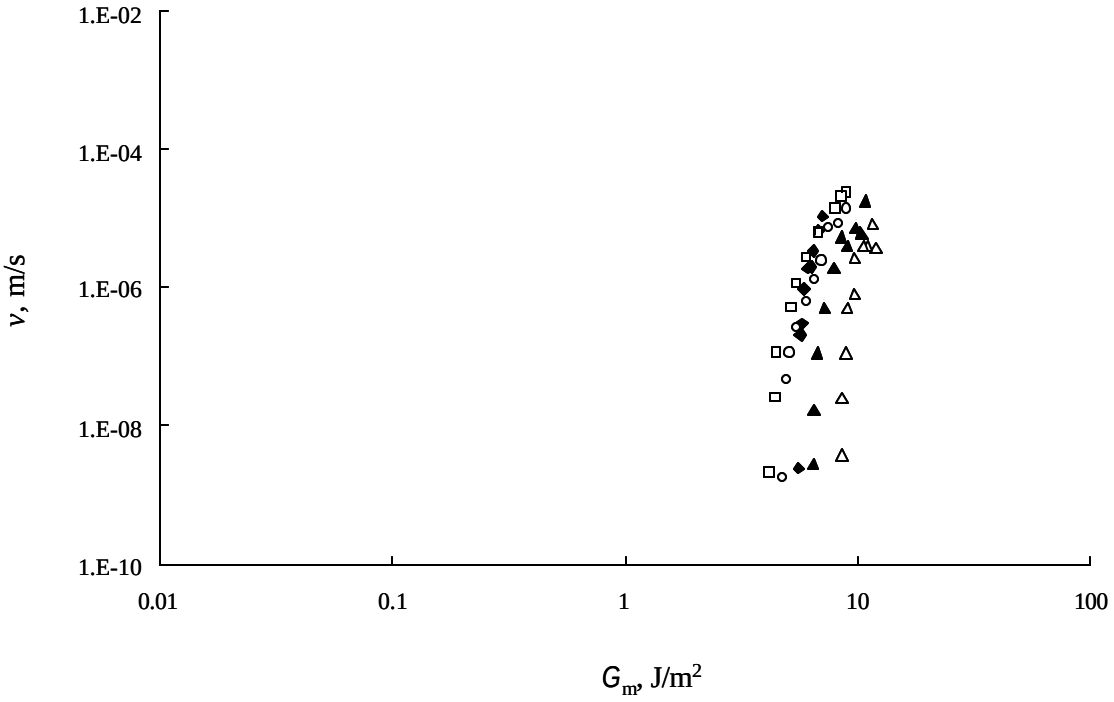

(c)

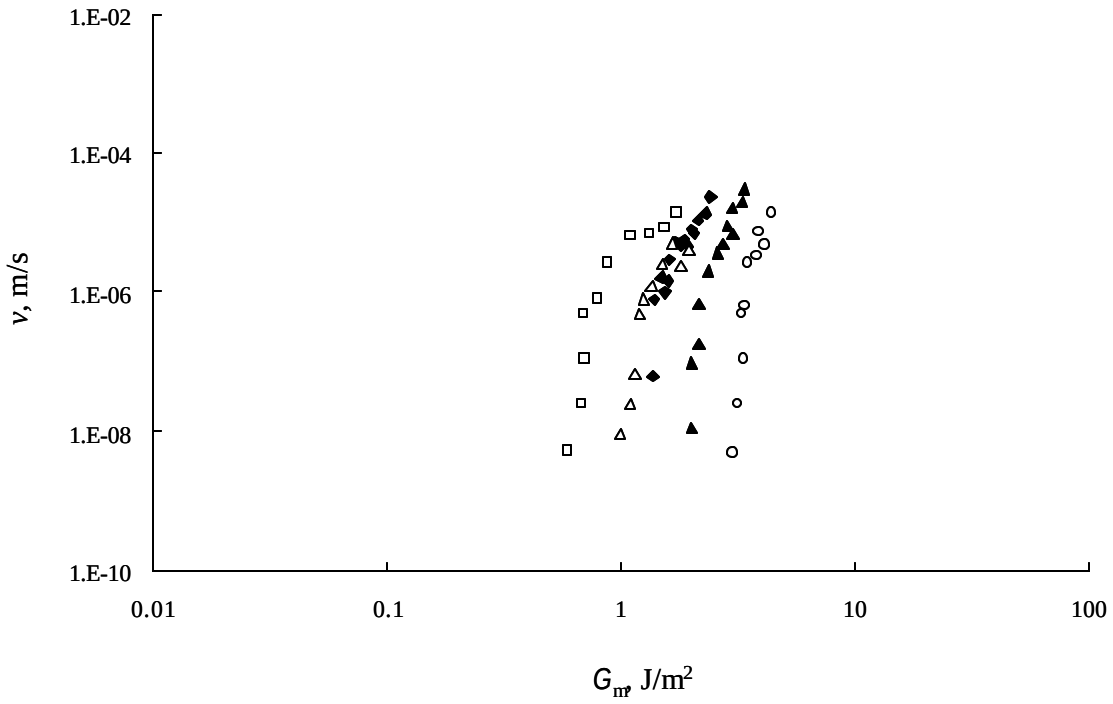

(d)

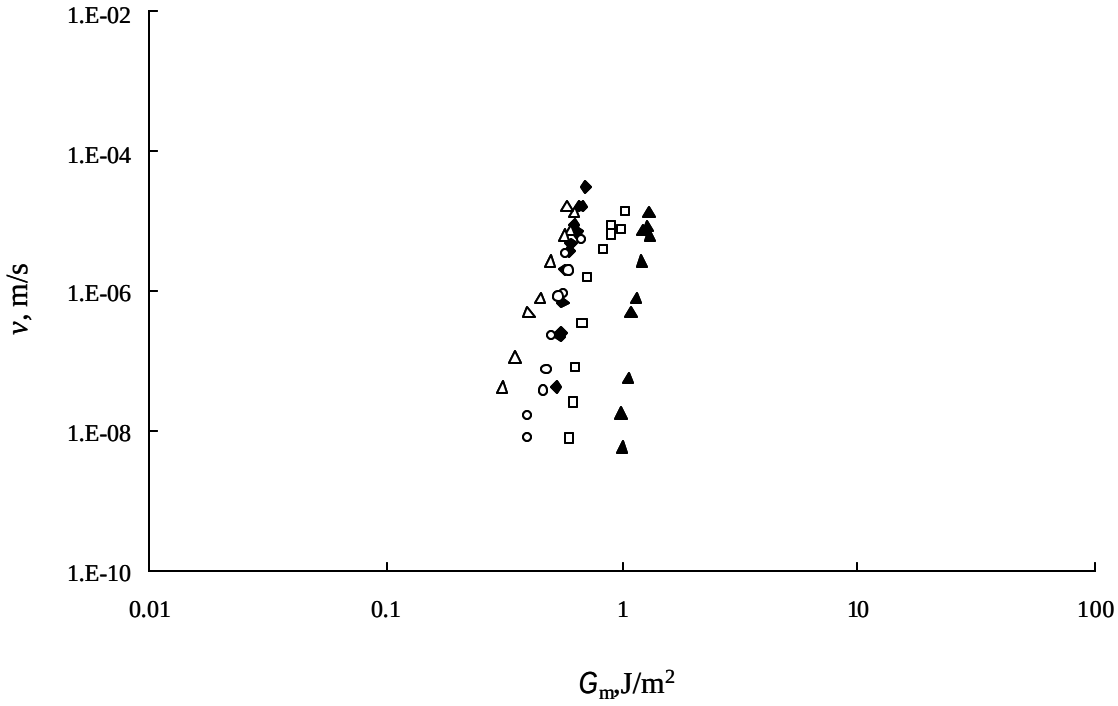

(e)

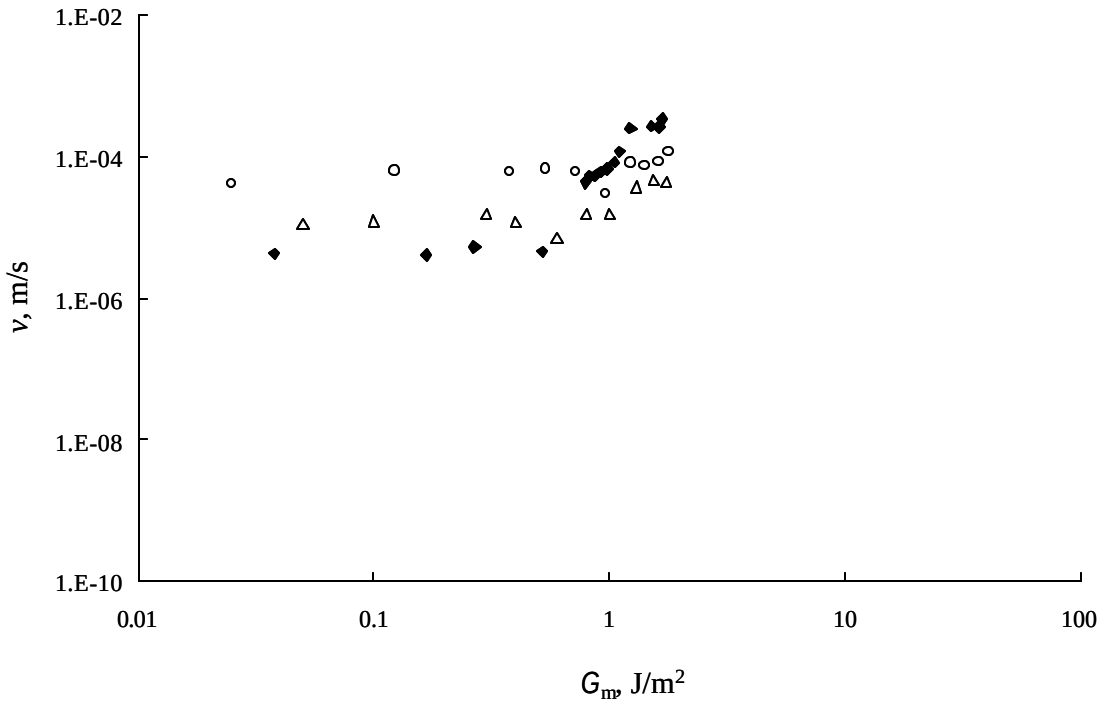

(f)

Figure 2.5 Crack propagation velocity *v* (log scale) as a function of energy release rate *G* (log scale) at the crack tip at room temperature (RT) for the *ex situ* wedge tests. (a) summary of the data. (b) data for the preconditioning time of 1 day. (c) data for the preconditioning time of 5.5 day. (d) data for the preconditioning time of 14 day. (e) data for the preconditioning time of 62.5 day. (f) data for the preconditioning time of 103 day.

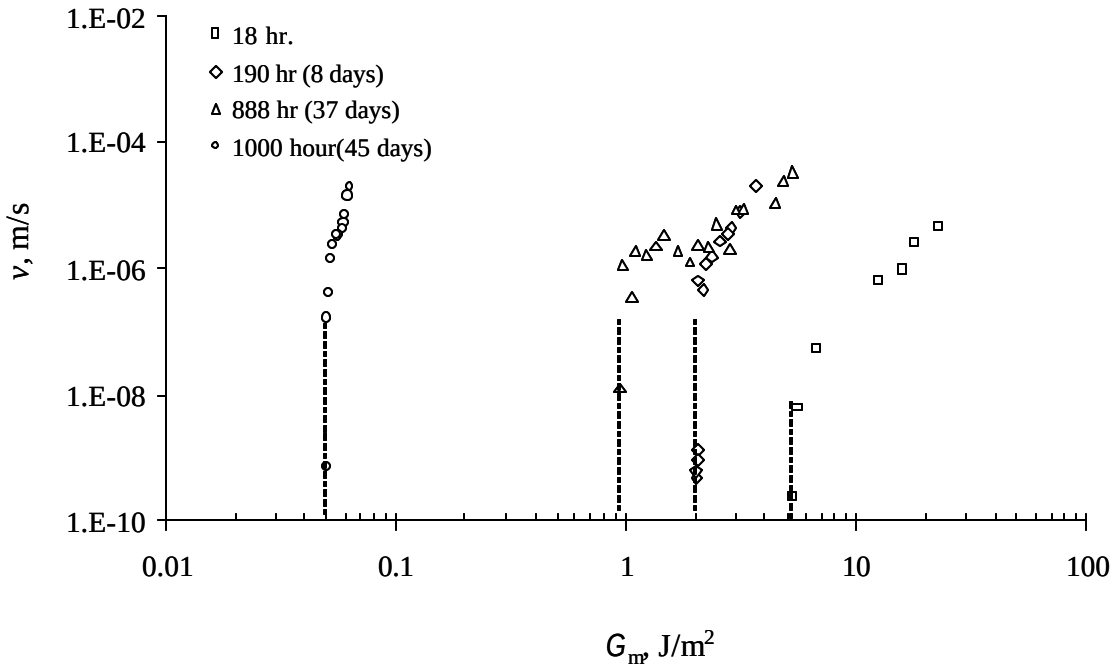
1.E-02
1.E-04
1.E-06
1.E-08
1.E-10
v, m/s
18 hr.
190 hr (8 days)
888 hr (37 days)
1000 hour(45 days)
0.01
0.1
1
10
100
G_m, J/m^2

(a)

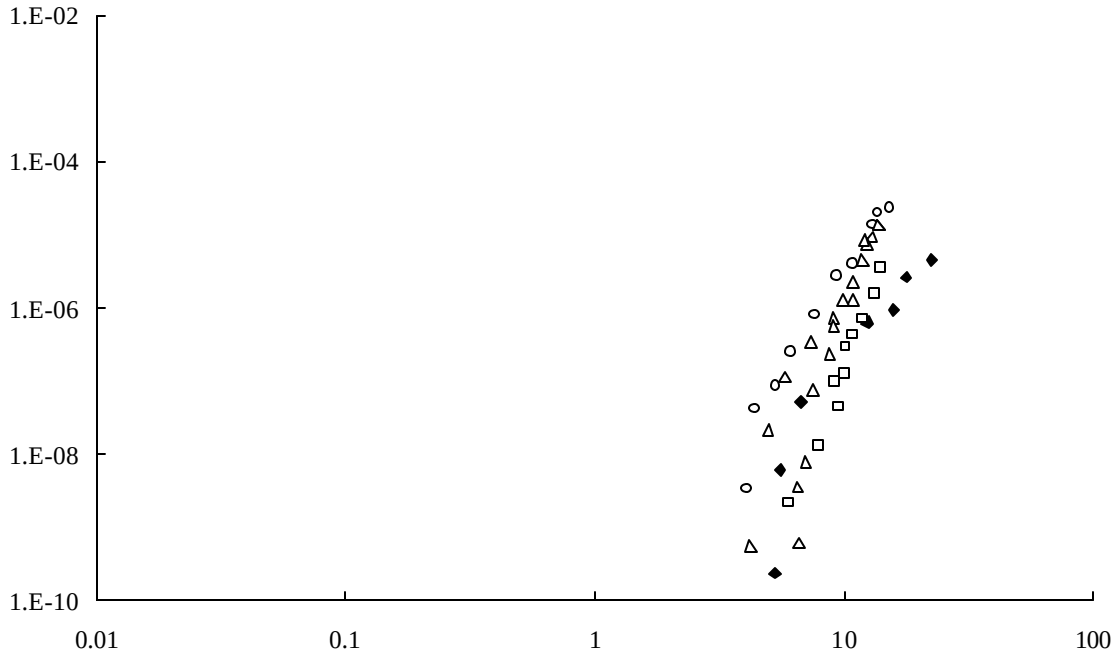

(b)

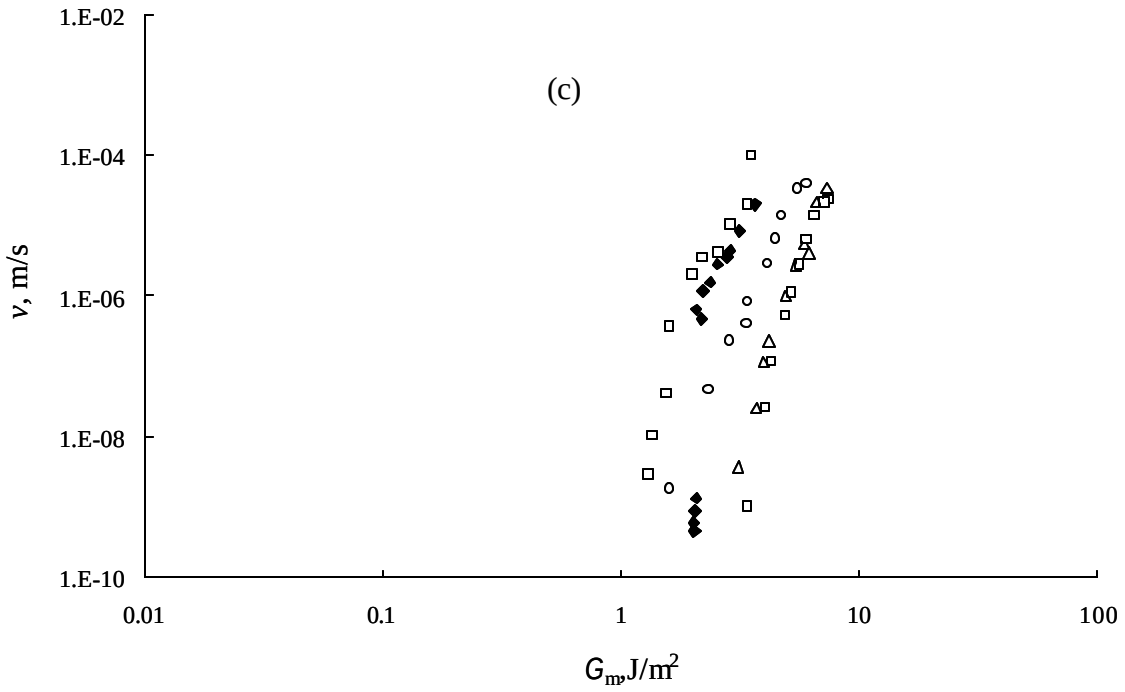
(c)
1.E-02
1.E-04
1.E-06
1.E-08
1.E-10
v, m/s
0.01
0.1
1
10
100
G_m,J/m^2

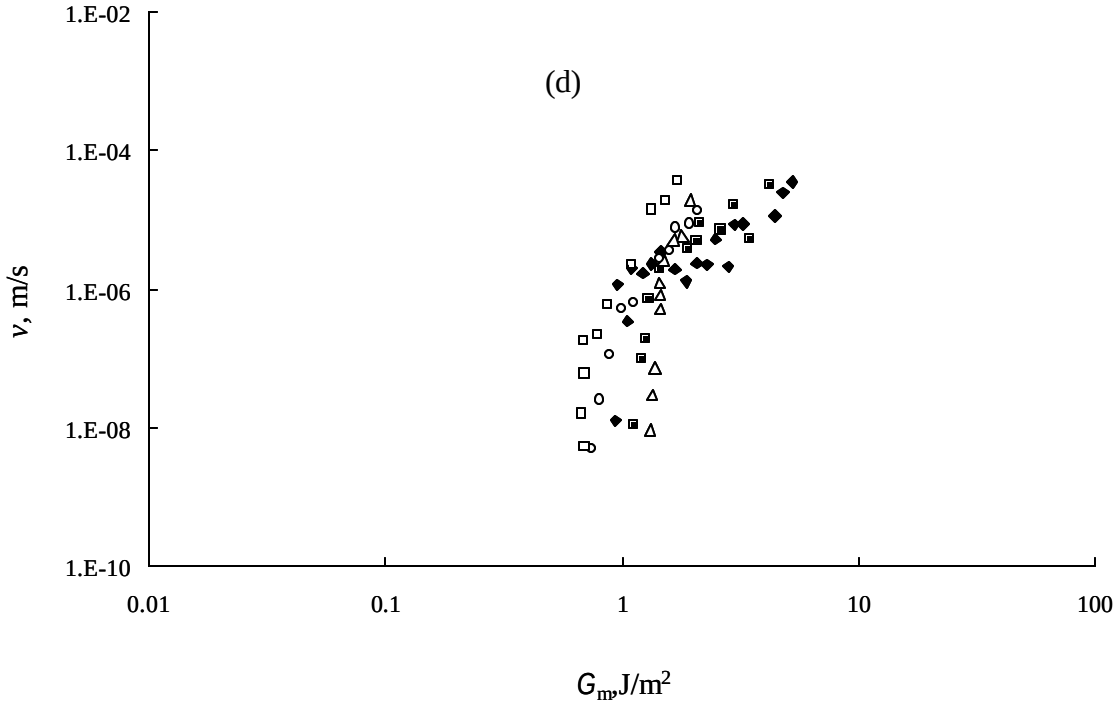
(d)
1.E-02
1.E-04
1.E-06
1.E-08
1.E-10
v, m/s
0.01
0.1
1
10
100
G_m,J/m^2

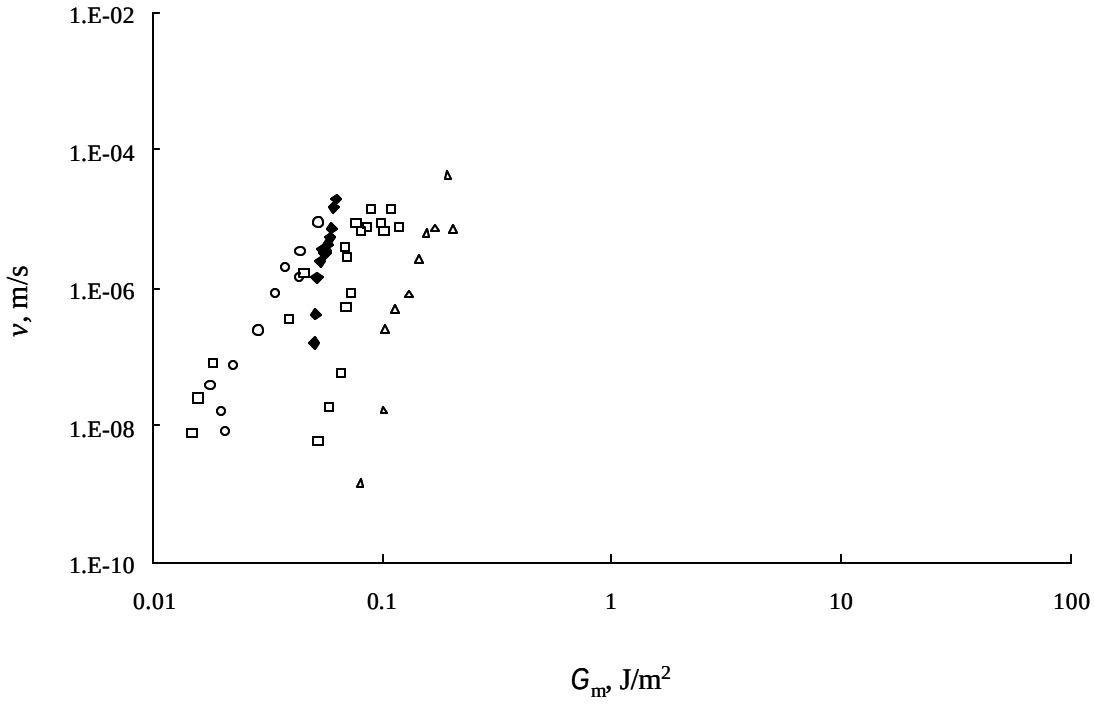

(e)

Figure 2.6 Crack propagation velocity v (log scale) as a function of energy release rate G (log scale) at the crack tip at 40°C for the *ex situ* wedge tests. (a) summary of the data. (b) data for the preconditioning time of 18 hours. (c) data for the preconditioning time of 190 hours (8 days). (d) data for the preconditioning time of 888 hours (37 days). (e) data for the preconditioning time of 1000 hours (45 days).

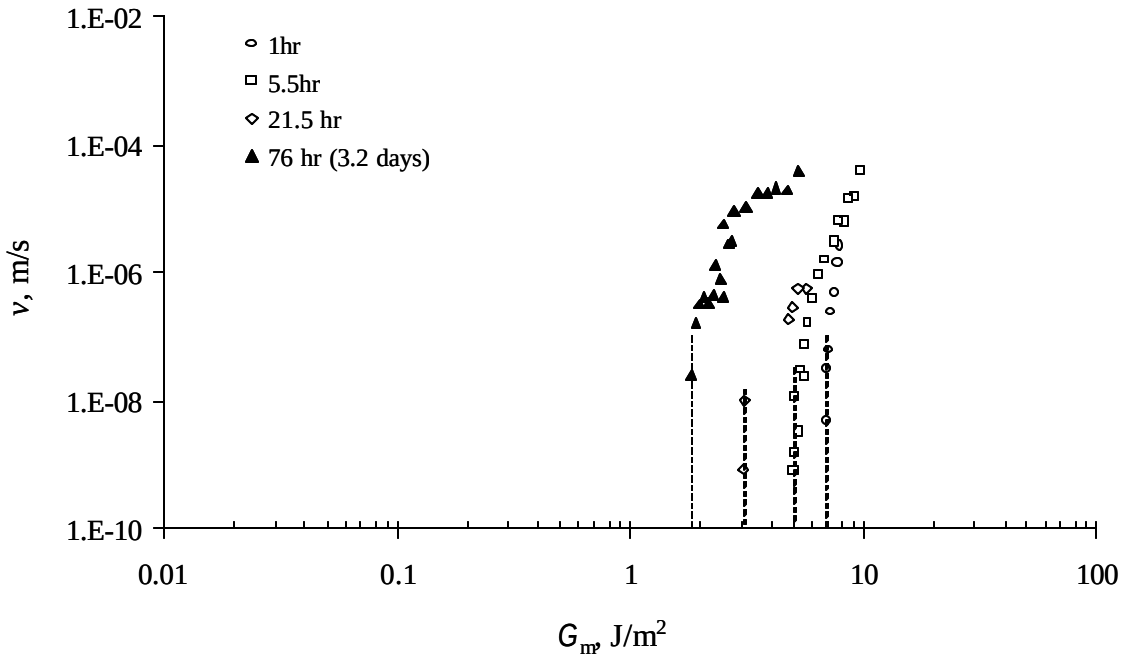
1.E-02
1.E-04
1.E-06
1.E-08
1.E-10
v, m/s
1hr
5.5hr
21.5 hr
76 hr (3.2 days)
0.01
0.1
1
10
100
G_m, J/m^2

(a)

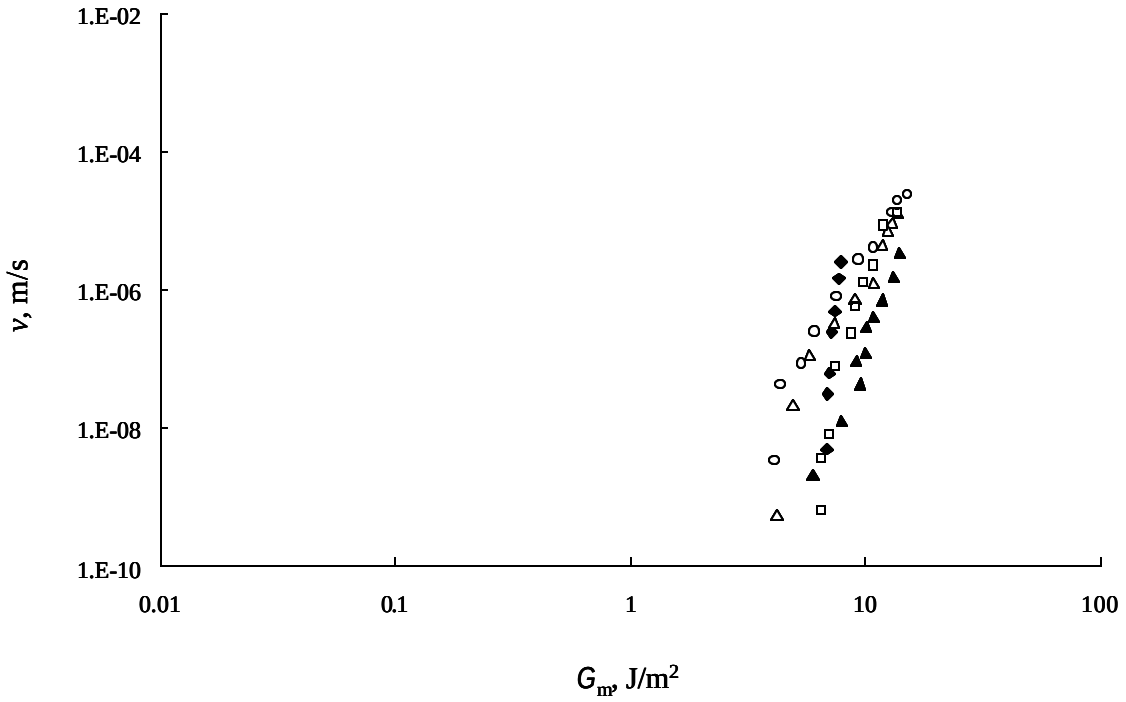

(b)

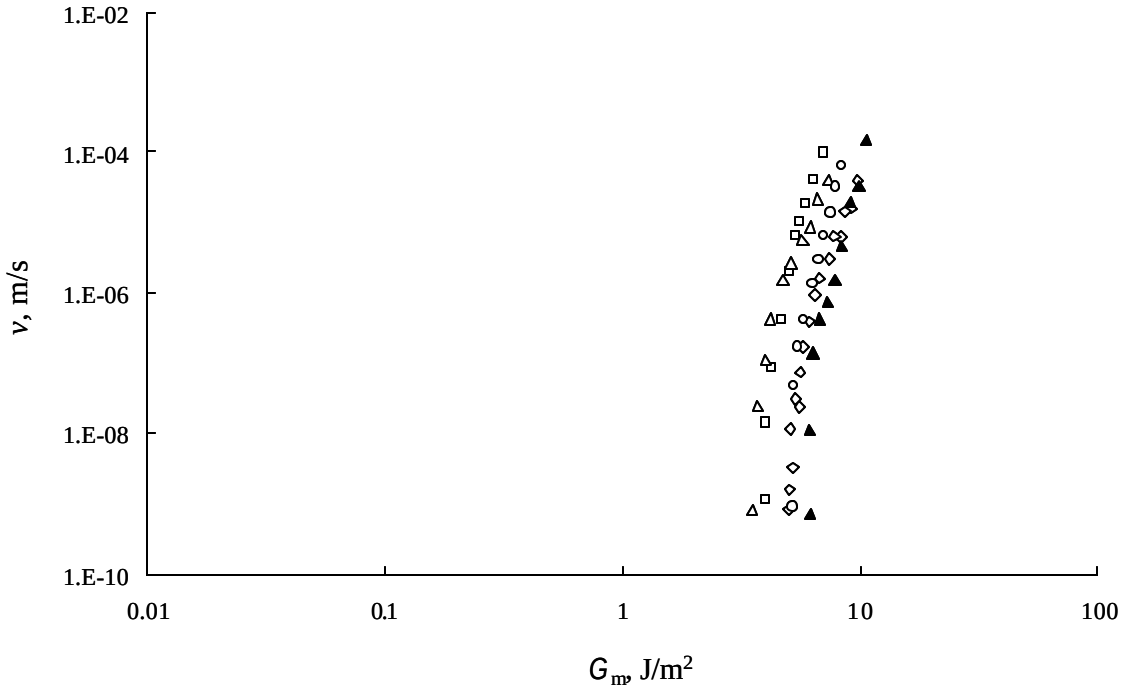

(c)

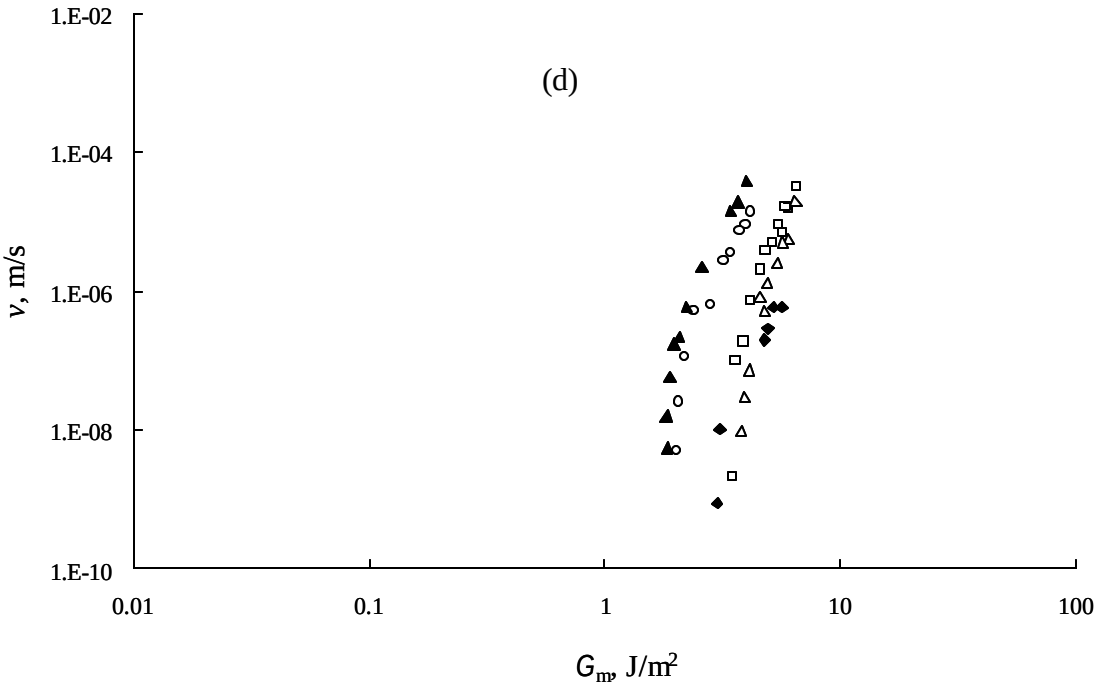
(d)
1.E-02
1.E-04
1.E-06
1.E-08
1.E-10
v, m/s
0.01
0.1
1
10
100
G_m, J/m^2

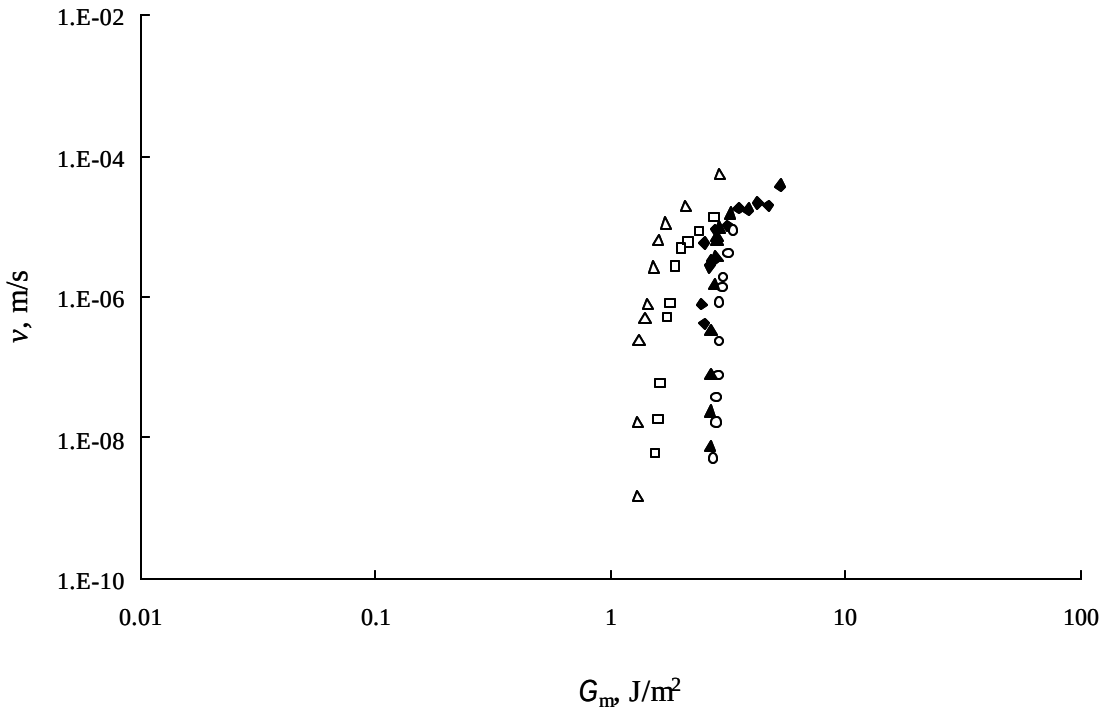

(e)

Figure 2.7 Crack propagation velocity v (log scale) as a function of energy release rate G (log scale) at the crack tip at 60°C for the *ex situ* wedge tests. (a) summary of the data. (b) data for the preconditioning time of 1 hour. (c) data for the preconditioning time of 5.5 hours. (d) data for the preconditioning time of 21.5 hours. (e) data for the preconditioning time of 76 hours (3.2 days).

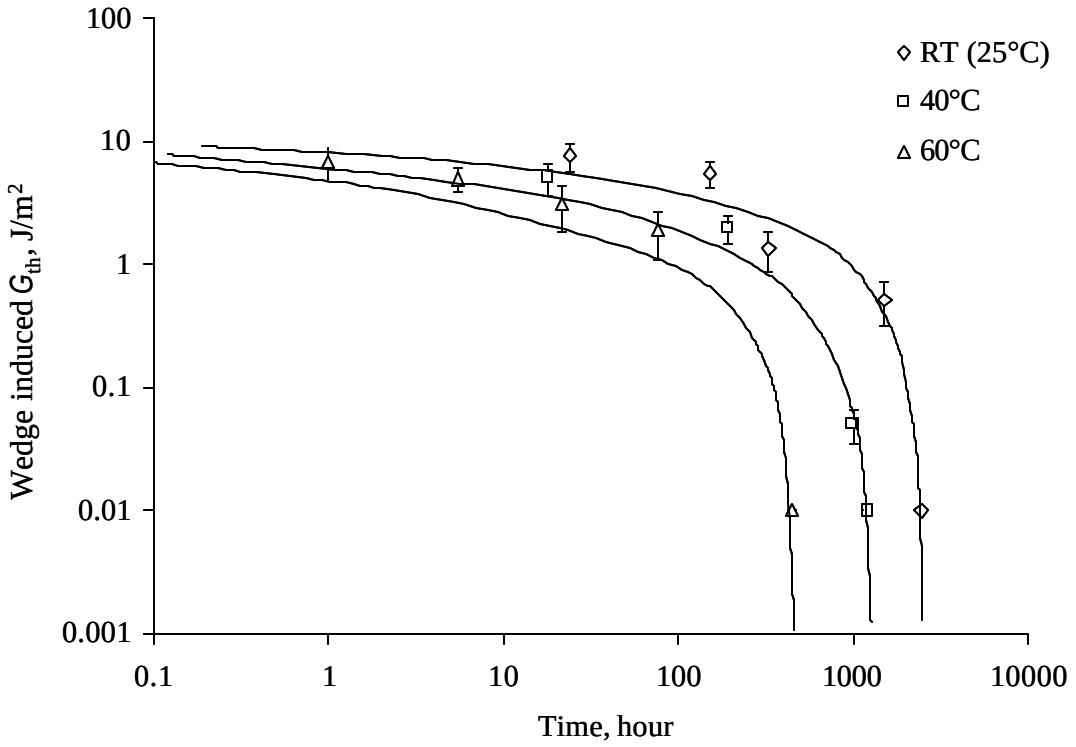

Figure 2.8 Threshold energy release rate G_{th} (log scale) caused by a wedge load at the crack tip as a function of pre-conditioned time (log scale) at three different temperatures. The solid lines are added to clarify the trend of the data. The error bars represent one standard deviation of the data at each testing condition.

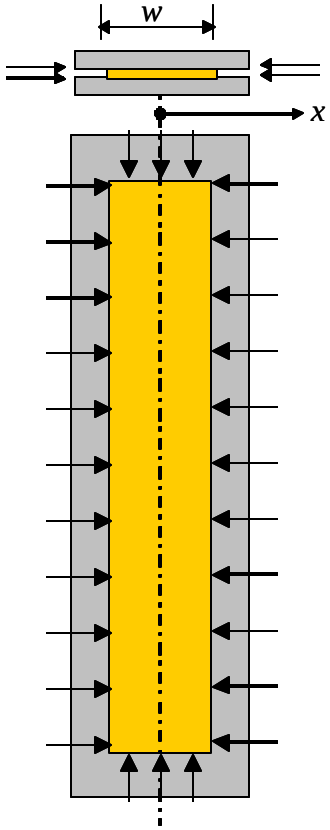

Figure 2.9 Schematic of a DCB specimen showing interfacial diffusion path. The arrows represent how water ingresses into specimen.

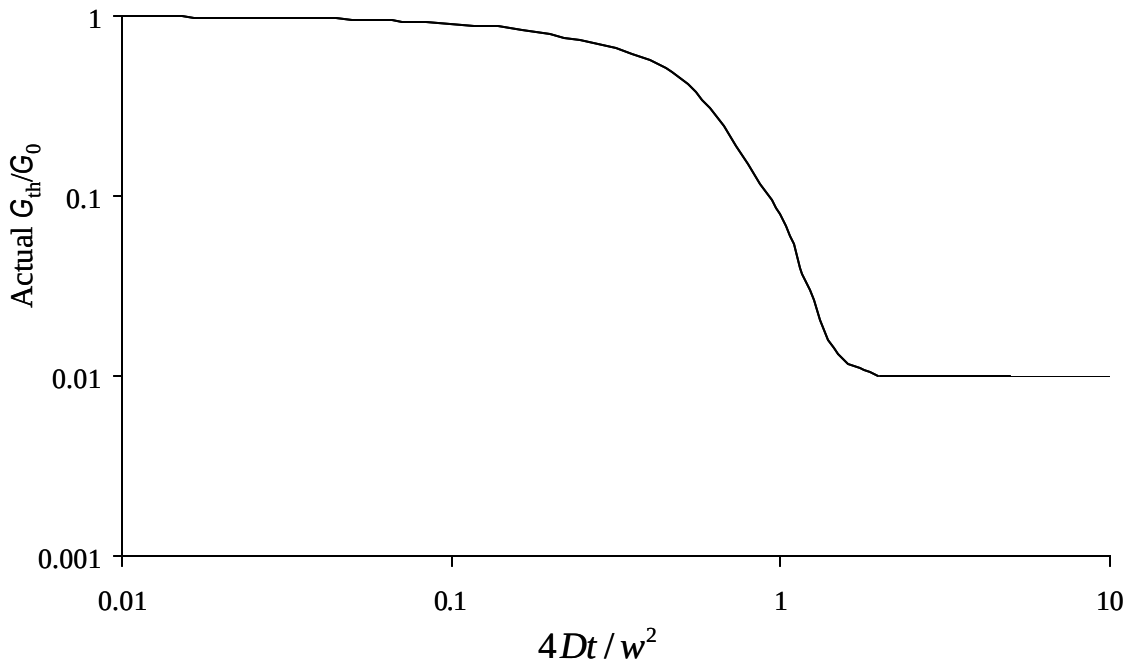

Figure 2.10 Theoretical G_{th}/G_{th0} (on log scale) as a function of normalized pre-conditioning time (on log scale) without considering residual stress. G_{th} stands for the threshold value of actual strain energy release rate after pre-conditioning, while G_0 stands for threshold strain energy release rate prior to pre-conditioning.

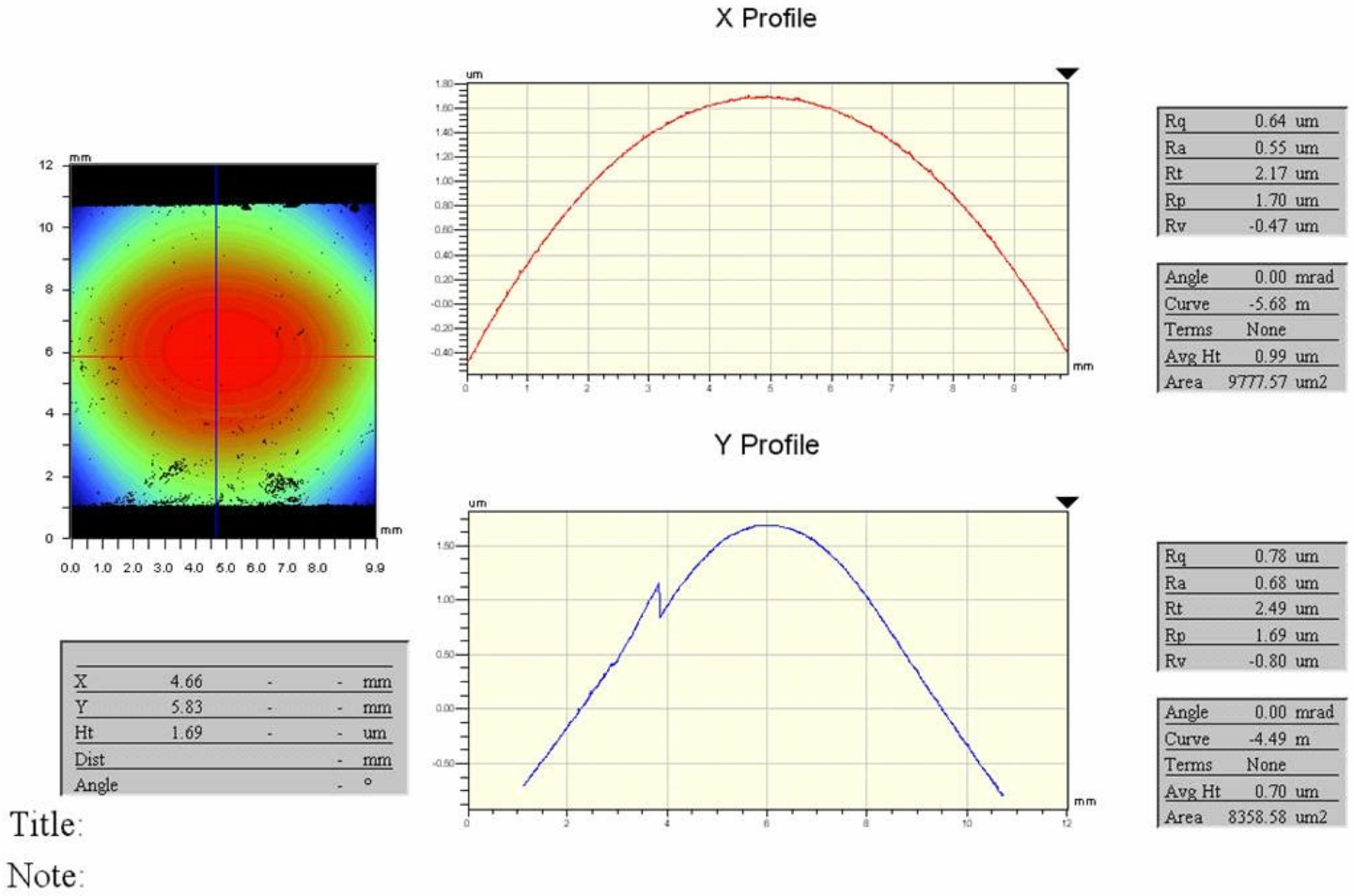

Figure 2.11 Screen display of the optical profiler. The two curves are the deflection profiles along two directions on the specimen surface.

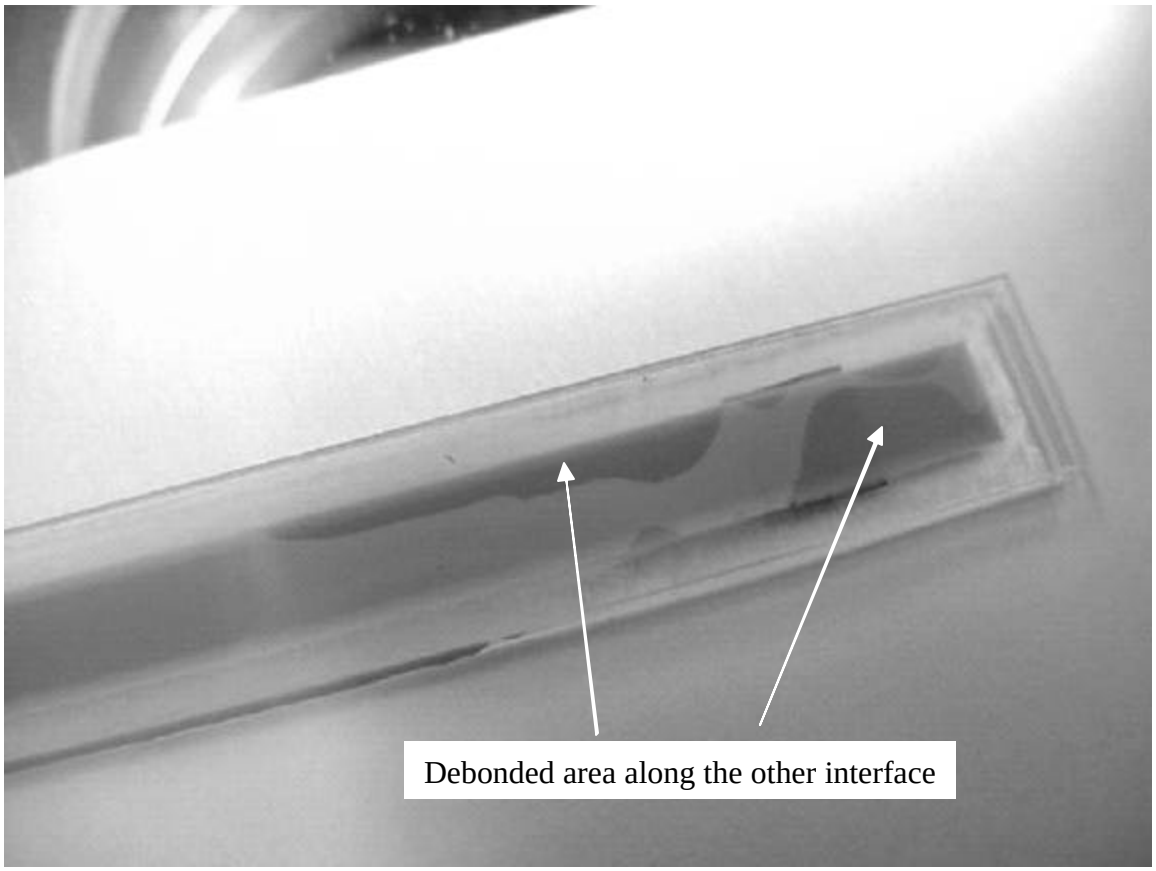

Figure 2.12 Photograph showing the debonding along the glass/epoxy interface due to thermal residual stress.

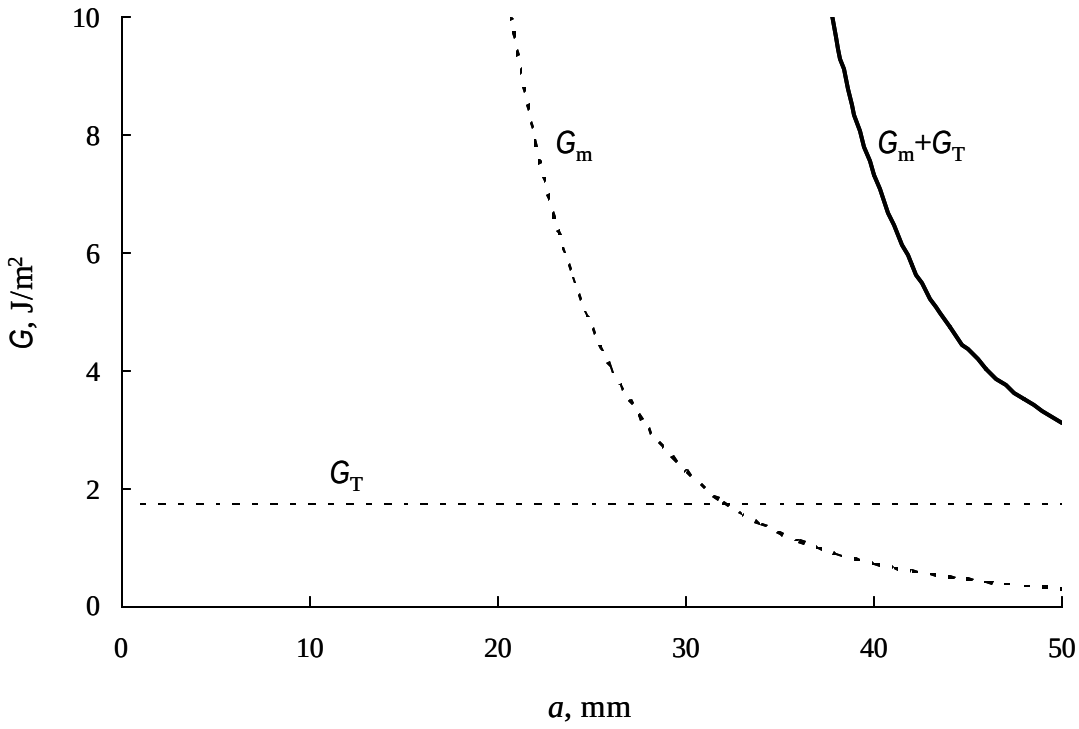

Figure 2.13 Dependence of G_m and G_T on crack length, a, for the wedge specimens tested.

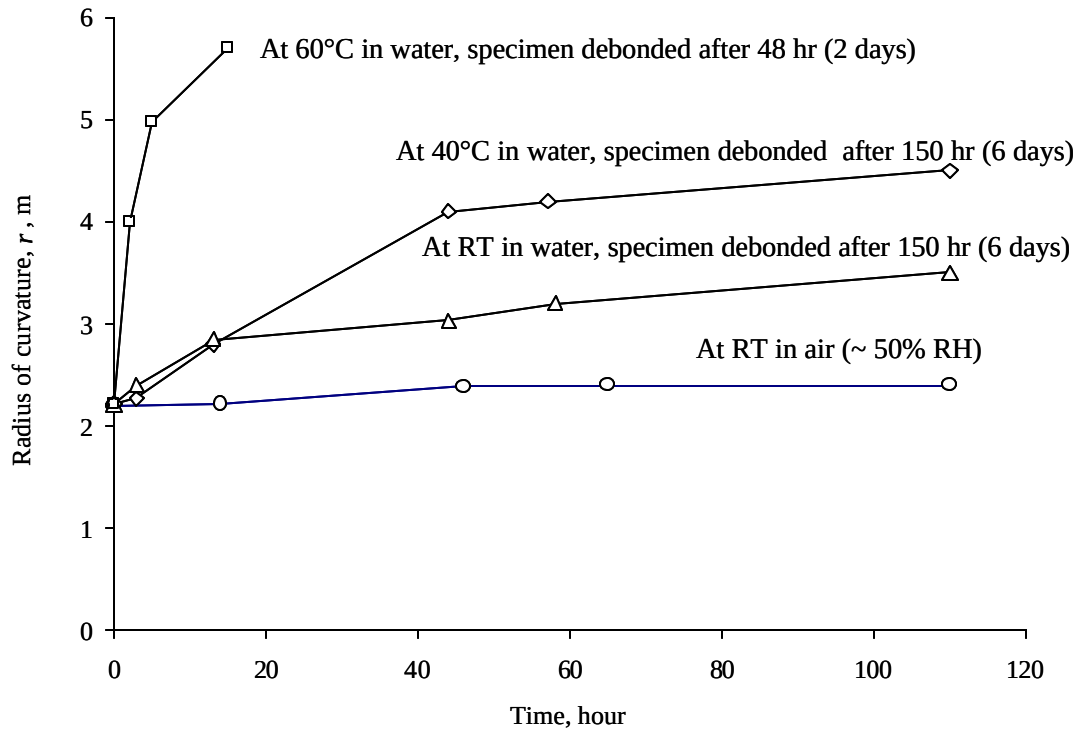

Figure 2.14 Radius of curvature of bimaterial strips as function of time submerged in water at different temperatures.

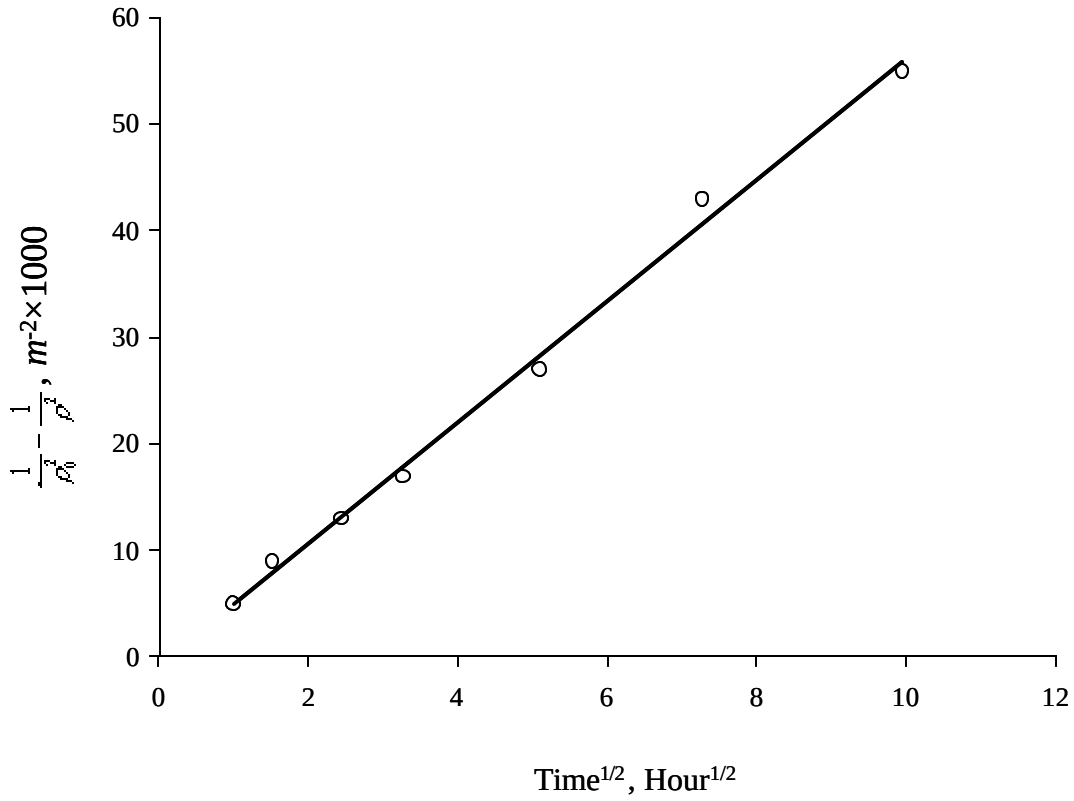

Figure 2.15 Change of $1/\rho^2$ as a function of square root of time for a pre-conditioned sandwich specimen. ρ stands for the radius of curvature of the bimaterial part of the debonded sandwich specimen after preconditioning.

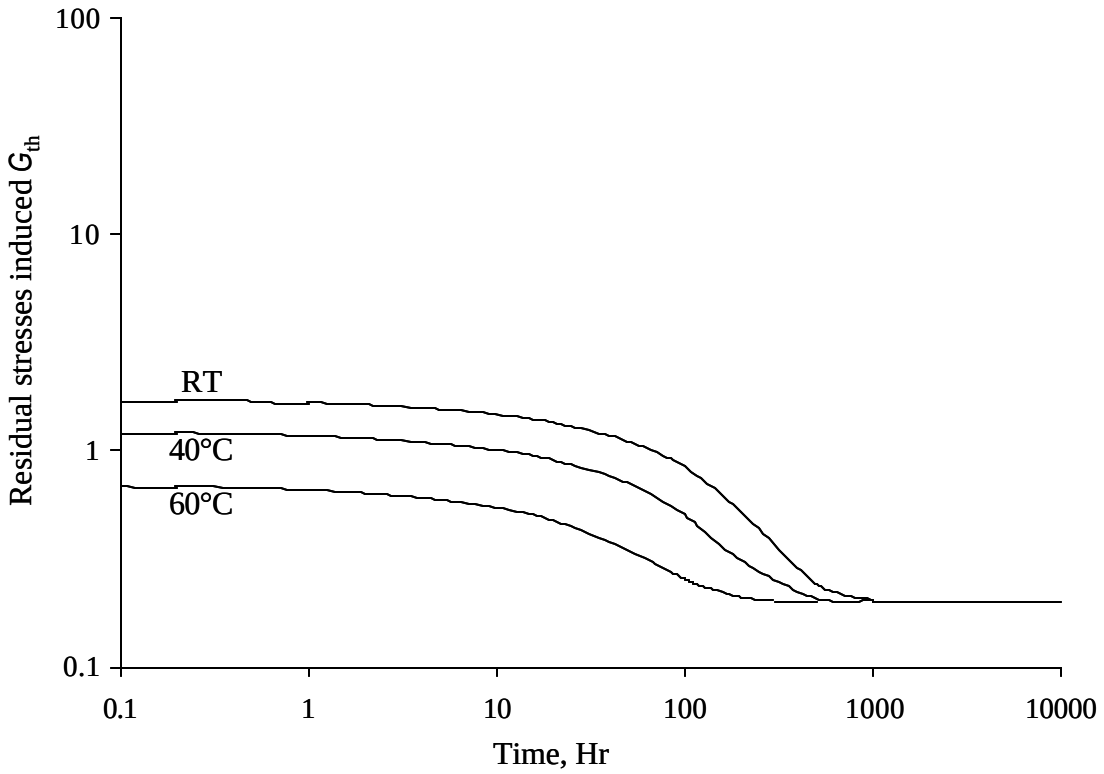
100
10
1
0.1
Residual stresses induced G_{th}
RT
40°C
60°C
0.1
1
10
100
1000
10000
Time, Hr

(a)

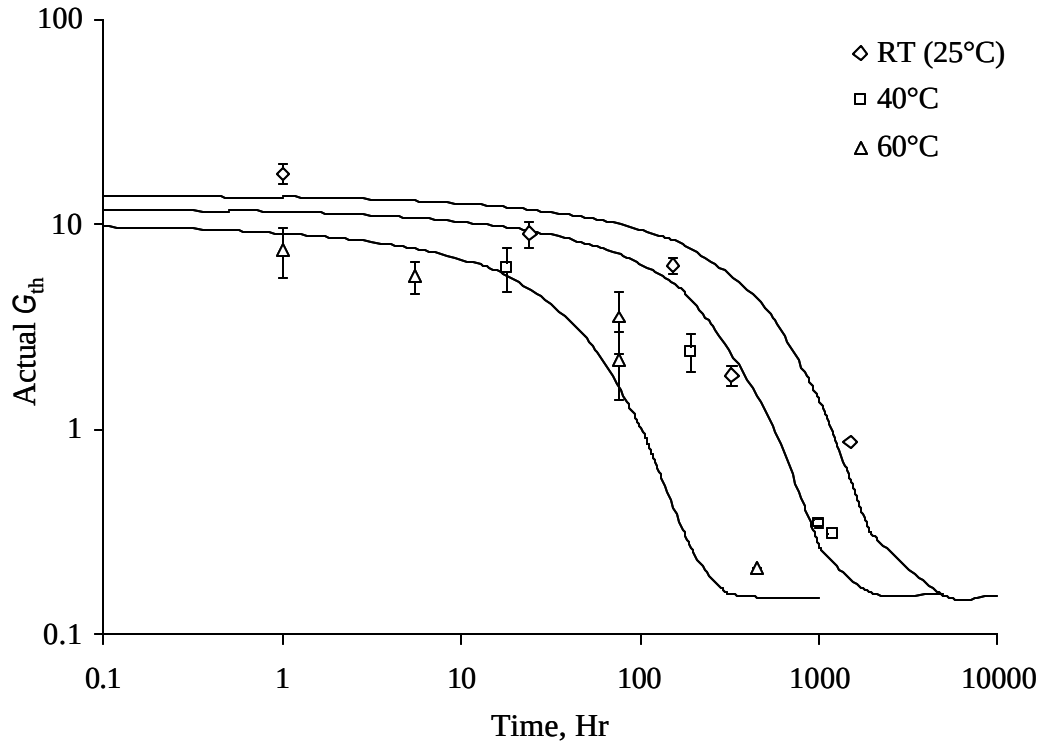

(b)

Figure 2.16 The prediction of the model for the three temperatures. (a) The predicted thermal stresses induced threshold energy release rate G_{th} (log scale) as a function of time (log scale). (b) The actual G_{th} (log scale) as a function of time (log scale). The solid lines are predictions by the model described in the text and data points are the additives of the experimental data in Figure 2.8 and Figure 2.16 (a).

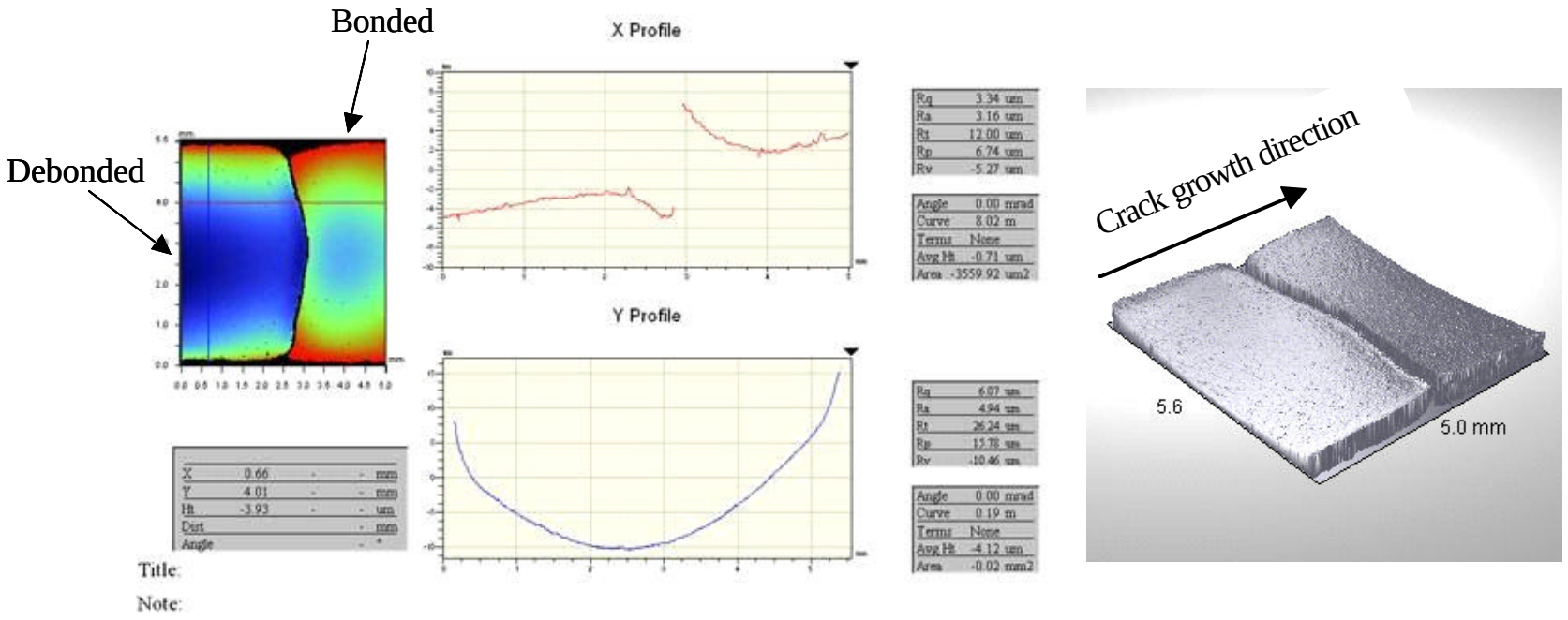

Figure 2.17 Images from the optical profiler that was used to measure the crack front profile of the post-tested *in situ* wedge test specimens. The two curves are the deflection profiles along two directions on the specimen surface.

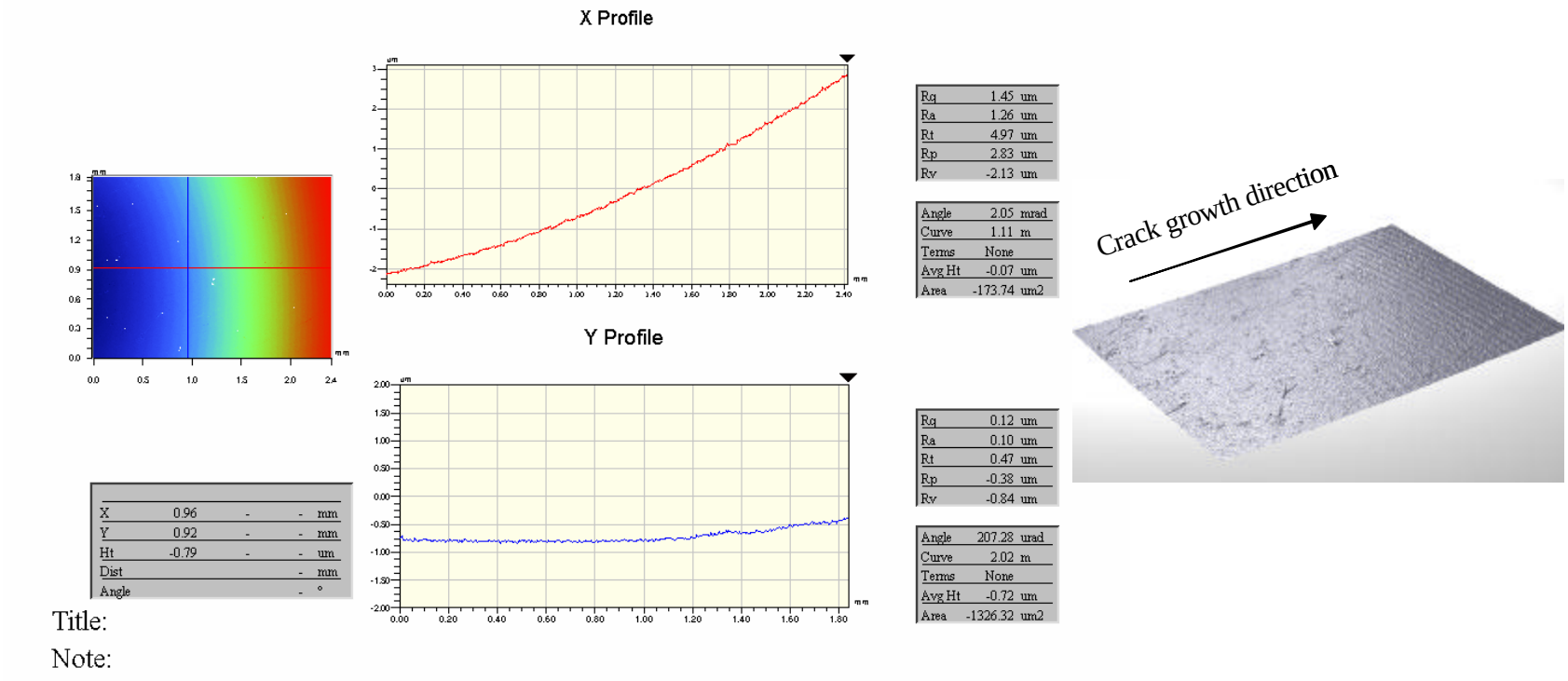

Figure 2.18 Images from the optical profiler that was used to measure the crack front profile of the post-tested ex *situ* wedge test specimens. The two curves are the deflection profiles along two directions on the specimen surface.

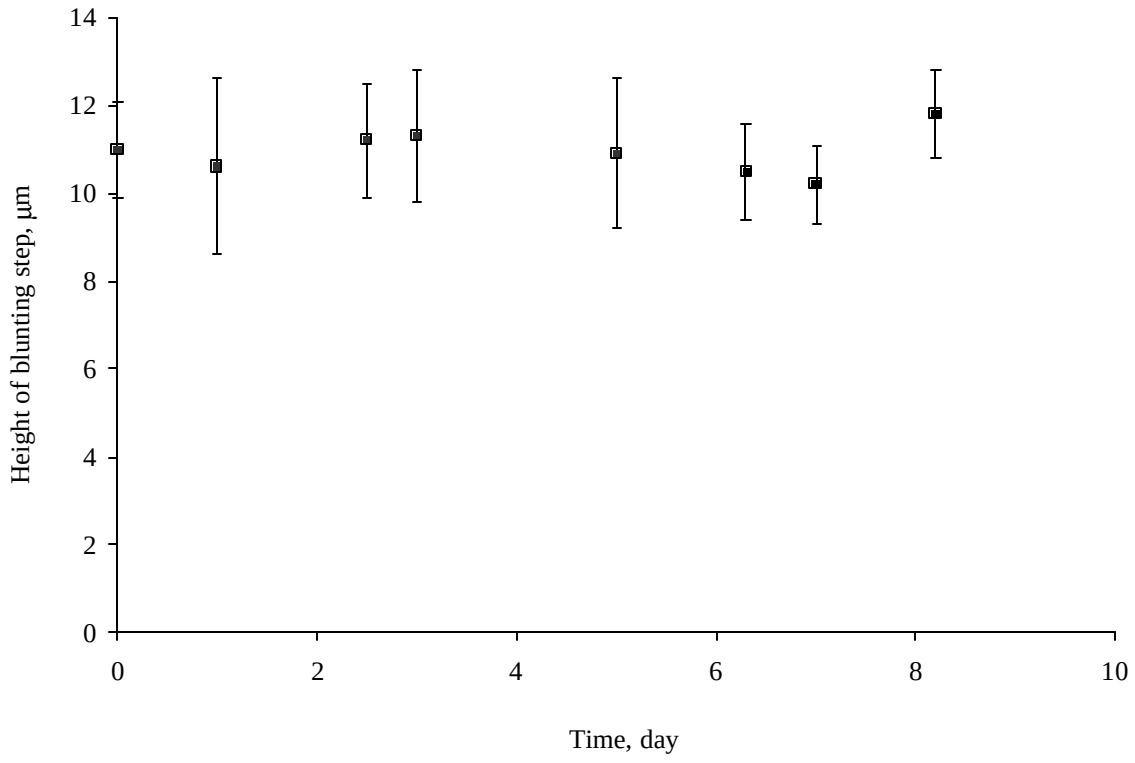

Figure 2.19 Step height at crack tip shown in Figure 2.17 as a function of time in dry air at elevated temperature (70°C). The height is referred with the lower surface in Figure 2.17.

CHAPTER 3

THE EFFECT OF RESIDUAL STRESS ON THE ENERGY RELEASE RATE OF A WEDGE TEST SPECIMEN

(to be submitted to *International Journal of Adhesion and Adhesives*)

3.1 Abstract

Changes in interfacial strain energy release rate caused by thermal residual stresses in a triple-layered specimen were analyzed. The method is based on linear elastic fracture mechanics and simple beam theory. The curvature of a bimaterial strip was chosen to characterize the residual stress in the specimen, and the strain energy release rate, caused by either tensile or compressive residual stresses in the adhesive, was derived for an asymmetric double cantilever beam (ADCB) geometry. The contributions of the thermal residual and mechanical stresses to the global energy release rate were analyzed. The thermally induced energy release rate, G_T, is found to be independent of crack length, but is a function of residual stress level and the geometric and material parameters of the specimen.

Keywords: thermal residual stresses, double cantilever beam, interfacial fracture energy, asymmetric double cantilever beam, wedge specimens, biomaterial curvature.

3.2 Introduction

When layers of dissimilar materials are bonded, differences in the coefficient of thermal expansion (CTE), combined with a temperature change relative to the stress-free state, result in thermal residual stresses. These stresses, along with edge flaws, may result in the development of interfacial cracks. In particular, because the analysis of thermal stress in a bimaterial beam caused by a uniform change in temperature provides fundamental insight to the understanding of thermo-mechanical behavior of multilayered materials and electronic packaging, it has received considerable attention in the literature. For the purpose of engineering applications, simple solutions based on strength of materials theories clearly indicate the major factors affecting thermal stresses. One of the earliest models was developed by Stoney [1]. He determined the residual stress in a coating by assuming the thickness of the coating layer was small compared to the substrate. Timoshenko [2] analyzed the curvature of a bimaterial strip based on the observation that the interfacial stresses in a bimaterial beam are highly localized at the free edges. Timoshenko's model leads to simple, yet sufficiently accurate formulae for overall deflection and longitudinal stress. However this model does not predict any detail about the distribution of the interfacial stresses. Timoshenko's model has been extended to multilayered systems by Pan *et al.* [3]. Since the interfacial residual stresses dominate interfacial failure of multilayered materials and electronics packages, considerable attention has been devoted to the analysis of interfacial stresses [4-8]. Suhir [5] developed a modified beam model based on the concept of longitudinal "interfacial compliance", which assumes that the deviation of the longitudinal interfacial displacement at a point is proportional to the interfacial shear force at that point. Due to its impressive simplicity, this model received wide attention and was also extended to multilayered materials. On the other hand, Suhir's model [5] cannot meet the required self-equilibrium condition for the interfacial normal (peeling) stress. As a result, Suhir [7] revised his model by further considering the normal "interfacial compliance". However the revised model resulted in a complicated solution because of the sixth-order differential equations. Recently Ru [9] modified Suhir's model [7] by assuming that the deviation of the longitudinal interfacial displacement at a point depends not only on the

interfacial shear force, but also on its second gradient at that point. This model yields a simpler solution than Suhir's model [7], and satisfies all boundary conditions at the free edges. The one dimensional beam analysis was also extended to two dimensional cases [10, 11] in which a cylindrical shape was assumed for the deformed plate. Senne, *et al* [12] analyzed the interfacial stresses in a polymer wearing surface/FRP deck bond due to thermal loading using a curvature method.

Small deformation theory is adequate for determining the strain and stress fields for many applications. There also exist, however, a number of practical situations where large elastic deformations, i.e. geometrically nonlinear deformation, occur. The subject of large rotations of elastic laminates received much attention [13-15]. In these analyses, the out-of-plate deflection and mid-plane normal strains are approximated by a second-order polynomial whose unknown coefficients are determined by minimizing the total strain potential energy and by identifying the equilibrium shapes of the plate. While classic plate theory predicts a single shape with a unique curvature at low stresses, three equilibrium shapes are feasible after the bifurcation stress or temperature using such methods. The single shape at low stresses is a spherical geometry for isotropic thin films on substrates, and the post-bifurcation configurations are an unstable spherical and two stable ellipsoidal shapes with two different principal curvatures along two mutually orthogonal in-plane coordinates. Experimentally, the bimaterial technique has been applied to measure the residual stress [16, 17] and material properties of coating system [18].

Interfacial fracture mechanics for a layered structure has also been explored by many people [19-24] for more than 30 years. The mathematical solutions indicate that interfacial fracture is often mixed mode (combination of mode I (open) and II (forward shear)), even when the geometry and loading are otherwise symmetric with respect to the crack. Another unique feature of interfacial fracture is the oscillation of stress and displacement field in the vicinity of the crack tip, which leads to predicted crack surface interpenetration, due to the mathematical features of the problem solution. Interfacial fracture mechanics of adhesive joints with the existence of residual stress has also been studied [25-29]. Gaudette *et al.* [28] examined the evolution of the energy release rate

for a crack in a three-layered system, composed of elasto-plastic materials, subject to monotonic thermal loading, and found the existence of characteristic temperatures which mark the bounds between the three regimes of interfacial fracture: elastic, elasto-plastic, and fully plastic. Using an asymmetric double cantilever beam (ADCB) geometry, Jiao *et al.* [29] reported the solution of the strain energy release rate for an ADCB specimen combined with thermal stress, which is due to the CTE difference between the two ADCB adherends. However, residual stresses in many adhesive DCB experiments are caused by the different CTE of the adhesive and adherends, thus, the Jiao's solution is not applicable. Nairn [30] investigated the effect of residual stresses on strain energy release rate on a symmetric DCB specimen using a thermo-elasticity method. His analysis was limited because the debond is assumed to be located along the middle of adhesive layer, and the mechanical load needs to do external work during debond growth. However, if the end displacement of the specimen is fixed during debond growth, as in wedge tests, the strain energy caused by residual stress is still released, and thus contributes to the total energy release rate.

In this chapter, the interfacial energy release rate, G_T, caused by thermal stresses in a DCB/wedge test specimen is calculated based on simple beam theory and linear elastic fracture mechanics (LEFM). Thermal stress within the adhesive layer was measured using the curvature of a bimaterial beam.

3.3 Calculations

3.3.1 G calculation for a wedged DCB geometry considering adhesive layer

Based on simple beam theory, the strain energy release rate, G_m for an ADCB specimen with an end opening, Δ, as shown in Figure 3.1, may be expressed as

$$G_m = \frac{1}{a^4}\frac{9\Delta^2}{2w}\frac{(EI)_1(EI)_2}{(EI)_1+(EI)_2} \tag{1}$$

where $(EI)_i$ are the flexural rigidity of the two beams, a the crack length, w the adhesive's width, and subscript "i" the label for the respective arms.

If one beam of the specimen, i.e. the bottom beam labeled 1 in Figure 3.1, is a composite beam composed of the adherend and adhesive layer, it is only necessary to substitute $(EI)_1$, which are obtained using the transformed-section method, into (1) to get the correct G_m. For this case, the final expression of G_m can be obtained as

$$G_m = \frac{3\Delta^2 BEt^3}{8a^4 w} \frac{B^2E^2t^4 + w^2E_a^2h^4 + 2BwEE_a th(2t^2 + 3th + 2h^2)}{2B^2E^2t^4 + w^2E_a^2h^4 + BwEE_a th(5t^2 + 6th + 4h^2)} \quad (2)$$

where B and w are width of the adherends and adhesive, respectively, t and h are the thickness of adherends and adhesive, respectively, and E and E_a are the corresponding Young's moduli of adherends and adhesive.

3.3.2 Derivation of G_T for an asymmetric wedge test geometry

Consider a specimen composed of two identical substrates that are bonded with a layer of adhesive. In-plane thermal residual stress is present in such a specimen due to a CTE mismatch between the substrates and adhesive, and the temperature difference from the stress free state. If a tensile residual stress is formed within the adhesive layer, and an interfacial debond exists within the specimen, the bimaterial strip will bend toward the other adherend strip. Thus contact forces appear between the two strips. However, if the sign of the residual stress changes, the bending direction of the bimaterial strip is opposite from the previous case, thus the two strips do not contact each other. A schematic diagram of these two cases is shown in Figure 3.2 (b). Therefore, when a wedge is inserted into such a specimen, the total driving force for debond propagation consists of two parts: the wedge induced part, G_m, and residual stress related part, G_T. The expression of the two parts of the driving force can be obtained using the superposition method if the materials are linear elastic and the deflection slope of the beam is small, which is assumed in this dissertation.

The curvature, $1/r$, of a bimaterial strip shown in Figure 3.2 (a) can be expressed as [1]

$$\frac{1}{r} = \frac{6\,\Delta a\;\Delta T\,(1+m)^2}{(h+t)\left(3(1+m)^2 + (1+mn)(m^2 + \frac{1}{mn})\right)} \tag{3}$$

where r is the radius of curvature of the bimaterial strip, Δa is the CTE difference between the adhesive and adherend, ΔT is the temperature change from the stress free temperature, $m=h/t$ is the thickness ratio of two layers, $n=E_a/E$ is the ratio of moduli for the two materials. For the case of a tensile residual stress in the adhesive (Case I), the contact force P_0 is

$$P_0 = \frac{3}{2\,r\,a}\left(\frac{(EI)_1 (EI)_2}{(EI)_1 + (EI)_2}\right) \tag{4}$$

where a is the crack length, $(EI)_i$ is the flexural rigidity of the two strips, and r is thermally-induced radius of curvature of a bimaterial beam composed of the adhesive and adherend. The deformation caused by P_0 can also be obtained by introducing a wedge with a thickness of $\Delta_0=a^2/2r$. The total energy released from the bent bimaterial strip can be obtained as follows

$$U_t = \frac{(EI)_1}{2}\frac{a}{r^2} \tag{5}$$

Part of U_t is stored in the specimen as the strain energy, $U_e=P_0\Delta_0/2$. Therefore, the energy available for driving the debonding is U_t-U_e. The strain energy release rate during the growth of debond can be obtained by differentiating U_t-U_e with respect to debond area $A=a\,w$. Therefore,

$$G_T = \frac{1}{2}\frac{(EI)_1}{wr^2}\left[1-\frac{3}{4}\frac{(EI)_2}{(EI)_1+(EI)_2}\right] \tag{6}$$

Alternatively, when compressive in-plane residual stresses are present in he adhesive (Case II), and the specimen is debonded for a length of a, as shown in Figure 3.2(b). The total strain energy released from the bent strip, U_t, expressed in (5), contributes to the debond growth. Therefore the strain energy release rate during the growth of debond can then be obtained as

$$G_T = \frac{1}{2}\frac{(EI)_1}{wr^2} \tag{7}$$

Interestingly, G_T for the two cases is independent of debond length, a, but the sign of the residual stress determines the value of G_T. G_T is always larger for case II, where all stored energy is released, in contrast to case I where stored energy remains within the arms of the specimen due to the contact force, P_0.

3.4 Discussion

In the following discussion, the adhesive width, w, is assumed equal to the width of the adherends, B, for both cases.

3.4.1 Effect of asymmetry on G_m for an asymmetric wedge test specimen

Figure 3.3 shows the non-dimensional strain energy release rate (SERR), $\Gamma_m = G_m/G_{m0}$, where $G_{m0} = 9\Delta^2(EI)_1/(4a^4)$ is the SERR of a wedge specimen without considering the effects of adhesive and residual stress, as a function of ratios of thickness and Young's moduli for the adhesive and adherends. Γ_m spans between 1 and 2, depending on the values of $m = (h/t)$ and $n = (E_a/E)$. The figure also demonstrates that the

ratio of thickness, m, has a stronger influence on G_m than the ratio of Young's moduli, n, because thickness term in G_T expressions is in cubic order, while Young's modulus is linear. Figure 3.3 (c) illustrates a 3-D figure showing the relationship between G_m and m and n. In a limiting case, in which m and n are much larger than unity, Γ_m reach 2 asymptotically.

3.4.2 Comparison between two cases

Figure 3.4 and 3.5 show the non-dimensional G_T, $\Gamma_T = G_T / [(\Delta T)^2 (\Delta a)^2 Et]$, as a function of thickness ratio m and the ratio of Young's moduli, n. Γ_T shows similar trend for both cases: increases with either m or n initially and reaches different maximum values at small values of n and m. However, with increasing m and n further, Γ_T starts to drop, and finally reaches zero at the limiting conditions in which, the adhesive is either much thicker, or stiffer, than the adherends. Figure 3.6 illustrates the ratio of G_T for the two cases. G_T for Case I is always smaller than for Case II, and the ratio ranges from 0.625 to 0.91 for the common conditions, i.e. h/t and E_a/E is smaller than 1.

3.4.3 Correction of G_m for wedge test geometries

The actual value of G_m is different for the two cases discussed before. For a wedge test specimen with tensile residual stress in the adhesive (Case I), the actual force needed to open a given end opening distance is larger than that required for the case of compressive residual stress in the adhesive (Case II). Therefore, the actual SERR caused by the external load with the same load-point displacement, Δ, G_m is different for these two cases. For Case I:

$$G_m = \frac{1}{a^4} \frac{9\left(\Delta + \frac{a^2}{2r}\right)^2}{2B_2} \frac{(EI)_1 (EI)_2}{(EI)_1 + (EI)_2} \tag{8}$$

and for Case II:

$$G_m = \frac{1}{a^4}\frac{9\left(\Delta - \frac{a^2}{2r}\right)^2}{2B_2}\frac{(EI)_1(EI)_2}{(EI)_1 + (EI)_2} \tag{9}$$

Therefore, (1) underestimates G_m for Case I, but overestimates G_m for Case II, as might be expected.

3.4.4 Comparison with other published solutions

Using a similar method as outlined in this chapter, Nairn [30] investigated the effect of residual stresses on the energy release rate in a DCB specimen with laminated adherends. Nairn studied the case in which crack is located right in the middle of adhesive layer, thus the deformations in the two arms are symmetric. Although Nairn's solution may be applied to the wedge geometry in which the end displacement is fixed, it requires that the total end deflection caused by the external load and residual stress must be positive. For the case of tensile residual stress in adhesive layer (Case I), the end deflection is zero if the fracture is located in the middle of the adhesive layer, but contact forces are produced at the end. Following the analysis in section 3.3, the total energy released is $a(EI)_1/r^2$ and the strain energy in the specimen due to contact is $3a(EI)_1/(4r^2)$. Therefore, the energy available for driving cracking is $a(EI)_1/(4r^2)$. However, for the case of tensile residual stress in adhesive layer (Case II), the total released energy of $a(EI)_1/r^2$ contributes for driving the crack. If the external load is taken to be zero in Nairn's solution, it agrees with the current solution for Case II. The situation for the fixed load and displacement is different for a DCB specimen with residual stress. For load control situation, the contribution of residual stress has two parts, one is due to the net released energy from the debonded arm, and the other is from the work that the external load do due to change of the displacement caused by residual stress, as the crack grows. However, if the end displacement is fixed, as for the wedge test, the external load doesn't do work to the specimen. Therefore, the contribution of the residual stress comes

only from the net released energy as crack grows. The current solutions can be extended to more general cases in which the crack grows parallel with the interface, and is located at an arbitrary distance from the interface. For case I, the contact force between at the end of the specimen is

$$P_0 = \frac{3}{2}\frac{\left(\frac{1}{r_1}+\frac{1}{r_2}\right)}{a\left(\frac{1}{(EI)_1}+\frac{1}{(EI)_2}\right)}$$

where r_1 and r_2 are the radius of curvatures of the two arms respectively. Following the fashion of analysis in section 3.3, the end deflection is

$$\Delta_0 = \frac{a^2}{2}\frac{\frac{1}{r_2}-\frac{(EI)_1}{(EI)_2}\frac{1}{r_1}}{1+\frac{(EI)_1}{(EI)_2}}$$

The stain energy stored in the specimen is

$$U_e = \frac{1}{2}P_0\left[\left(\frac{1}{2}\frac{a^2}{r_1}+\Delta_0\right)+\left(\frac{1}{2}\frac{a^2}{r_2}-\Delta_0\right)\right]$$

The total released energy is

$$U_t = \frac{1}{2}\left[(EI)_1\frac{a^2}{r_1}+(EI)_2\frac{a^2}{r_2}\right]$$

Therefore, the strain energy release rate during the crack growth can be obtained by differentiating U_t-U_e with respect to debond area $A=a\,w$.

For case II, The total released strain energy, U_t, expressed in (5), contributes to the debond growth. Therefore the strain energy release rate during the growth of debond can then be obtained as

$$G_T = \frac{(EI)_1}{2r_1} + \frac{(EI)_2}{2r_2}$$

Adopting the solution of Suo and Hutchinson [23] for thin films, Jiao *et al.* [29] obtained the energy release rate of an asymmetric DCB specimen composed of two adherends with different thermal coefficients. Residual stresses exist in such a specimen with a temperature difference from stress free temperature. Direct comparison of the current solution with Jiao *et al.*'s solution is difficult to make because residual stress is due to thermal mismatch between the adhesive and adherends of a DCB specimen in this chapter, while in Ref [29] residual stresses is caused by different CTE of DCB specimens composed of two arms. Furthermore, Jiao's solution can only be successfully applied to thin film systems, in which residual stress is close to plane strain state. But the solutions in this chapter is for beam geometries in which residual stress is not uniformly distributed in the specimen.

3.5 Conclusions

We demonstrate in this chapter that the energy release rate, G_T, associated with thermal residual stresses in a wedge test geometry is independent of debond length. However, the nature of the residual stress determines the value of G_T. G_T for a specimen with tensile residual stress in the adhesive is always higher than for the case of compression stress in the adhesive, but the difference is smaller than 10% for common

conditions in which adhesive is thinner and has a smaller Young's modulus than adherends. Bending of the debonded bimaterial strip also causes the effective wedge thickness different for the two discussed cases.

3.6 References

1 Stoney, G. G. (1909) The tension of metallic films deposited by electrolysis, *Proceedings of the Royal Society of London*, **A82**, 172-175.

2 Timoshenko, S. (1925) Analysis of bi-metal thermostats, *Journal of Optical Society of America*, **11**, 233-255.

3 Pan, T. Y. and Pao, Y. H. (1990) Deformation in multilayer stacked assemblies, *ASME Journal of Electronics Packaging*, **112**, 30-34.

4 Chen, WT, and Nelson, C. W. (1979) Thermal stress in bonded joints, *IBM J. Res. Div*., **23**, 179-188.

5 Suhir, E. (1986) Stresses in bi-metal thermostats, *ASME Journal of Applied Mechanics*, **53**, 657-660.

6 Suhir, E. (1988) An approximation analysis of stresses in multilayered elastic thin films, *ASME Journal of Applied Mechanics*, **55**, 143-148.

7 Suhir, E. (1989) Interfacial stresses in bimaterial thermostats, *ASME Journal of Applied Mechanics*, **56**, 595-600.

8 Kuo, A. Y. (1989) Thermal stresses at the edge of a bimetallic thermostats, *ASME Journal of Applied Mechanics*, **56**, 585-589.

9 Ru, C. Q. (2002) Interfacial thermal stresses in bimaterial elastic beams: modified beam models revisited, *ASME Journal of Electronics Packaging*, **124**, 141-146.

10 Corcoran, E. M. (1969) Determining stresses in organic coatings using plate beam deflection, *Journal of Paint Technology* **41**, 635-640.

11 Yu, J-H, Guo, S. and Dillard, D. A (2003) Bimaterial curvature measurement for CTE of adhesives: optimization and modeling, *Journal of Adhesion Science and Technology*, **17**, 149-164.

12 Senne, J, Haeberle, D. and Lesko, J. (2000) Interfacial Stresses in Polymer Wearing Surface/FRP Deck Bond Due to Thermal Loading, *Proceeding of 23rd Annual Meeting of the Adhesion Society*, 20-23.

13 Hyer, M. W. (1981) Calculation of the room temperature shapes of unsymmetric laminates, *Journal of Composite Materials*. **15**, 296-310.

14 Masters, C. B. and Salamon, N. J. (1993) Geometrically nonlinear stress-deflection relations for thin film/substrate systems, *International Journal of Engineering Science*, **31**, 915-925.

15 Finot, M. and Suresh. S. (1996) Small and large deformation of thick and thin-film multi-layers: Effects of layer geometry, plasticity and compositional gradients, *Journal of Mechanics and Physics of Solids*, **44**, 683-721.

16 Stoney, G. G. (1909) The tension of metallic films deposited by electrolysis, *Proceedings of the Royal Society of London*, **A82**, 172-175.

17 Dillard, D.A., Park, T., Zhang, H., Chen, B. (1999) Measurement of residual stresses and thermal expansion in adhesive bonds, *Proceedings of the 22nd Annual Meeting of the Adhesion Society*, 336-338.

18 Guo, S., Yu, J.-H., Williams, S., Cao, Y., Dillard, D.A., Roboa, P. (2001) Characterization of coefficient of thermal expansion and coefficient of diluent expansion using a bi-material curvature technique, *Proceedings of the 24th Annual Meeting of the Adhesion Society*, 116-118.

19 Williams, M. L. (1959) The stresses around a fault or crack in dissimilar media, *Bull. Seismol. Soc. America*, **49**, 199-204.

20 England A. H. (1965) A crack between dissimilar media, *ASME Journal of Applied Mechanics*, **32**, 400-402.

21 Erdogan, F. (1965) Stress distribution in bonded materials with cracks, *ASME Journal of Applied Mechanics*, **32**, 403-410.

22 Rice, J. R. (1988) Elastic fracture mechanics concepts for interfacial cracks, *ASME Journal of Applied Mechanics*, **55**, 98-103.

23 Suo, Z. and Hutchinson (1990) Interface crack between two elastic layers, *International Journal of Fracture*, **43**, 1-18.

24 Evans, A. G., Ruhle, M., Dalgleish, B. J. and Charalambides, P. G. (1990) The fracture energy of bimaterial interfaces, *Materials Science and Engineering*, **A126**, 53-64.

25 Daghyani, H. R., Ye, L. and Mai, Y. -W. (1996) Effect of thermal residual stresses on crack path in adhesively bonded system. *Journal Materials Science*, **31**, 2523-2529.

26 Suresh, S., Giannakopoulos, A. E., and Olson, M. (1994) Elasto-plastic analysis of thermal cycling: layered materials with sharp interfaces, *Journal of Mechanics and Physics of Solids*, **42**, 979-1018.

27 Xiao, F., Hui, C. Y., and Kramer, E. J. (1993) Analysis of a mixed mode fracture specimen: Asymmetric Double Cantilever Beam, *Journal of Materials Science*, **28**, 5620-5629.

28 Gaudette, F. G., Giannapoulos, A. E. and Suresh, S. (2001) Interfacial cracks in layered materials subjected to a uniform temperature change, International Journal of Fracture, **110**, 325-349.

29 Jiao, J. Gurumurthy, G. K., Kramer, E. J., Sha Y., Hui, C. Y., and Borgesen (1998) Measurement of interfacial fracture toughness under combined mechanical and thermal stress, *Journal of Electronic Packaging*, **120**, 349-353.

30 Nairn, J. A. (2000) Energy release rate analysis for adhesive and laminate double cantilever beam specimens emphasizing the effect of residual stresses, *International Journal of Adhesion and Adhesives*, **20**, 59-70.

3.7 Figures

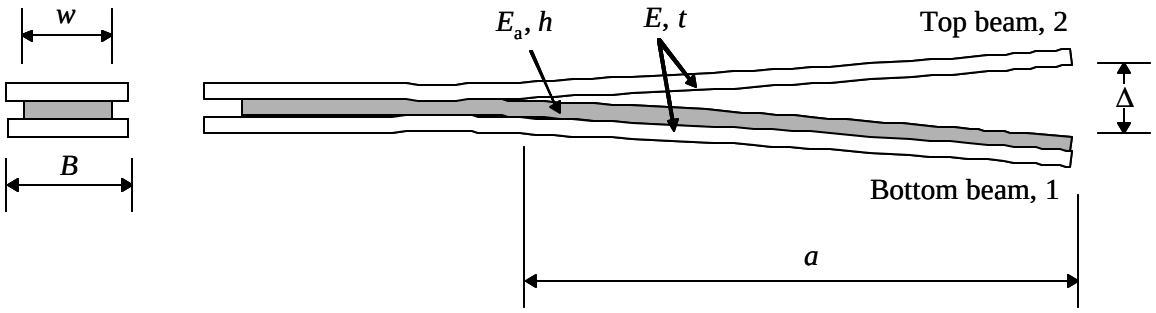

Figure 3.1 Schematic of an Asymmetric DCB specimen in which the adhesive has a different width than the adherends.

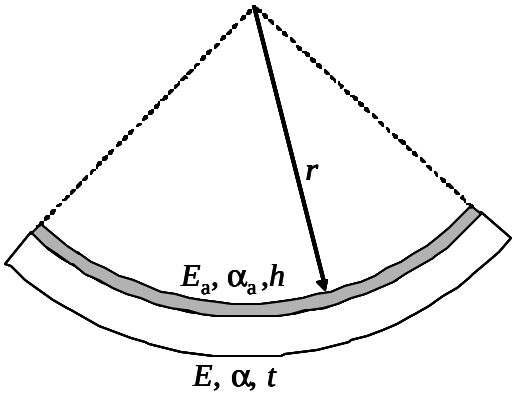

(a)

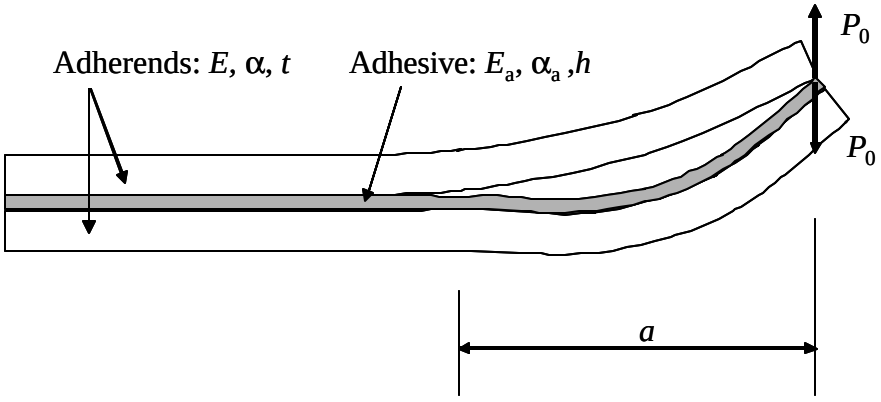

Case I

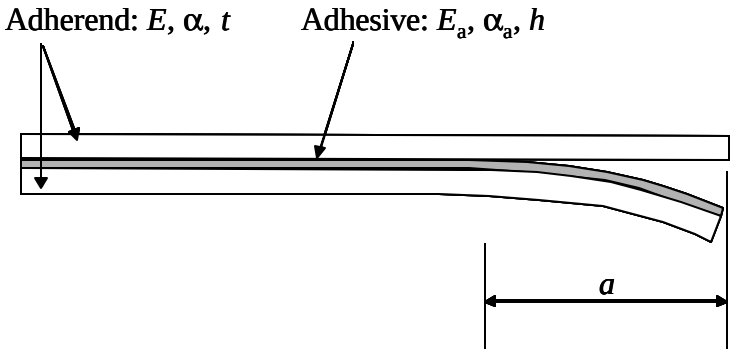

Case II

(b)

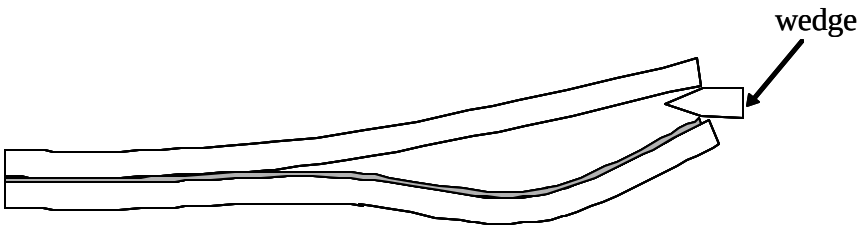

(c)

Figure 3.2 Schematics that show the geometry of a wedge test specimen with the presence of residual stresses. (a) Schematic of a bimaterial strip subject to temperature change. (b) Two cases for a wedge specimen with thermal residual stresses prior to loading. P_0 is the contact force between the two arms of the specimen (c) A wedged specimen having tensile residual stress in the adhesive layer.

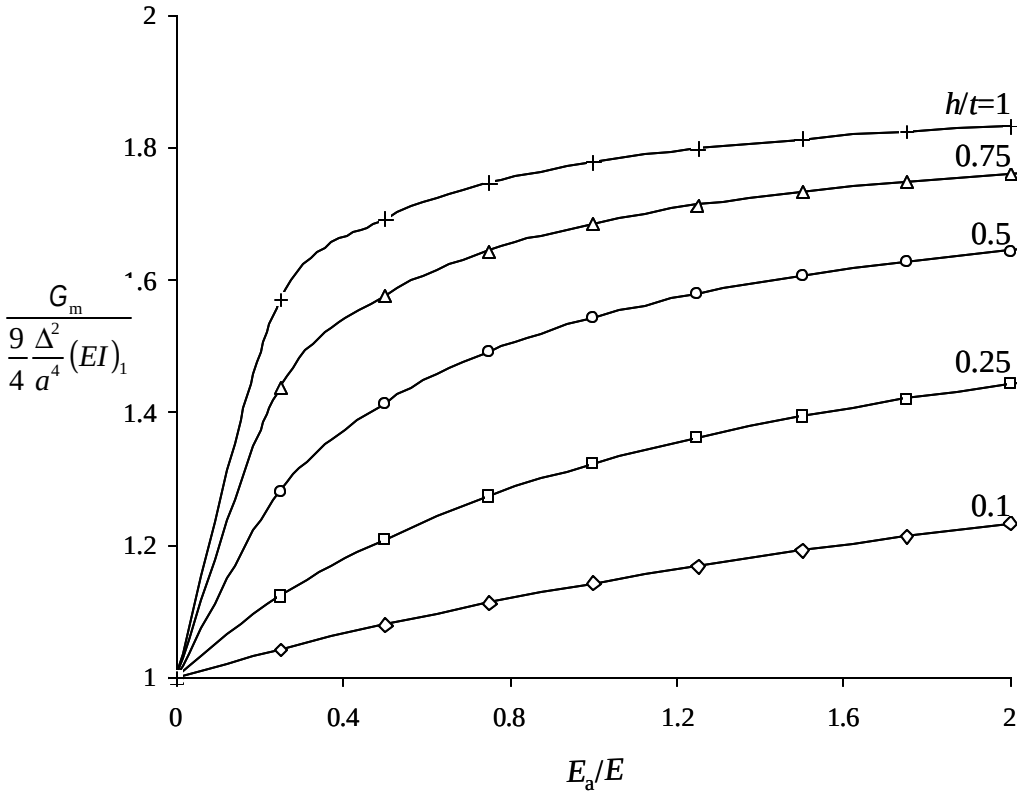
2
1.8
1.6
1.4
1.2
1
0
0.4
0.8
1.2
1.6
2
$\frac{G_m}{\frac{9}{4}\frac{\Delta^2}{a^4}(EI)_1}$
E_a/E
h/t=1
0.75
0.5
0.25
0.1

(a)

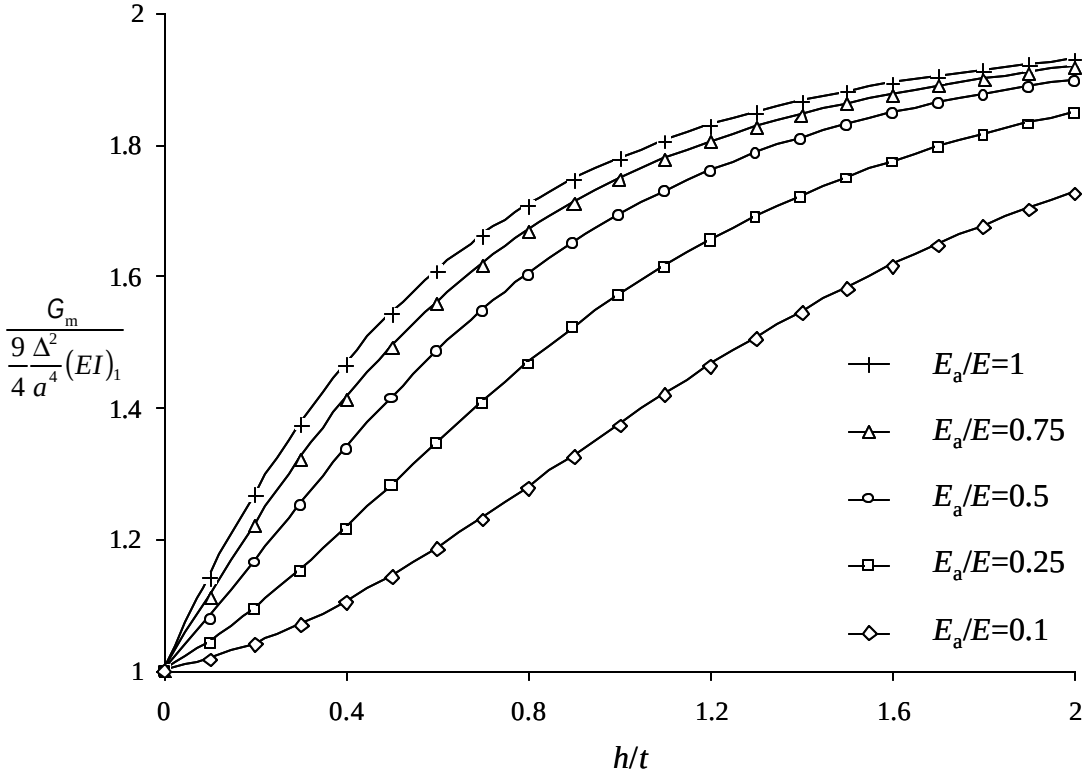
2
1.8
1.6
1.4
1.2
1
0
0.4
0.8
1.2
1.6
2
h/t
$\frac{G_m}{\frac{9}{4}\frac{\Delta^2}{a^4}(EI)_1}$
E_a/E=1
E_a/E=0.75
E_a/E=0.5
E_a/E=0.25
E_a/E=0.1

(b)

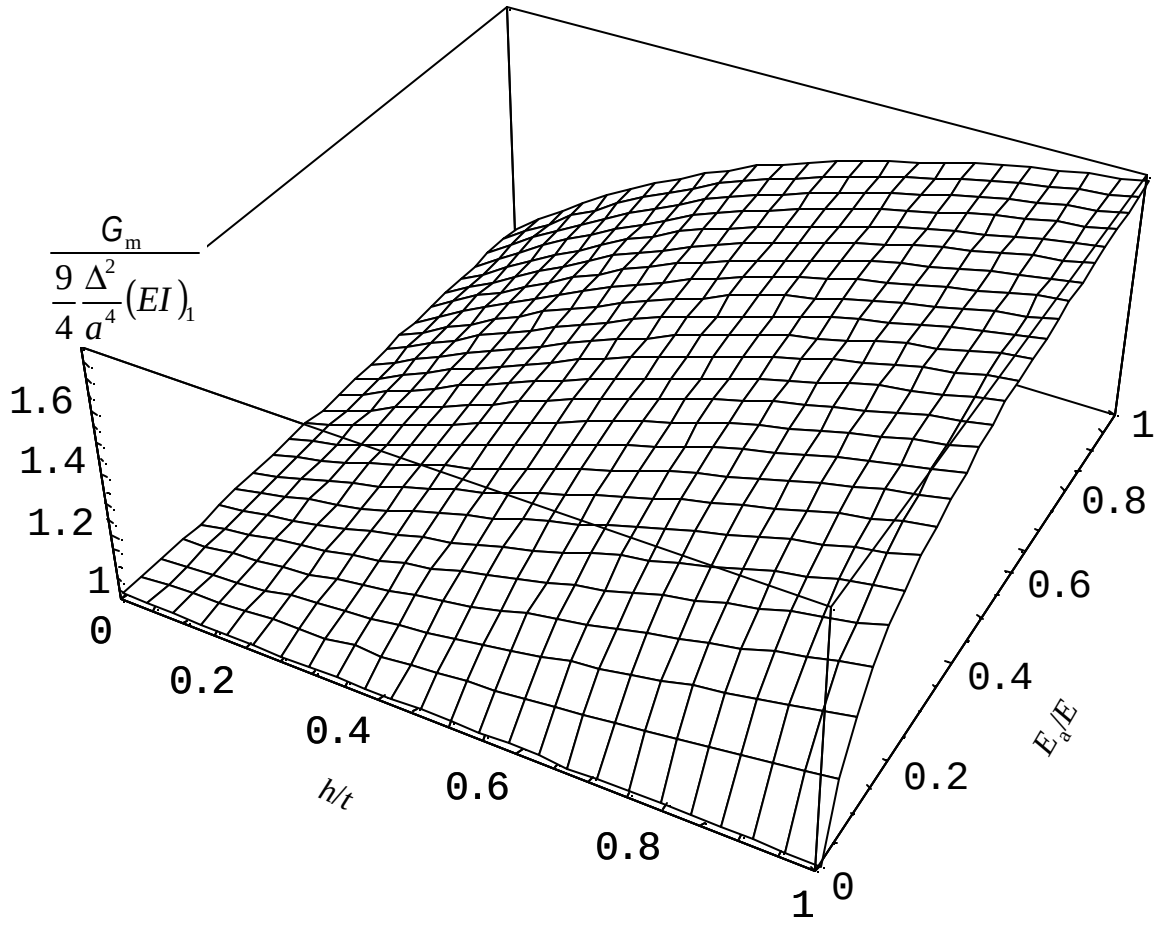

(c)

Figure 3.3 Dependence of non-dimensional strain energy release rate, Γ_m, for an wedge specimen on the thickness ratio and ratio of Young's modulus between the adhesive and adherends. (a) Relationship between Γ_m and the ratio of Young's moduli. (b) Relationship between Γ_m and the thickness ratio. (c) 3D diagram illustrating Γ_m as a function of t_2/t_1 and E_2/E_1.

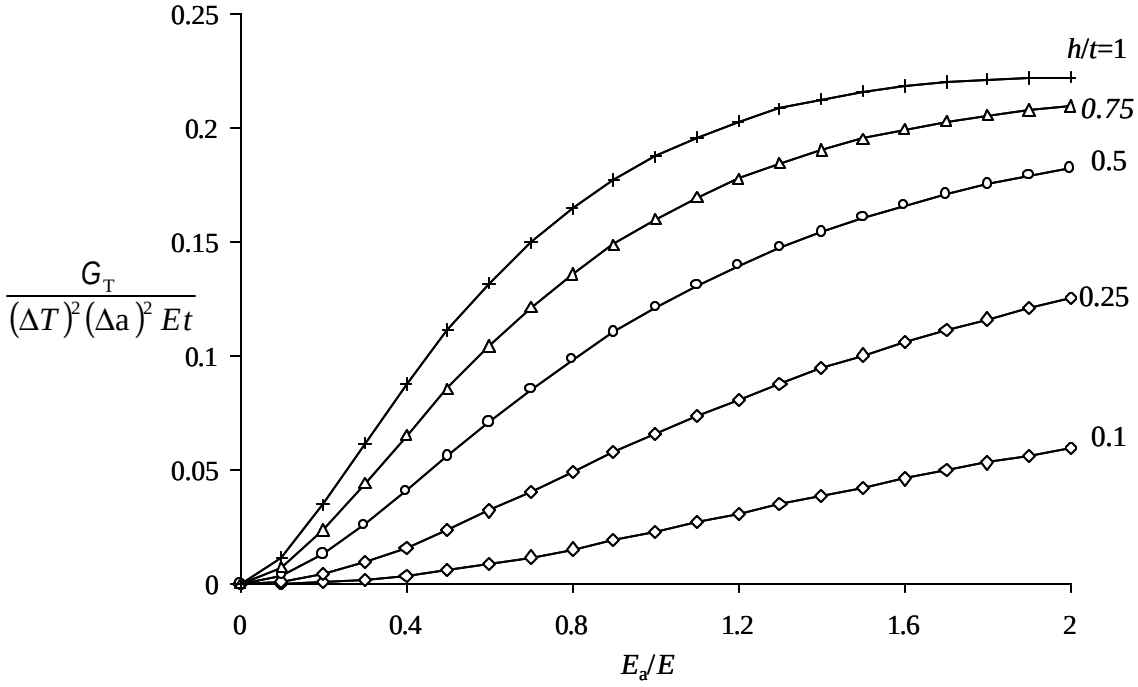
0.25
0.2
0.15
0.1
0.05
0
$\frac{G_T}{(\Delta T)^2(\Delta a)^2 Et}$
h/t=1
0.75
0.5
0.25
0.1
0
0.4
0.8
1.2
1.6
2
E_a/E

(a)

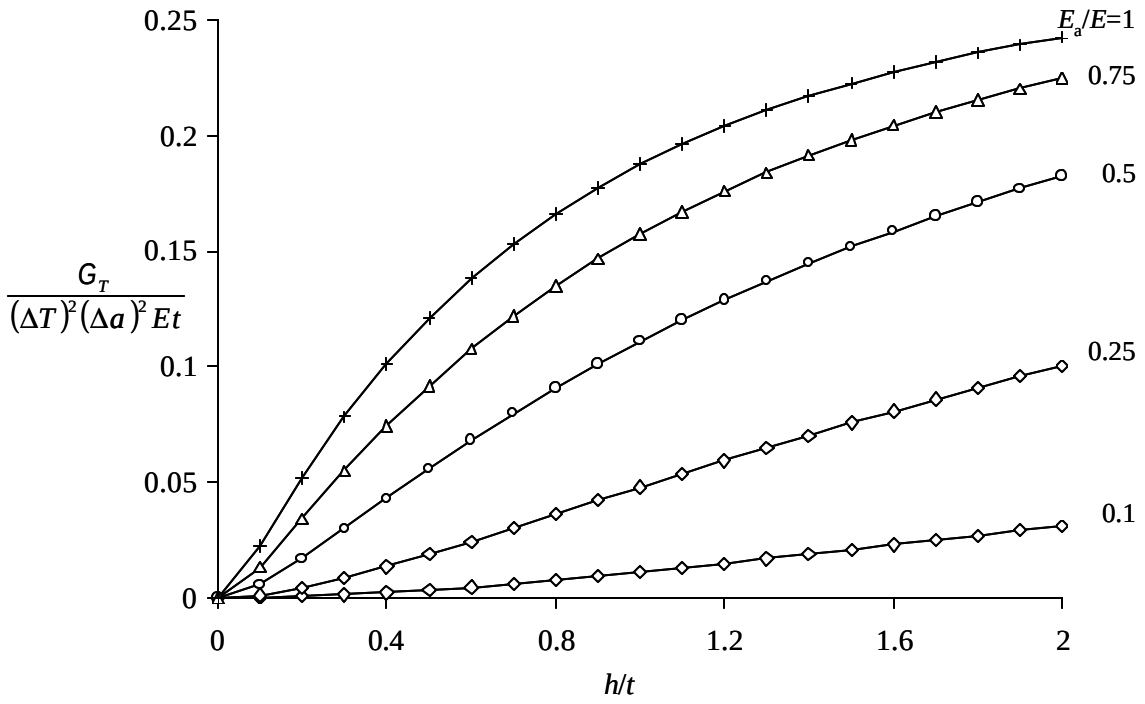
0.25
0.2
0.15
0.1
0.05
0
$\frac{G_T}{(\Delta T)^2(\Delta a)^2 Et}$
0
0.4
0.8
1.2
1.6
2
h/t
E_a/E=1
0.75
0.5
0.25
0.1

(b)

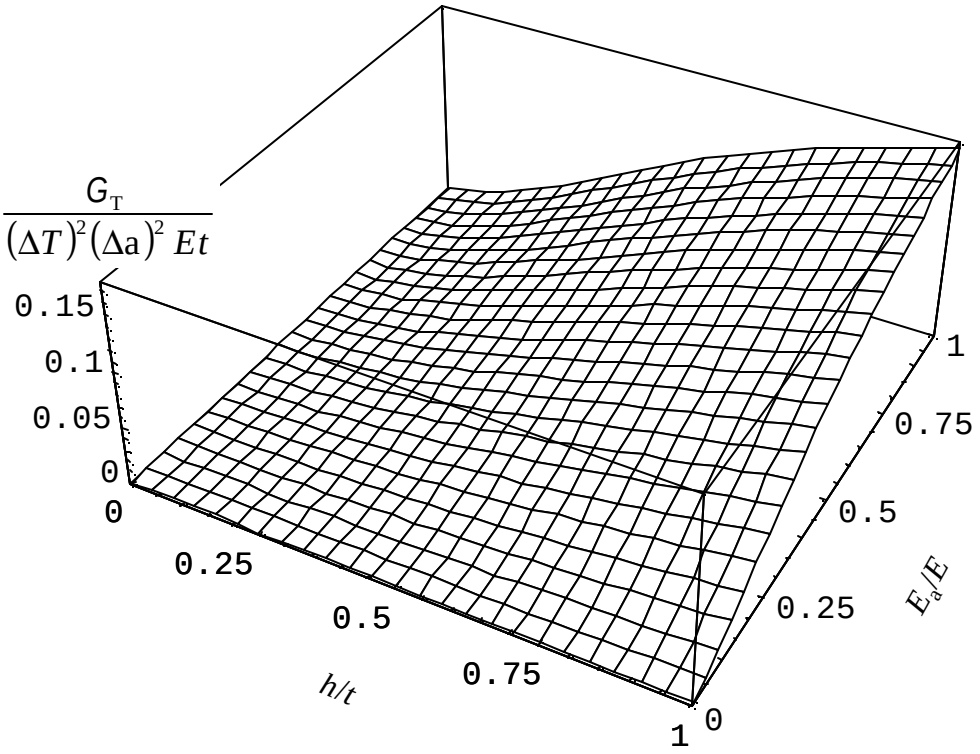

(c)

Figure 3.4 Dependence of non-dimensional thermally induced strain energy release rate, Γ_T, caused by a tensile residual stress in the adhesive for an ADCB specimen on the thickness ratio and ratio of Young's modulus between the adhesive and adherends. (a) Relationship between Γ_m and the ratio of Young's moduli. (b) Relationship between Γ_T and the thickness ratio. (c) 3D diagram illustrating Γ_T as a function of t_2/t_1 and E_2/E_1.

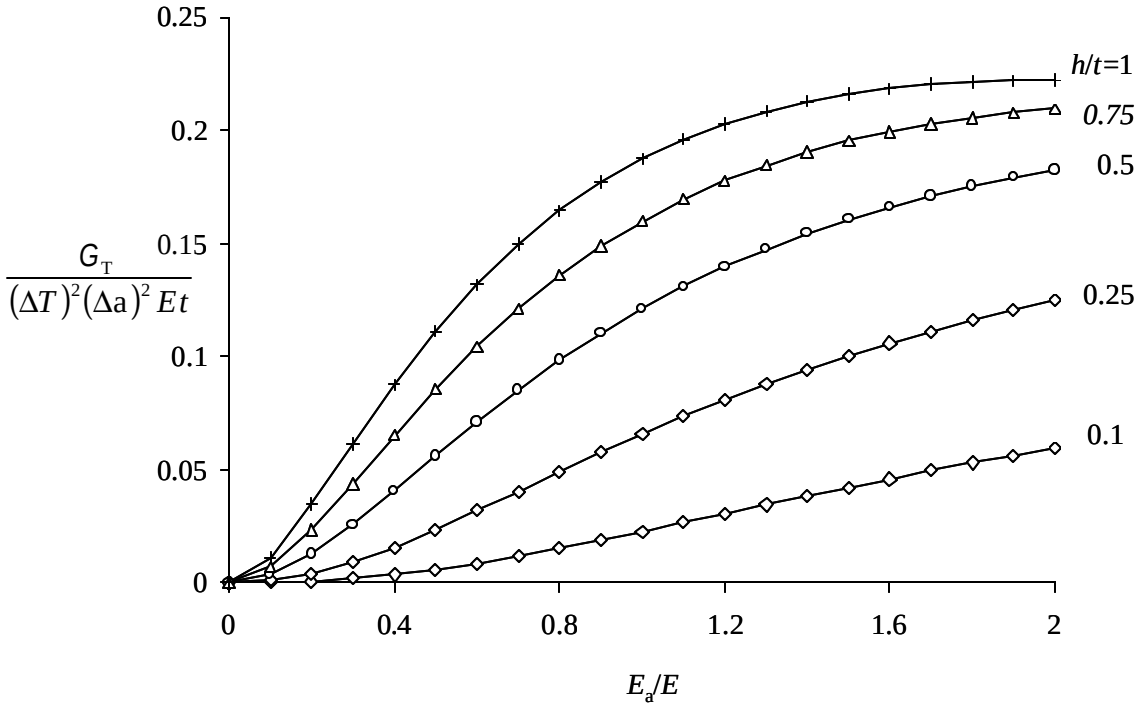
0.25
0.2
0.15
0.1
0.05
0
$\frac{G_T}{(\Delta T)^2(\Delta a)^2 Et}$
0
0.4
0.8
1.2
1.6
2
E_a/E
h/t=1
0.75
0.5
0.25
0.1

(a)

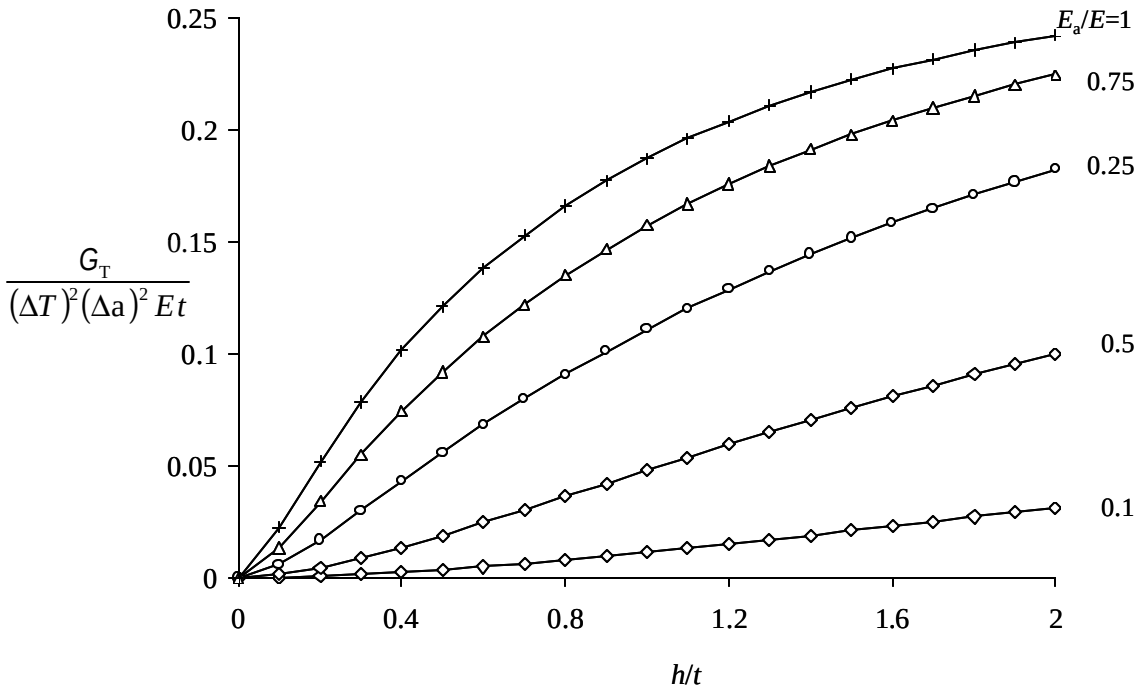
0.25
0.2
0.15
0.1
0.05
0
$\frac{G_T}{(\Delta T)^2(\Delta a)^2 Et}$
0
0.4
0.8
1.2
1.6
2
h/t
E_a/E=1
0.75
0.25
0.5
0.1

(b)

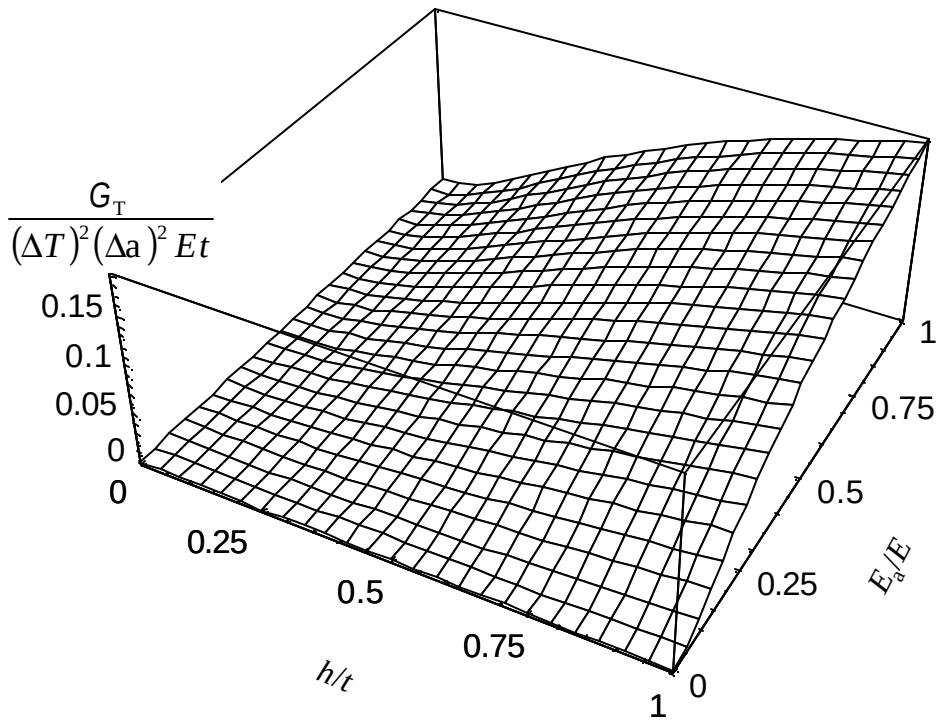

(c)

Figure 3.5 Dependence of non-dimensional strain energy release rate, Γ_T, caused by a compressive residual stress in the adhesive for an ADCB specimen on the thickness ratio and ratio of Young's modulus between the adhesive and adherends. (a) Relationship between Γ_T and the ratio of Young's modulus. (b) Relationship between Γ_T and the thickness ratio. (c) a 3D diagram illustrating Γ_m as a function of t_2/t_1 and E_2/E_1.

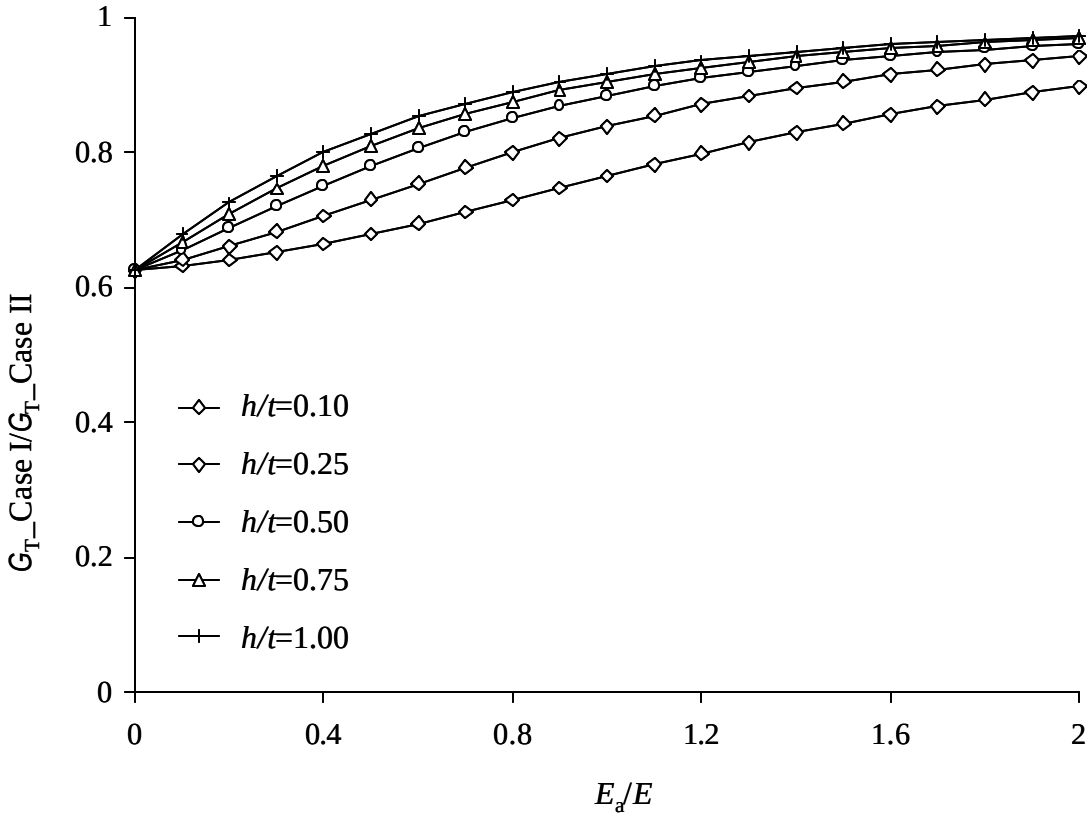
1
0.8
0.6
0.4
0.2
0
0
0.4
0.8
1.2
1.6
2
$G_{T\_Case\ I}/G_{T\_Case\ II}$
E_a/E
h/t=0.10
h/t=0.25
h/t=0.50
h/t=0.75
h/t=1.00

(a)

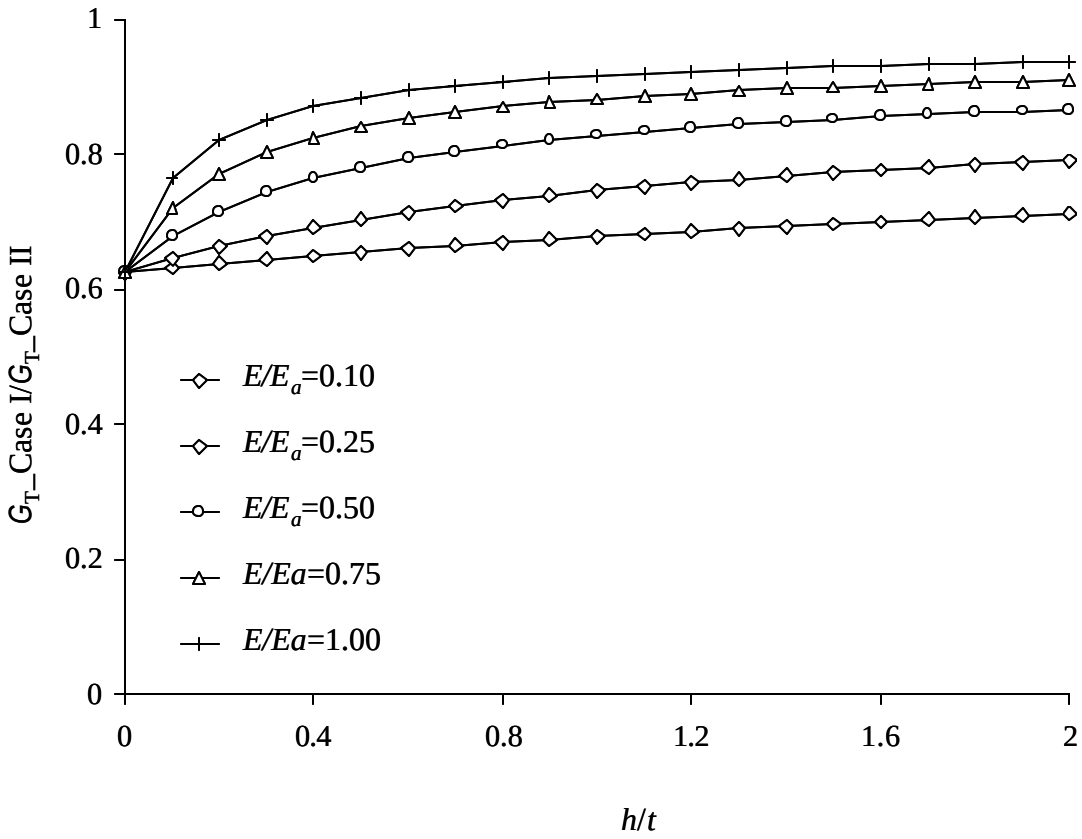
1
0.8
0.6
0.4
0.2
0
0
0.4
0.8
1.2
1.6
2
$G_{T_}$Case I/$G_{T_}$Case II
h/t
E/E_a=0.10
E/E_a=0.25
E/E_a=0.50
E/Ea=0.75
E/Ea=1.00

(b)

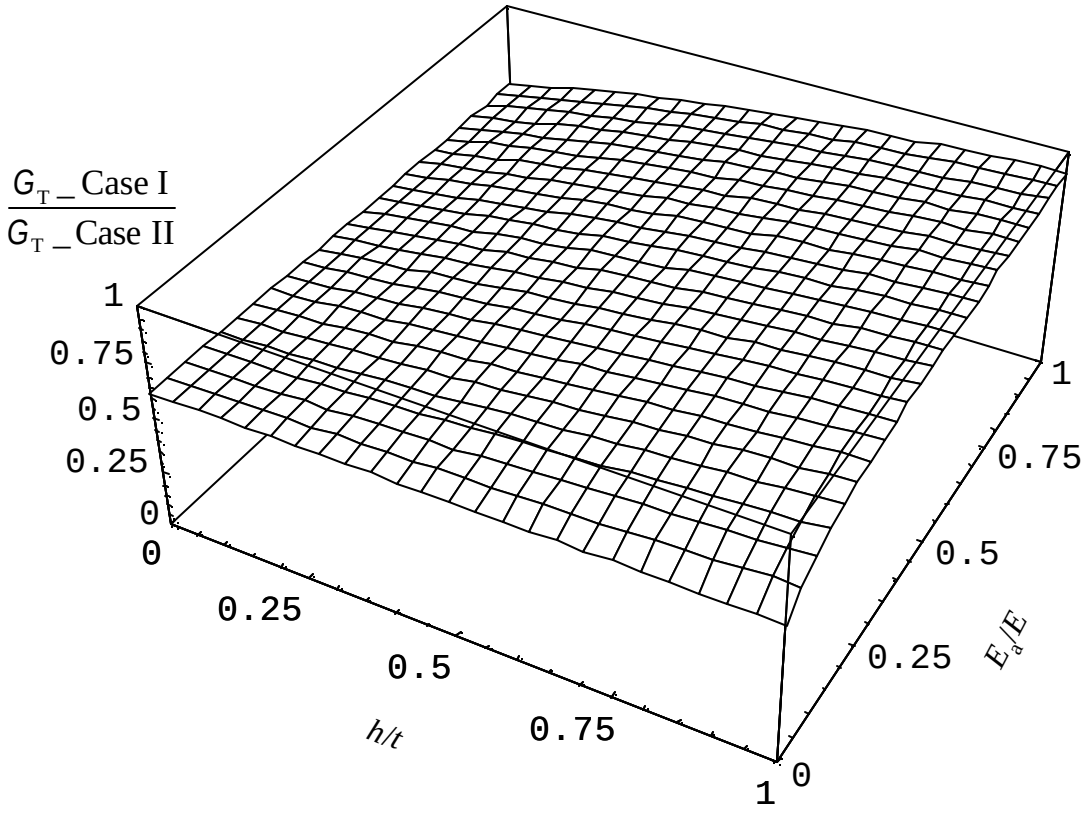

(c)

Figure 3.6 Dependence of the ratio of strain energy release rate, G_T, caused by residual stresses in the adhesive for the two cases. (a) Relationship between the ratio of G_T and the ratio of Young's modulus. (b) Relationship between the ratio of G_T and the thickness ratio. (c) a 3D diagram illustrating the ratio as a function of t_2/t_1 and E_2/E_1.

CHAPTER 4 A BENDING-TO-STRETCHING ANALYSIS OF THE BLISTER TEST IN THE PRESENCE OF RESIDUAL STRESS

(To be submitted to *Journal of Solid Thin Films*)

4.1 Abstract

The adhesion of films and coatings to rigid substrates is often measured using blister geometries, which are loaded either by an applied pressure or a central shaft. The measurement will be affected if there are residual stresses that make a contribution to the energy release rate. This effect is investigated using analytical solutions based on the principle of virtual displacements. A geometrically nonlinear finite element analysis is conducted for comparison. Furthermore, the relationships among strain energy release rate, load, deflection, and fracture radius are discussed in detail in this chapter. Both analytical solutions and numerical results reveal that uniform tensile residual stresses reduce a specimen's deflection if it experiences plate behavior under small loads. However, this effect diminishes when membrane behavior is dominant.

Keywords: blister test, thin film, residual stress, delamination, bending, stretching, adhesion, fracture mechanics, coating.

4.2 Introduction

Blister tests are often used for measuring interfacial fracture energy between a coating film and the substrate [1, 2]. A thin film bonded to a substrate is debonded by applying either a hydrostatic pressure or a point load. The deformation mode in a blister film experiences a transition from bending, when subjected to very small loads, to stretching under high loads. In a bending analysis, the in-plane stresses in the specimen are ignored, while bending rigidity is not considered during stretching analysis. A load-deflection curve is linear for a bending plate, but cubic for a stretching membrane. Besides the conventional circular, unconstrained geometry, some alternative blister configurations have been proposed to measure the adhesion energy between thin films and rigid substrates [3-5]. The following review emphasizes on two standard blister geometries, which will be analyzed in detail later in the thesis.

The most common blister geometry uses pressure to load a specimen. Bennett *et al.* [6] investigated the effect of specimen thickness on the elastic analysis of a pressurized blister, and conducted finite element analysis for verification. The analysis of blisters for thin films gained much attention. Hinkley [7] reported an approximate solution of the pressurized blister without residual stress based on the assumption of a spherical cap for a loaded blister, but gave the wrong solution for the strain energy release rate. Voorthuyzen *et al.* [8] solved numerically the von Karman equation for a pressurized blistering film with residual stress. Gent and Lewandowski [9] later corrected the solution for energy release rate by using a similar method. Allen and Senturia [10] gave equations for both the load-defection relationship and strain energy release rate for both circular and square specimens with constant residual stress. Lin and Senturia [11] and Sizemore *et al.* [12] experimentally verified their elastic model for thin flexible film and applied a perturbation of bending moment for thick films. Small and Nix [13] conducted finite element analysis to compare the accuracy of the analytical solutions based on different deflection profiles. Cotterell and Chen [14] studied the transition from bending to stretching of a blister geometry using Hencky's series solution, and gave a polynomial expression for the strain energy release rate. Using the

assumption of a uniform and isotropic membrane stress, Wan and Lim [15] gave an approximate analytical solution for a pressurized blister without residual stress, and demonstrated the transition from bending to stretching with increasing load. Recently, still based on the assumption of uniform and isotropic in-pane stresses, Wan *et al.* [16] obtained an approximate analytical solution for a clamped circular film in the presence of uniform residual tension. Jensen and Thouless [17] analyzed both tensile and compressive residual stresses in a blister specimen for both small linear displacement limit (pure bending) and large nonlinear membrane-type limit (pure stretching). Sheplak and Dugundji [18] investigated the transition from bending to stretching of a circular plate's deflection with initial stretching using a finite difference technique, and found that tensile residual stress delayed the transition from bending to stretching.

An alternate way of applying load to a blister is by using a rigid shaft to displace the center of the films. Malyshev and Salganik [19] studied the response of a penny-shape debond by treating the adhesive layer as a bending plate. Jensen [20], Jensen and Thouless [17] and Thouless and Jensen [21] reported strain energy release rate for a point loaded blister with and without residual stress. Williams [22] reviewed the strain energy release rate of peel and blister test for flexible films under both applied pressure and an a point load. Wan *et al.* [23-25] measured the adhesion energy between a polymer thin film and rigid substrates using the proposed shaft-loaded blister, and developed an approximate analytical solution for the point loaded blister using the assumption of uniform and isotropic in-plane stress. This solution was extended to the case with residual stresses [16].

Although the blister geometry has been investigated intensively, less effort has been devoted to the transition behavior from bending to stretching. Most work emphasized either of the two limits. Furthermore, the effect of residual stress on this transition has obtained less attention.

In this chapter, we will present comprehensive solutions for a clamped plate in the presence of uniform in-plane tension using the principle of virtual displacements. The plate is subject to either a uniform pressure or a central point load. The solutions are very simple, yet agree with the FEA (finite element analysis) results and other analytical

solutions available in literature. In the second part, the strain energy release rate, G, was derived for a blister debonded from a rigid substrate in the presence of uniform tensile residual stresses. The relationships among G, load, deflection and debond radius are discussed. Furthermore, geometrically nonlinear FEA is conducted to verify the analytical solutions, and the discrepancy between analytical solutions and numerical results is investigated.

4.3 Review of analytical solutions by Wan et al. [16]

This section is based on collaboration of the author and Dr. Kai-Tak Wan. Wan *et al.* [16] obtained approximate analytical solutions for several blister geometries based on the assumption of uniform and isotropic membrane stresses. Nonlinear FEA modeling results to be discussed later in this chapter showed perfect agreement in the bending-dominant region, but a discrepancy in the stretching-controlled region is believed due to the non-uniform and anisotropic membrane stress state under high loading conditions. In this section, the discussions are based on the solutions in ref. [16], but the unnecessary equations will not be listed due to limited space.

For simplicity, the relationship between pressure, p, or central point load, F, and central deflection, w_0, can be expressed in a general form: $F \propto a^2 \, w_0^{\,n}$ for central point loaded blister and $p \propto a^4 \, w_0^{\,n}$ for the pressurized case throughout the whole loading region. Here a is the debond radius, and n can be determined by p or F, and w_0. Depending on the loading level, n ranges from 1 to 3 as the dominant response goes from bending to stretching.

A few useful non-dimensional parameters are defined as:

$$b_m = \left(\frac{N_m a^2}{D} \right)^{1/2}, b_0 = \left(\frac{N_0 a^2}{D} \right)^{1/2}, b = \left(\frac{(N_m + N_0) a^2}{D} \right)^{1/2}, \; r = \frac{p a^4}{2Dh}, j = \frac{F a^2}{2pDh}, W_0 = \frac{w_0}{h}$$

$$c = \frac{G}{pV/A} = \frac{G}{F\, w_0/A}$$

where N_m is the assumed uniform and isotropic membrane stress caused by the external load, N_0 is the residual in-plane tensile membrane stress, $D=Eh^3/[12(1-\nu^2)]$ is the flexural rigidity of plate, E is Young's modulus, h is the plate thickness, ν is Poisson's ratio of the plate, V is the blister volume, $A=\pi a^2$ is the debonded area, and G is the strain energy release rate during debonding.

4.3.1 Pressurized blister

Wan *et al.* [16] showed that $c = (n+2)/(n+1)$ for a pressurized blister without residual stress, thus $1.25<\chi<1.5$. The lower bound corresponds to a pure stretching mode (n=3), while the upper bound to pure bending (n=1). An explicit expression of χ at the limit of bending region can be obtained by ignoring the membrane stress caused by external loading, i.e. $b = b_0$ where b is the total dimensionless membrane stress. Similarly, χ at the membrane limit can also be derived by ignoring b_0, i.e. $b = b_m$. However, in the transition zone, χ cannot be expressed explicitly. The curves of φ and ρ as a function of W_0 for different β_0 at the two limits are shown in Figure 4.2 (a). The influence of b_0 is important only in the bending and bending-to-stretching regimes. b_0 delays the transition from bending to stretching, but all the curves converge together at the stretching limit.

When either the external pressure or the central deflection exceeds a critical threshold, delamination may be driven along the film-substrate interface if the interfacial fracture energy is lower than that of the thin film and substrate materials. The value of the facture energy depends on the strain energy release rate, G, for a fixed pressure p, which is defined to be

$$G = \frac{d}{dA}\left(U_p - U_e\right)\Big|_p \tag{1}$$

where $A = \pi a^2$ is the crack area, the potential energy of the external load

$$U_P = \int p\, dV \tag{2}$$

and the elastic energy stored in the elastic medium

$$U_E = \int_0^a p 2p\, r w_0 dr = \left(\frac{1}{n+1}\right) pV \tag{3}$$

for an elastic film $p \propto a^4 w_0^{\,n}$. Substituting (2) and (3) into (1),

$$G = \left(\frac{n}{n+1}\right) p \frac{dV}{dA} \tag{4}$$

thus

$$c = \left(\frac{n}{n+1}\right)\left(\frac{a}{2V}\right)\frac{dV}{da} \tag{5}$$

In terms of the already defined variables, (5) can also be written as

$$c = \left(\frac{n}{n+1}\right)\left(\frac{b_r}{2V}\right)\frac{dV}{db_r} \tag{6}$$

The blister volume V can be obtained from integration and expressed simply as $V=k_2 \pi a^2 w_0$, where k_2 varies from 1/3 to 0.5 depending on the type of a film's deformation. If ρ can be written as $k_1(w_0/h)^n$, where k_1 is a function of b_m, and can be expressed from the solutions of r and W_0 as reported in ref. [16]. Therefore, V can be rewritten as

$$V = r^{1/n}\left(\frac{1}{k_2}\right)^{1/n} a^2 h$$

$$= \left\{\left[p\frac{1}{2Dh}\left(\frac{D}{N_0}\right)^2\right]^{1/n}\frac{Dh}{N_0}\right\}\left(\frac{V}{a^2 h}\frac{1}{r^{1/n}}\right) b_0^{\frac{2n+4}{n}} \tag{7}$$

The variables in brace are constants independent of a. Substituting (7) into (6), χ can be found as an explicit function of b_m.

4.3.2 Central point-loaded blister

Following the procedure for G derivation in the preceding subsection, the normalized SERR for point loaded case, χ, can be found to be

$$c = \left(\frac{n}{n+1}\right)\left(\frac{a}{2w_0}\right)\frac{dw_0}{da} \tag{8}$$

In terms of the already defined variables, (8) can also be written as

$$c = \left(\frac{n}{n+1}\right)\left(\frac{b_r}{2W_0}\right)\frac{dW_0}{db_r} \qquad (9)?$$

Using the definition of φ and W_0 in ref. [16], W_0 may be re-written as

$$W_0 = \left(\frac{1}{k}\right)^{1/n}\left(\frac{Fa^3}{2pDh}\right)^{1/n}$$

$$= \left[\left(\frac{F}{2pDh}\right)\left(\frac{D}{s_r h}\right)^{1/2}\right]^{1/n}\left[\frac{W_0}{j^{1/n}}\right] b_r^{2/n}? \qquad (10)$$

The variables in the first square bracket are constants independent of *a*. Substituting (10) into (9), χ can be found as an explicit function of b_m by a mathematics software such as MATHEMATICA™, though the lengthy solution is not given here.

4.4 Approximate Analytical solutions based on the principle of virtual displacements

Alternatively, approximate solutions for the problems under consideration can be obtained by using the strain energy method. The following derivations are based on the principle of virtual displacements used by Timoshenko [26].

4.4.1 Pressurized blister

The shape of a loaded blister changes with load level, thus is difficult to be described using a single equation. Assuming that the profile of the deflected circular blister can be represented by the same equation as in the case of small deflections [26], we have

$$w = w_0\left(1-\frac{r^2}{a^2}\right)^2 ? \tag{11}$$

where a is the debond radius and w_0 is the central deflection.

For the radial displacement we assume the expression

$$u = C_0 r + r(a-r)(C_1 + C_2 r + \ldots) \tag{12}$$

where C_0 is determined by the uniform isotropic in-plane residual membrane stress N_0, and C_1 and C_2 depend on the load. The boundary conditions that u must vanish at the center and edge of the film subjected to load are automatically satisfied. u=$C_0 r$ doesn't satisfy the boundary condition at the film's edge and is caused by uniform isotropic residual strain prior to external loading. Substituting (11) and (12) into either one of the following expressions for N_r and N_t [26]:

$$\begin{aligned} N_r &= \frac{Eh}{1-n^2}\left[\frac{du}{dr}+\frac{1}{2}\left(\frac{dw}{dr}\right)^2 + n\frac{u}{r}\right] \\ N_t &= \frac{Eh}{1-n^2}\left[n\frac{du}{dr}+\frac{n}{2}\left(\frac{dw}{dr}\right)^2 + \frac{u}{r}\right] \end{aligned} \tag{13}$$

we have

$$C_0 = \frac{(1-n)N_0}{Eh}$$

From (11) and (12) for the displacements, we calculate the strain components ε_r and ε_t of the middle plane and obtain the strain energy due to stretching of the middle plane by using the expression [26]

$$V_1 = 2p\int_0^a\left(\frac{N_r e_r}{2}+\frac{N_t e_t}{2}\right)rdr = \frac{p\ ?h}{1-n^2}\int_0^a\left(e_r^{\ 2}+2e_r e_t+e_t^{\ 2}\right)rdr \qquad (14)$$

where the strain components ε_r and ε_t can be calculated from [26]

$$\begin{aligned} e_r &= \frac{du}{dr}+\frac{1}{2}\left(\frac{dw}{dr}\right)^2 \\ e_t &= \frac{u}{r} \end{aligned} \qquad (15)$$

We obtain

$$\begin{aligned} V_1 = {} & \frac{32Ehpw_0^{\ 4}}{105a^2(1-n^2)}+\left(\frac{pEha(82n-46)w_0^{\ 2}}{315(1-n^2)}\right)C_1+\left(\frac{4pEha^2(11n+1)w_0^{\ 2}}{315(1-n^2)}\right)C_2 \\ & +\left(\frac{pEha^4}{4(1-n^2)}\right)C_1^{\ 2}+\left(\frac{3pEha^5}{10(1-n^2)}\right)C_1C_2+\left(\frac{2p\,w_0^{\ 2}}{3}\right)N_0 \\ & +\left(\frac{a^2p(1+n)w_0^{\ 2}}{Eh}\right)N_0^{\ 2} \end{aligned} \qquad (16)$$

The constants C_1 and C_2 are now determined from the condition that the total energy of the plate for a position of equilibrium is a minimum. Hence

$$\frac{dV_1}{dC_1} = 0 \qquad \text{and} \qquad \frac{dV_1}{dC_2} = 0$$

We obtain two linear equations for C_1 and C_2 from which we find that

$$C_1 = \frac{(179 - 89\nu)w_0^{\,2}}{126a^3}; \quad C_2 = -\frac{(79 - 13\nu)w_0^{\,2}}{42a^4} \tag{17}$$

We can then explicitly obtain V_1 from (16)

The strain energy of bending can be calculated using the expression [26]

$$V_2 = \frac{D}{2}\int_0^{2\pi}\int_0^a \left[\left(\frac{\partial^2 w}{\partial r^2}\right)^2 + \frac{1}{r^2}\left(\frac{\partial w}{\partial r}\right)^2 + \frac{2\nu}{r}\frac{\partial w}{\partial r}\frac{\partial^2 w}{\partial r^2}\right] r\,dr\,d\theta = \frac{32\pi}{3}\frac{w_0^{\,2}}{a^2} \tag{18}$$

From the principle of virtual displacements, it follows that

$$\frac{d(V_1 + V_2)}{dw_0}dw_0 = 2\pi\int_0^a p\,dw\,r\,dr = 2\pi\, p\,dw_0\int_0^a \left(1 - \frac{r^2}{a^2}\right)^2 r\,dr \tag{19}$$

Substituting expressions for V_1, and V_2 into this equation, we obtain a cubic equation for p:

$$p = \left(\frac{64D}{a^4} + \frac{4}{a^2 h}\sigma_0\right)w_0 + \frac{2(-2791\nu^2 + 4250\nu + 7050)}{6615(1-\nu^2)}\frac{Eh}{a^4}w_0^{\,3} \tag{20}$$

For N_0=0, this result agrees with Timoshenko's solution [26]. Figure 4.2(a) shows the normalized constitutive relationship with different residual stress β_0, together with the solutions by Wan *et al.* [16] and FEA results, which will be discussed in Section 4.6

4.4.2 Central point loaded blister

For a central point loaded circular blister, we assume the deflection profile as [26]

$$w = w_0\left[1-\left(\frac{r}{a}\right)^2 - 2\left(\frac{r}{a}\right)^2 Log\left[\frac{r}{a}\right]\right] \tag{21}$$

and the same radial displacement expression as for the pressurized case in (12). Following the same procedure used for the pressurized condition, we obtain a cubic equation for the point load F

$$F = \left(\frac{16pD}{a^2} + p\,hs_0\right)w_0 + \frac{(704679 + 291054n - 357049n^2)}{1215000(1-n^2)}\frac{pEh}{a^2}w_0^{\,3} \tag{22}$$

Figure 4.2(b) shows the normalized constitutive relationship for a point-loaded plate together with Wan's solution [16] and FEA results. The curves illustrate a similar shape as pressurized plate. For both point loaded and uniformly loaded plate, we find that the normalized residual stress parameter β_0 only affects the linear region of the response of the plate. The disagreement of (22) and the FEA results is owing to the assumption of deflection profile defined in (21), and will be discussed in detail in section 4.7.

4.4.3 Modification of the solution to central-point loaded blister

The disagreement between the FEA results and (22) becomes more significant with increasing residual stress s_0 (or b_0), as shown in Figure 4.2(b). The analysis of the deflection profiles in Section 4.7 suggests that (21) cannot reflect the features of the deflection either in the stretching region without residual stress, or with the existence of σ_0. However, the j-W_0 relationship may be expressed as a combination of linear terms, which reflect the bending response and influence of residual stress, and a cubic term which results from the stretching deformation. In (22), the coefficients of the linear term with σ_0 and cubic term are not accurate due to the inaccurate profile assumption of (21). However, more accurate coefficients may be obtained using the curve-fitting technique based on the FEA results, which are thought to be closer to the real solution than any of the two analytical approaches reported in this study. Therefore, the non-dimensional j-W_0 relationship can be expressed in the following general form

$$j = (8 + K_1 b_0^{\,n}) W_0 + K_2 W_0^{\,3} \tag{23}$$

where n, K_1 and K_2 are the parameters to be determined from nonlinear curve-fitting of the FEA results and should be functions of Poisson's ratio, ν. For ν=0.3, n=1.85, K_1=0.5, and K_2=1.721. Figure 4.3 shows the modified solution together with the FEA results and Wan's solution. The following fracture analysis for the central-point loaded case is based on this modified solution.

4.5 Fracture analysis

For delamination of a circular blister from a rigid substrate subjected to either pressure, or a central point load, the applied strain energy release rate, G, can be derived by calculating the strain energy or complimentary energy using the solutions from the preceding subsection, then differentiating with respect to debond area.

4.5.1 Pressurized blister

When a blister is delaminated axisymmetrically from a rigid substrate at a fixed blister volume *V*, the stain energy release rate can be obtained using

$$G = -\left.\frac{dU_e}{dA}\right|_V$$

where U_e is the strain energy which can be expressed as $\int p\,dV$, and $A=\pi a^2$ is the debond area. Alternatively, under fixed pressure, *p*, conditions, *G* can also be derived by

$$G = \left.\frac{dU_c}{dA}\right|_p$$

where $U_c = \int V\,dp$ is the complimentary energy in the blister film [30]. If the p-w_0 relationship can be expressed in a polynomial form, the above two definitions yield identical *G*, and same conclusion can be drawn for the central-point loaded case. For the other forms of p-w_0 equations, *G* is normally obtained using the first definition.

Substituting the solution obtained in the proceeding section into either of the above expressions for *G*, we obtain:

$$G = \left(\frac{8Eh^3}{3a^4(1-n^2)} + \frac{4N_0}{3a^2}\right) w_0^{\,2} + \frac{(7505 - 4250n + 2791n^2)}{7938(1-n^2)} \frac{Eh}{a^4} w_0^{\,4} \qquad (24)$$

4.5.2 Central point-loaded blister

In a similar fashion, the strain energy release rate for the central point-loaded case can be calculated by either of the following two definitions:

$$G = \left.\frac{dU_e}{dA}\right|_{w_0}$$

for fixed displacement, w_0, or

$$G = \left.\frac{dU_c}{dA}\right|_{F}$$

for fixed load, F.

Substituting the expression for F into either of the two above equations, G can be found to be

$$G = \left[8 + 0.0375\left(\frac{N_0 a}{D}\right)^{0.925}\right]\frac{D}{a^4}{w_0}^2 + 0.8605\frac{D}{a^4 h^2}w_0^4 \qquad (25)$$

4.6 Finite element analysis

In order to verify the preceding analytical solutions, a geometrically nonlinear finite element analysis (FEA) was conducted using the commercial general FEA package ABAQUS®. Axisymmetric quadratic shell elements were adopted to model the film under different loading configurations. Biased meshes were constructed at both the inner

and outer boundaries of the membrane, using a length ratio between adjacent elements of 1.25. A blister with a radius of 25mm and thickness of 0.1mm was modeled in the numerical simulation. A Young's modulus of 4 GPa and Poisson's ratio of 0.35 was used to mimic a typical filled polymeric material. Equal-biaxial prescribed tensile stresses were applied to the model to simulate the uniform residual stresses. Figure 4.4 shows the meshes for the two loading configurations. Results from the finite element analysis have been shown in each of the graphs presented above to allow comparisons with the analytical solutions.

The strain energy release rate (SERR) during a blister's delamination from a rigid substrate is determined using the commonly adopted virtual crack closure technique (VCCT) [31, 32]. This method was based on Irwin's theory on fracture [33]: if a crack extends by a small amount Δc, the energy released in the process is equal to that required to close the crack to its original length. Applying VCCT to axisymmetric shell cases, the SERR components can be expressed as:

$$G = \frac{1}{2\Delta c}(Z_1 w_2 + R_1 u_2 + M_1 q_2) \tag{26}$$

where *R, Z* and *M* are the reaction forces and moment at the blister edge, *u* and *w* are the nodal displacement components along *r* and *z* directions respectively, and *q* is the rotation angle. The subscripts denote the corresponding nodes in Figure 4.5.

4.7 Discussions

4.7.1 Relationship between strain energy release rate and central deflection

Figure 4.6 shows the curves indicating the relationship between non-dimensional strain energy release rate, χ,?and non-dimensional central deflection $W_0=w_0/h$. The normalized residual stress β_0 varies from zero to 50. Generally, β_0 tends to reduce the

value of χ when W_0 is small, corresponding to bending response, but all the curves for different β_0 continuously converge to the same χ value ($\chi_{stretching}$=1.25 for a pressurized blister, and $\chi_{stretching}$ =0.25 for the point loaded case) when W_0 is significantly large so that stretching in the plate is dominant. When β_0 is sufficiently large (>50) χ reaches constant asymptotic values for two loading cases (0 for pressurized case and 1 for point loaded situation respectively) independent of β_0 even at low W_0 limits. The degree of the agreement between the two analytical solutions and FEA results is different. Wan's solution shows perfect agreement in the bending limit, while the solution based on the energy methods agrees well with the FEA data at the stretching limit. The discrepancy between FEA and the two approximate solutions are due to their respective assumptions, which affect the accuracy of the solutions.

In the following discussions, the relationships between load, central deflection, and blister radius during debonding are discussed. Therefore, the following non-dimensional parameters need to be defined to facilitate the discussion:

Non-dimensional fracture toughness: $\Gamma = \dfrac{G}{D/h^2}$

Non-dimensional pressure: $\Pi = \dfrac{p}{D/h}$

Non-dimensional point load: $\Phi = \dfrac{F}{D/h^3}$

Non-dimensional blister radius: $\alpha = a/h$

Non-dimensional central deflection: $W_0 = w_0/h$

Γ is around the range of 0.01 if using the material properties and specimen dimensions for FEA analysis and taking G=100 J/m^2 to represent a typical interfacial

fracture toughness between polymeric thin film and silicon substrate [34]. Therefore, Γ=0.01 is chosen in the following discussions to simulate the typical polymeric thin film system. Because the expressions of Wan's solution based on the uniform and isotropic membrane stress are so complicated that some mathematical operations seems too difficult for MATHEMATICA^{TM}, the mathematical package used in this study, only the energy method based solution and FEA are discussed in the following.

4.7.2 Relationship between critical central deflection and debond radius

Figure 4.7 shows the central deflection W_0 as a function of a at constant Γ=0.01. β_0 ranges from 0 to 50. This figure physically illustrates how central deflections changes with debond radius during blister experiments. Two distinct regions are observed in this figure. In the bending dominant region $w_0 \propto a^2$, while $w_0 \propto a$ in the stretching domain. For the pressurized case, FEA results fit analytical solutions well, and β_0 delays the transition from bending to stretching. However, for the central point loaded case, the energy method based analytical solution illustrates the same trend as the FEA results, but in the bending domain they don't agree in the presence of β_0. The inaccurate profile assumption of the loaded blister is believed to cause this discrepancy, and should be improved by using a better mathematical profile expression.

4.7.3 Relationship between load and debond radius

Another blister test procedure requires debonding load and fracture radius for fracture energy measurement. Φ and Π as functions of α are illustrated in Figure 4.8 for Γ=0.01. For a blister with subjected to pressure, $\Pi \propto a^{-2}$ when the specimen responds like a bending plate, while $\Pi \propto a^{-1}$ when the specimen's deformation is mainly stretching like a membrane. The transition between these two regions is a function of β_0, and the tensile residual stress delays the transition from bending to stretching.

For the central point loaded blister, Φ initially is a constant independent of α, but increases with increasing β_0 during debonding when load is small. However, Φ gradually becomes linear with α when the film's response is like a flexible membrane, and all the

curves with different β_0 merge together when α is very high. Analytical solutions predict lower Φ in low α region due to poor deflection assumption in (21), but agrees fairly well with FEA results.

4.7.4 Relationship between debonding load and displacement

The compliance of a specimen during fracture tests is often used for G measurement, thus the understanding of how load changes with displacement is important. Figure 4.9 illustrates non-dimensional pressure or point load as functions of central deflection with the presence of different β_0. For the pressurized case, no difference is observed between the relationship between Π and W_0 throughout the bending and stretching regions, and can be approximately expressed as $\Pi \propto W_0^{-1}$. FEA simulations verify this prediction.

For the central point loaded blister, however, the curves show very similar trend to those for Φ versus α, as shown in Figure 4.8. Φ is a constant in the bending region, but is linear with W_0 when membrane behavior is much more significant than plate bending. β_0 increases the constant value in the bending region. FEA results show similar trends, but yield lower constant load values in the bending domain than the analytical solutions.

4.7.5 Difference between FEA results and analytical solutions

As reported in the preceding subsections, significant differences are observed between analytical solutions and numerical results in some situations. This can be attributed to the blister profile assumed in the analytical solutions. Figure 4.10 shows the deflection profile for the two loading configurations. The assumed deflection in (11) and (21) are based on the small deflection solutions, in which there is no stretching deformation. However, when the film deforms into stretching region, or residual stress is present, this assumption is not accurate anymore. Figure 4.11 (a) and (b) show that (11) is only accurate for small loading without residual stress. The profile is almost

independent of loading with the presence of high residual stress (β_0=25), and is close to the deflection profile under high loading without residual stress.

For a central point loaded blister film, Figure 4.10 (c) and (d) shows that (21) only is accurate when a stress-free plate is subject to small loadings. However, the actual deflection deviates from the presumed one either when subjected to high loading, or in the presence of residual stress.

Although the disagreement between FEA results and analytical solutions can be qualitatively explained by the difference between the deflection profiles presumed in (11) and (21) and that which FEA predicts, load-deflection relationships and SERR have different degrees of dependence on this discrepancy. For load-deflection relationships, as shown in Figure 4.2, the energy method based solution agrees with the FEA almost perfectly, while the difference becomes more significant in the central point loaded case as illustrated in (b) of this figure. However, for strain energy release rate, analytical solutions for both loading configurations agree with FEA results without residual stress, but the disagreement becomes more evident with increasing β_0. Analytical solutions give fair predictions for the relationship between load, central deflection and fracture radius for the pressurized blister, but show obvious variation for the central point loaded case. Therefore, a more accurate profile assumption should be used in order to obtain better solutions for central point loaded blister case.

4.7.6 Comparison with other solutions

Pressurized blisters have obtained many researchers' attention for a long time, and many solutions were reported, some of which are explicit polynomial expressions. Therefore, it is instructive to compare those solutions with what was reported in this chapter. Table 4.1 lists these solutions as comparison, and Figure 4.11 shows r-W_0 relationships from different solutions and FEA results. Because residual stress only appears in the linear terms, only the stretching behavior is captured by those solutions. For the cases with residual stresses, however, they show encouraging agreement with FEA models. The solution proposed in this chapter can capture the response from

bending to stretching, thus is more complete. As to the G calculation, significantly different shapes were observed for different solutions, although they agree with each other in the stretching limit. William's and Lin's solutions predict different values at the bending limit, and both of them are different from FEA results. Both solutions indicate that uniform tensile residual stresses delay the transition from bending to stretching. But, FEA results reveal that residual stress also changes the behavior in the bending-controlled domain, thus, attention should be given when such solutions are applied to practice.

4.8 Conclusions

The deformation and delamination behaviors of a blister under both pressure and central point load cases were investigated over a wide range of transverse loadings and initial in-plane uniform tensile stresses. If the blister is really thin or flexible, the residual stress can be ignored for deflection and G calculation using either measured load or displacement data. However, when bending or bending-to-stretching transition behavior is significant during the debonding process, the residual stress must be taken into account, and the correct equations should be adopted to measure the adhesion energy. The proposed solutions for the pressurized blister geometry fit well with FEA results, thus can be applied in practice safely. Although the solutions to the central point loaded case doesn't demonstrate promising agreement with numerical predictions due to poor profile assumption, qualitative trends can still be obtained using them. The results reported in this chapter will be useful to the engineers intending to measure residual stresses of thin films, and also for characterizing the adhesion energy between a thin film and rigid substrate using one of the two geometries.

4.9 References

1 Dannenberg, H. (1961) Measurement of adhesion by a blister method, *Journal of Applied Polymers Science*, **5**, 125-134.

2 Williams, M. L. (1969) The continuum interpretation for fracture and adhesion, *Journal of Applied Polymers Science*, **13**, 29-40.

3 Chang, Y. S., Lai, Y. H. and Dillard, D. A. and (1989) The constrained blister–A nearly constant strain energy release rate test for adhesives, *Journal of Adhesion*, **27**, 197-211.

4 Dillard, D. A. and Bao, Y. (1991) The peninsula blister test: A high and constant strain energy release rate fracture specimen fro adhesives, *Journal of Adhesion*, **33**, 253-271.

5 Wan, K.-T. (2002) Adherence of a Axisymmetric flat punch onto a clamped plate-Transition from a rigid plate to a flexible membrane, *ASME Journal of Applied Mechanics*, **69**, 104-109.

6 Bennett, S. J., Devries, K. L. and Williams, M. L. (1974) Adhsive fracture mechanics, *International Journal of Fracture*, **10**, 33-43.

7 Hinkley, J. A. (1983) A blister test for adhesion of polymer films to SiO_2, *Journal of Adhesion*, **16**, 115-126.

8 Voorthuyzen J.A., Bergveld, P. (1984) The influence of tensile forces on the deflection of circular diaphragms in pressure sensors. *Sensors and Actuators*, **6**, 201-213.

9 Gent, A. N. and Lewandowski, L. H. (1987) Blow-off pressure for adhering layers. *Journal of Applied Polymer Science*, **33**, 1567-1577.

10 Allen, M.G and Senturia, S.D. (1988) Analysis of critical debonding pressures of stressed thin films in the blister test, *Journal of Adhesion*, **25**, 303-315.

11 Lin P., Senturia S.D. (1990) The in-situ measurement of biaxial modulus and residual stress of multi-layer polymeric thin films. *Materials Research Society Symposium Proceedings*, **188**, 41-46.

12 Sizemore J., Hohlfelder, R.J., Vlassak J.J., Nix W.D. (1995) Measuring the adhesion of diamond thin films to substrates using the blister test. *Materials Research Society Symposium Proceedings*, **383**, 197-207.

13 Small, M. K. and Nix, W. D. (1992) Analysis of the accuracy of the bulge test in determing the mechanical properties of the thin film, *Journal of Materials Research*, **7**, 1553-1563.

14 Cotterell B., Chen, Z. (1997) The blister test – Transition from plate to membrane behavior for an elastic material. *International Journal of Fracture*, **86**, 191-198.

15 Wan, K-T., Lim, S.C. (1998) The bending to stretching transition of a pressurized blister. *International Journal of Fracture*, **92**, L43-L47

16 Wan, K-T, Guo, S. and Dillard, D. A. (2003) A theoretical and numerical study of a thin clamped circular film under an external load in the presence of residual stress. *Journal of Solid Thin films*, **425**, 150-162.

17 Jensen, H.M., Thouless, M. D. (1993). Effects of residual stresses in the blister test. *International Journal of Solids and Structures*, **30**, 779-795.

18 Sheplak, M. and Dugundji, J. (1998) Large deflections of clamped circular plates under initial tension and transitions to membrane behavior. *ASME Journal of Applied Mechanics*, **65**, 107-115.

19 Malyshev, B. M., Salganik, R. L. (1965) The strength of adhesive joints using the theory of cracks. *International Journal of Fracture*, **1**, 114-128.

20 Jensen, H. M. (1991). The blister test for interfacial toughness measurement. *Engineering Fracture Mechanics*, **40**, 475-486.

21 Thouless, M. D. and Jensen, H. M. (1994) The effect of residual stresses on adhesion measurement. J*ournal of Adhesion Science and Technology*, **8**, 579-586.

22 Williams, J.G. (1997) Energy release rates for the peeling of flexible membranes and the analysis of blister tests. *International Journal of Fracture*, **87**, 265-288.

23 Wan, K-T., Mai, Y.W. (1995) Fracture mechanics of a shaft-loaded blister of thin flexible membrane on rigid substrate. *International Journal of Fracture*, **74**, 181-197.

24 Wan, K-T. and Liao, K. (1999) Measuring mechanical properties of thin flexible films by a shaft-loaded blister test. *Thin Solid Films*, **352**, 167-172.

25 Wan, K-T. (1999). Fracture mechanics of a shaft-loaded blister test - Transition from a bending plate to a stretching membrane. *Journal of Adhesion*, **70**, 209-219.

26 Timoshenko, S. P., Woinowsky-Krieger, S. (1959) *Theory of Plates and Shells*. 2nd Ed. McGraw-Hill, New York.

27 Williams, J.G. (1997) Energy release rates for the peeling of flexible membranes and the analysis of blister tests. *International Journal of Fracture*, **87**, 265-288.

28 Williams, M.L. (1969) The continuum interpretation for fracture and adhesion. *Journal of Applied Polymer Science*, **13**, 29-40.

29 Wan, K-T., Horn, R. G., Courmont S., Lawn, B. R. (1993) Pressurised internal lenticular cracks at healed mica interfaces. *Journal of Materials Research*, **8**, 1128-1136.

30 Williams, J. G. (1984) *Fracture Mechanics of Polymers*, John Wiley & Sons Ltd., London.

31 Rybicki, E. F. and Kanninen, M. F. (1977) A finite element calculation of stress intensity factors by a modified crack closure integral. *Engineering Fracture Mechanics*, **9**, 931-938.

32 Raju, I. S. (1987) Calculation of strain-energy release rate with higher order and singular finite elements, *Engineering Fracture Mechanics*, **28**, 251-74.

33 Irwin, G. R. (1958) Fracture, *Handbuch der Physik*. **6**, 551.

34 Hohlfel, R. J., Luo, H., Vlasska, J. J., Chidsey, C. E. D., and Nix, W. D. (1997) Measuring interfacial fracture toughness with the blister test, *Material Research Symposium Proceedings*, **436**, 115-120.

4.10 Tables

Table 4.1 Comparison of the solutions for pressurized blister geometry [a]

Authors	r	$G/(pV/A)$
Sizemore (1995)	$19.6W_0^3 + 2\beta_0^2 W_0$	$\frac{359W_0^4 + 42.4W_0^2\beta_0^2 + \beta_0^4}{28.7W_0^4 + 39.1W_0^2\beta_0^2 + \beta_0^4}$
Williams (1997)	Not provided	$\frac{15W_0^2 + 1.15\beta_0^2}{12W_0^2 + 1.15\beta_0^2}$
Allen (1988)?	$20.8W_0^3 + 2\beta_0^2 W_0$	$\frac{15W_0^2 + 1.15\beta_0^2}{12W_0^2 + 1.15\beta_0^2}$
Lin (1990)	$32W_0 + 21.88W_0^3 + 2\beta_0^2 W_0$	Not provided
Gent and Lewandowski (1987)[b]	$18.82W_0^3$	1.125
Present Analysis	$32W_0 + 15.47W_0^3 + 2\beta_0^2 W_0$	$\frac{55.24 + 22.26W_0^2 + 1.15\beta_0^2}{36.82 + 17.8W_0^2 + 1.15\beta_0^2}$

a: Poisson's Ratio ν=0.3 for calculation.

b: residual stress is not considered

4.11 Figures

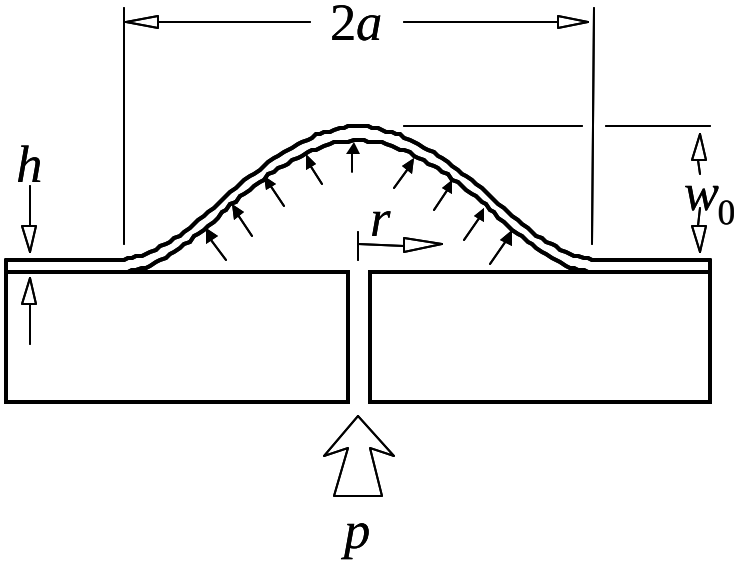

(a)

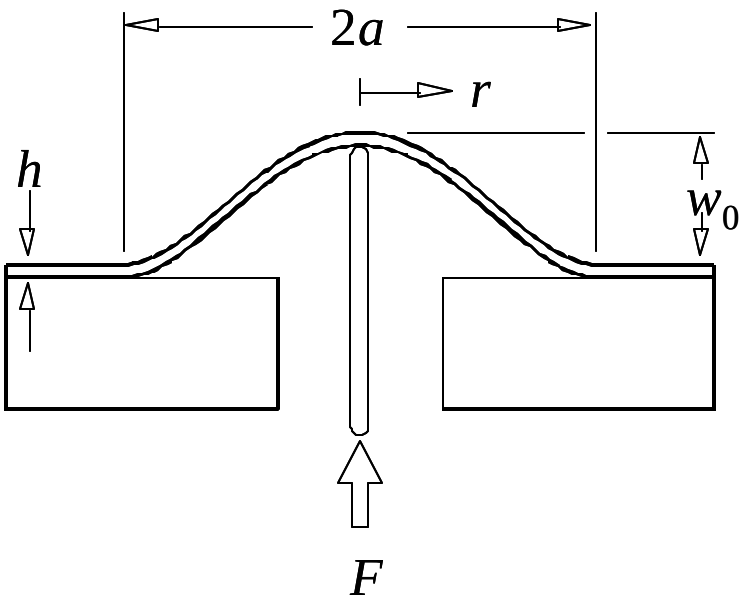

(b)

Figure 4.1 Schematics of the loading configurations for (a) pressurized blister; (b) shaft-loaded blister (After Wan *et al.* [16]).

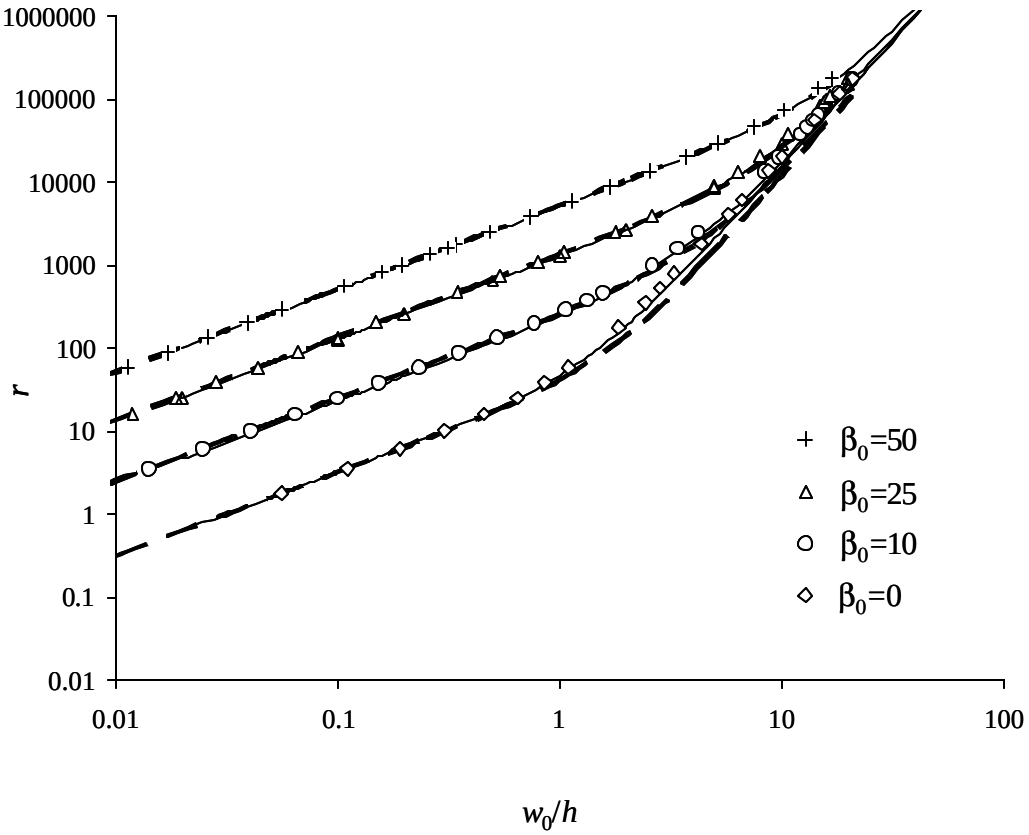
1000000
100000
10000
1000
100
10
1
0.1
0.01
r
0.01
0.1
1
10
100
β0=50
β0=25
β0=10
β0=0
w0/h

(a)

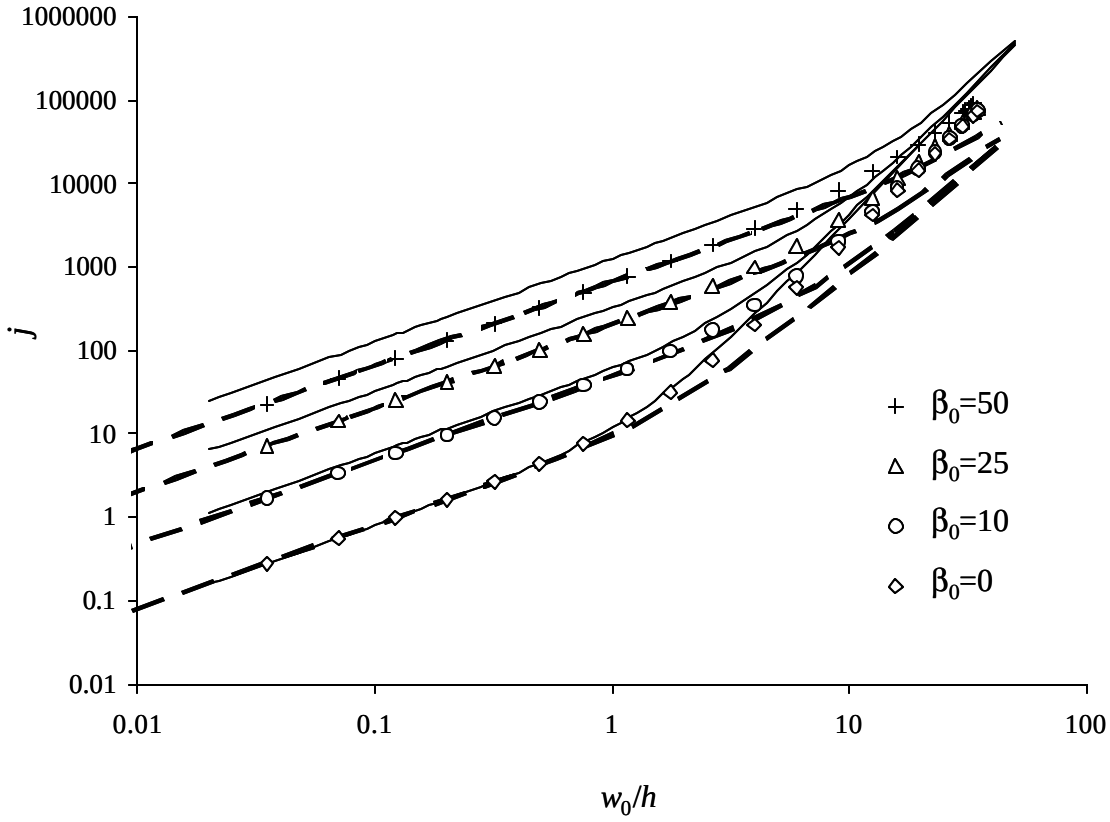

(b)

Figure 4.2 Constitutive relations for the two blister geometries. Analytical solutions from Wan *et al.* [19] are shown as broken lines, solutions based on principle of virtual displacements as solid lines, and FEA as data points. (a) pressurized blister. (b) central point loaded blister.

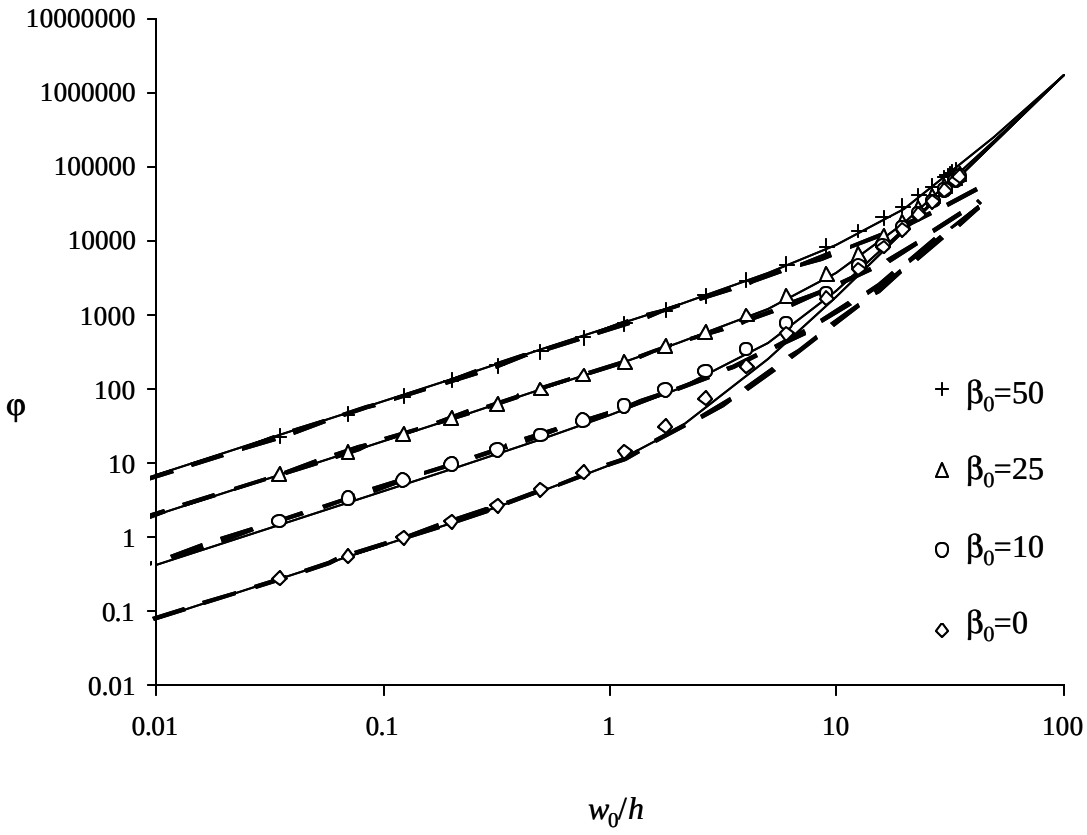

Figure 4.3 Constitutive relations for the shaft-loaded blister geometry. Modified analytical solution is shown as lines, Wan's solution [16] as dotted lines, and FEA as data points.

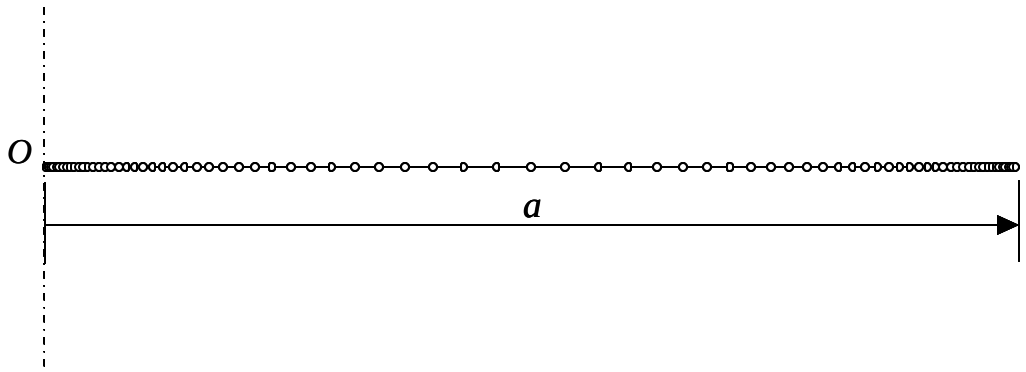

Figure 4.4 Axisymmetric element mesh used in the finite element analysis

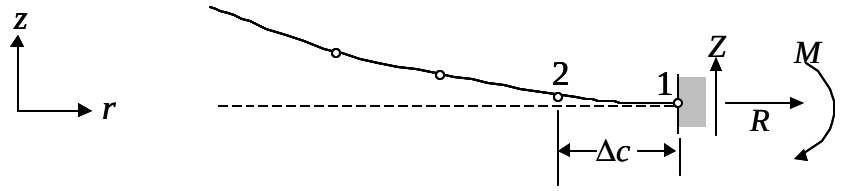

Figure 4.5 Schematic of crack front in axisymmetric blister using shell element. Dotted line represents the position of interface.

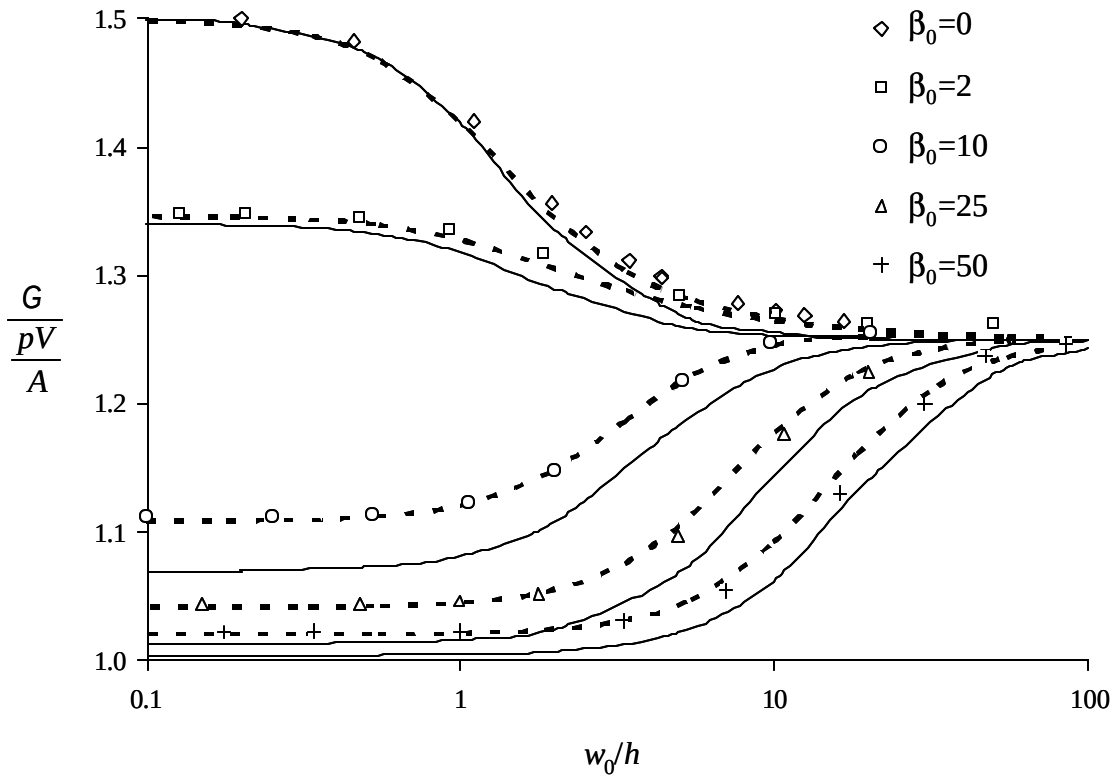

(a)

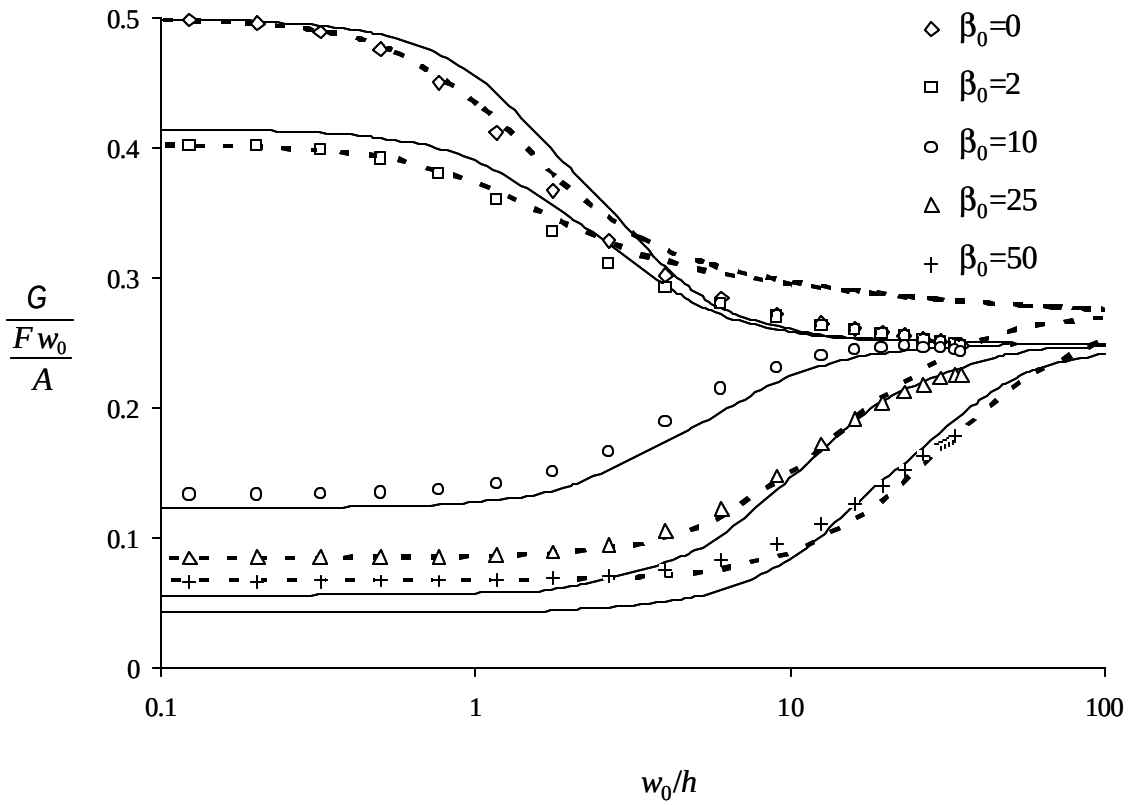

(b)

Figure 4.6 Normalized strain energy release rate as a function of central deflection W_0. Solutions based on the principle of virtual displacements are shown as lines, and FEA as data points. (a) pressurized blister. (b) central point loaded blister.

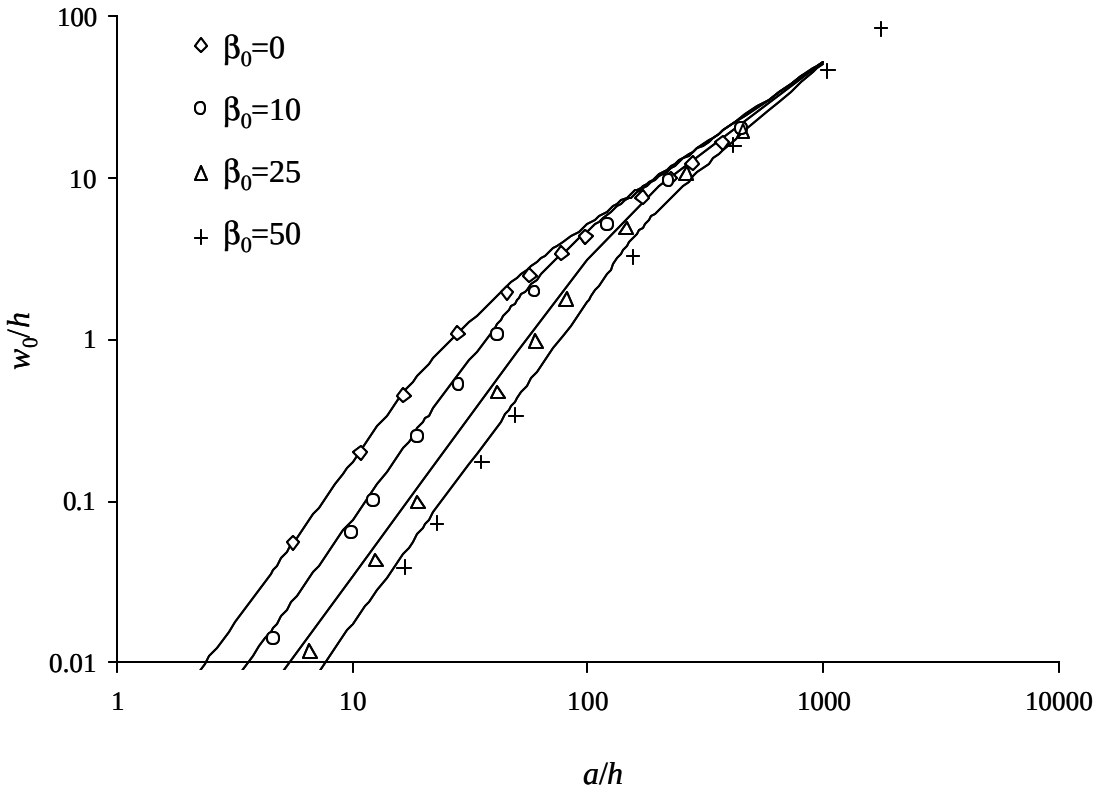
100
10
1
0.1
0.01
1
10
100
1000
10000
w_0/h
a/h
β_0=0
β_0=10
β_0=25
β_0=50

(a)

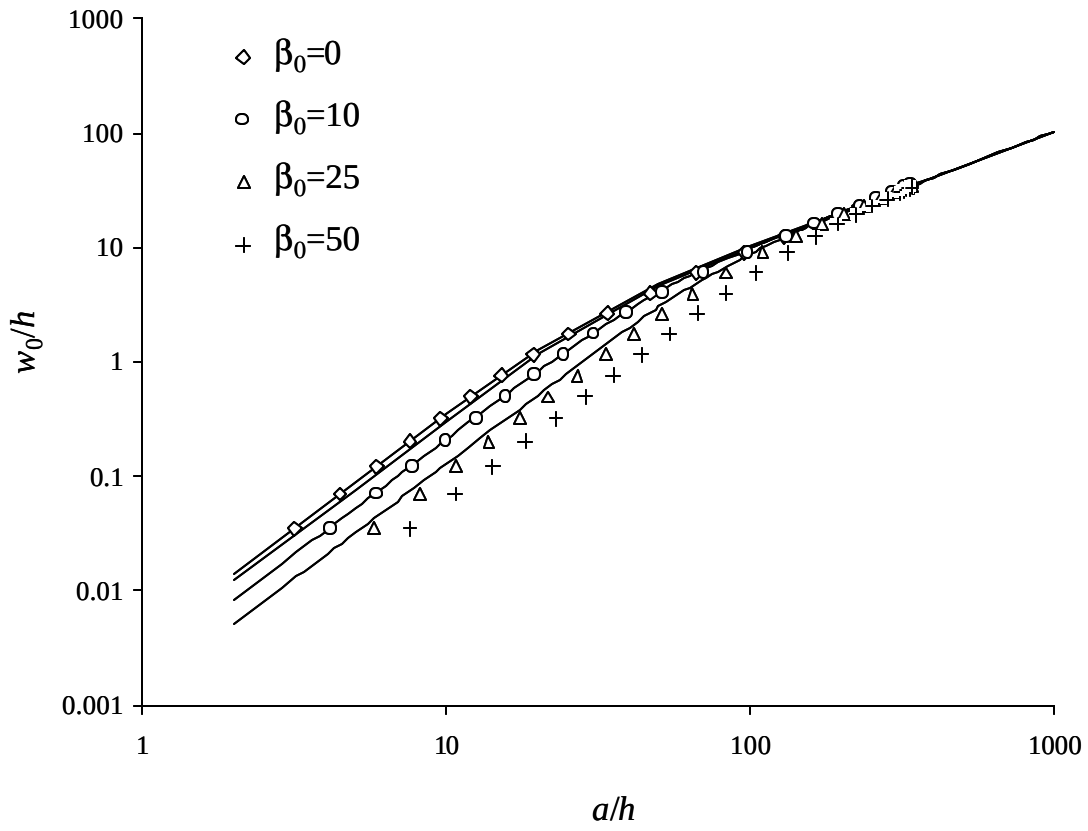

(b)

Figure 4.7 Central deflection as a function of blister radius during debonding. Analytical solutions based on the principle of virtual displacements are shown as solid lines, and FEA as data points. (a) pressurized blister. (b) central point loaded blister.

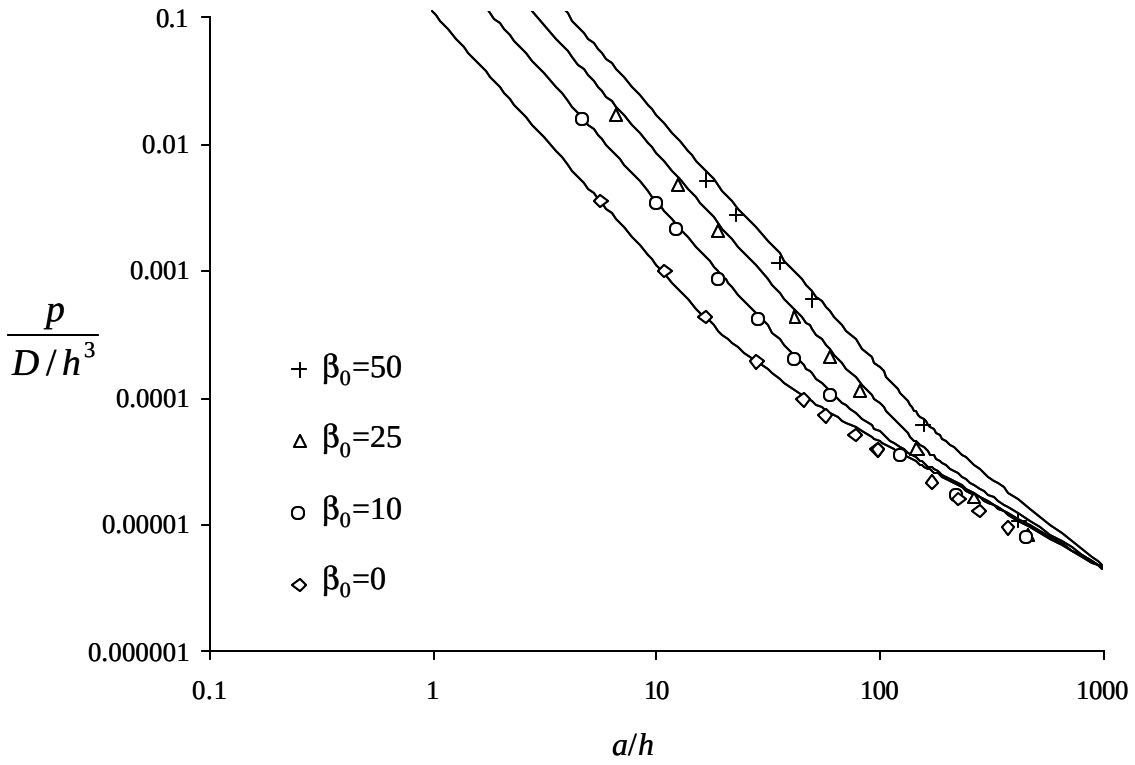
0.1
0.01
0.001
0.0001
0.00001
0.000001
p / D / h^3
β0=50
β0=25
β0=10
β0=0
0.1
1
10
100
1000
a/h

(a)

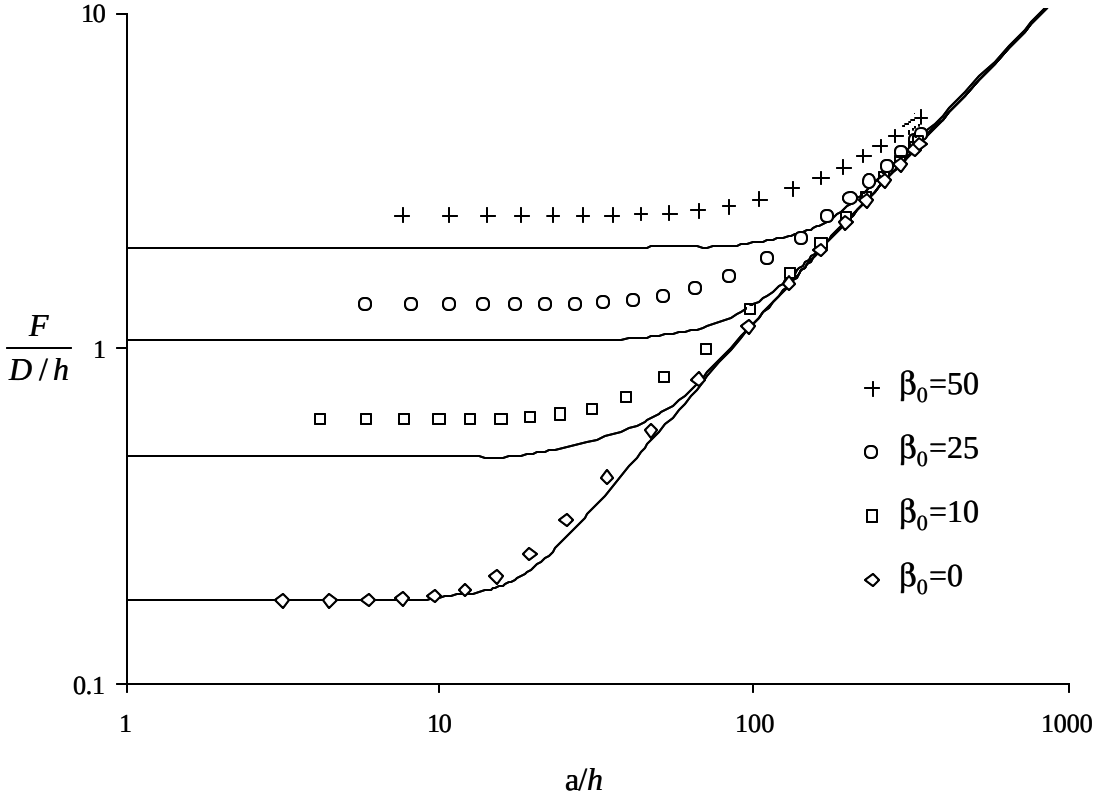

(b)

Figure 4.8 Applied load as a function of blister radius during debonding. Analytical solutions based on the principle of virtual displacements are shown as solid lines, and FEA as data points. (a) pressurized blister. (b) central point loaded blister.

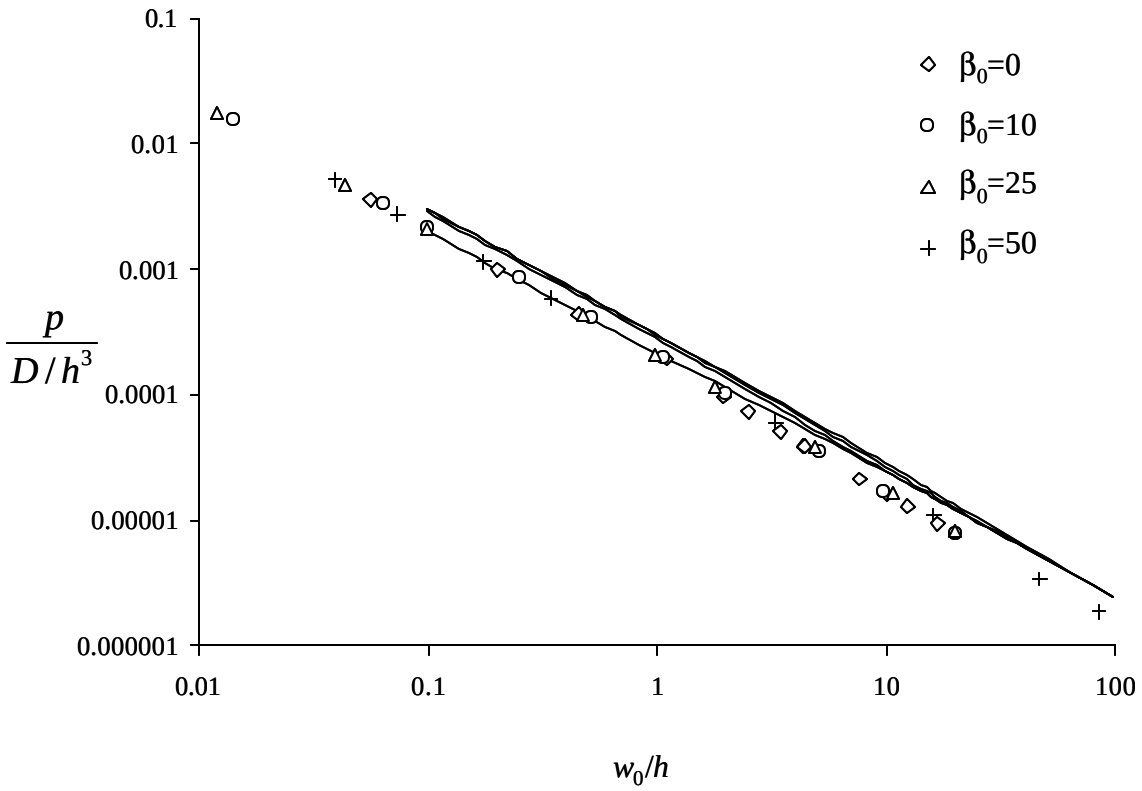
0.1
0.01
0.001
0.0001
0.00001
0.000001
$\frac{p}{D/h^3}$
0.01
0.1
1
10
100
w_0/h
β_0=0
β_0=10
β_0=25
β_0=50

(a)

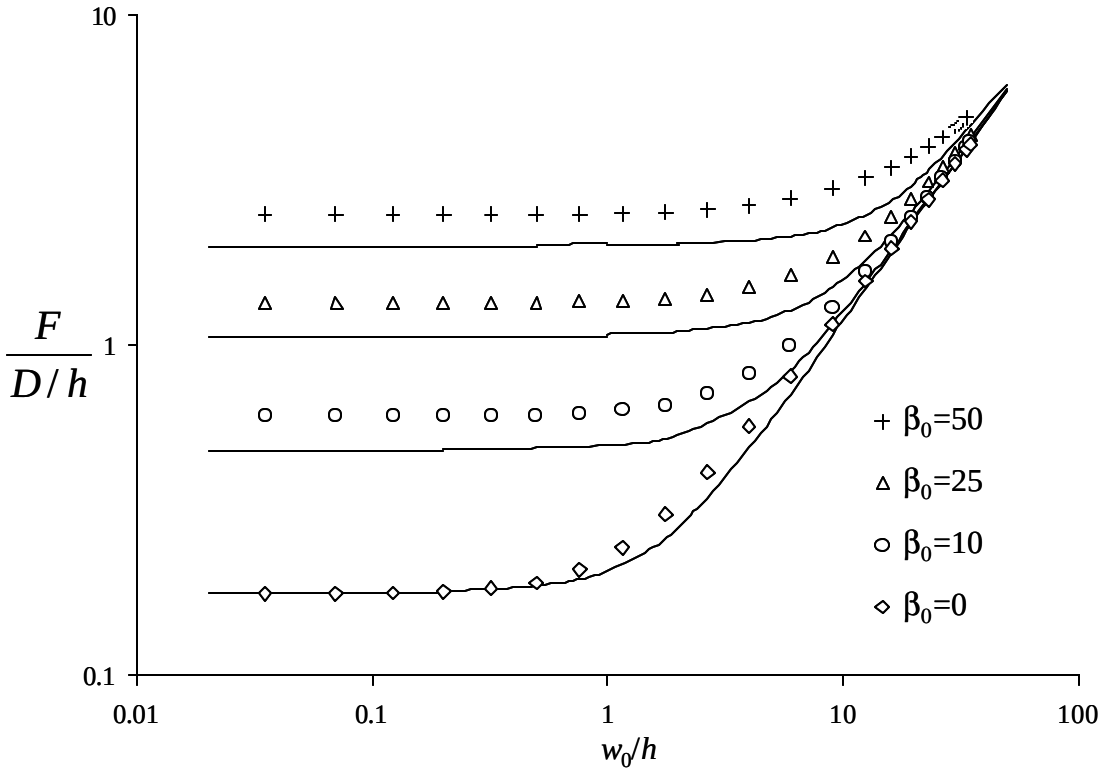

(b)

Figure 4.9 Applied load as a function of central deflection during debonding. Analytical solutions based on the principle of virtual displacements are shown as solid lines, and FEA as data points. (a) pressurized blister. (b) central point loaded blister.

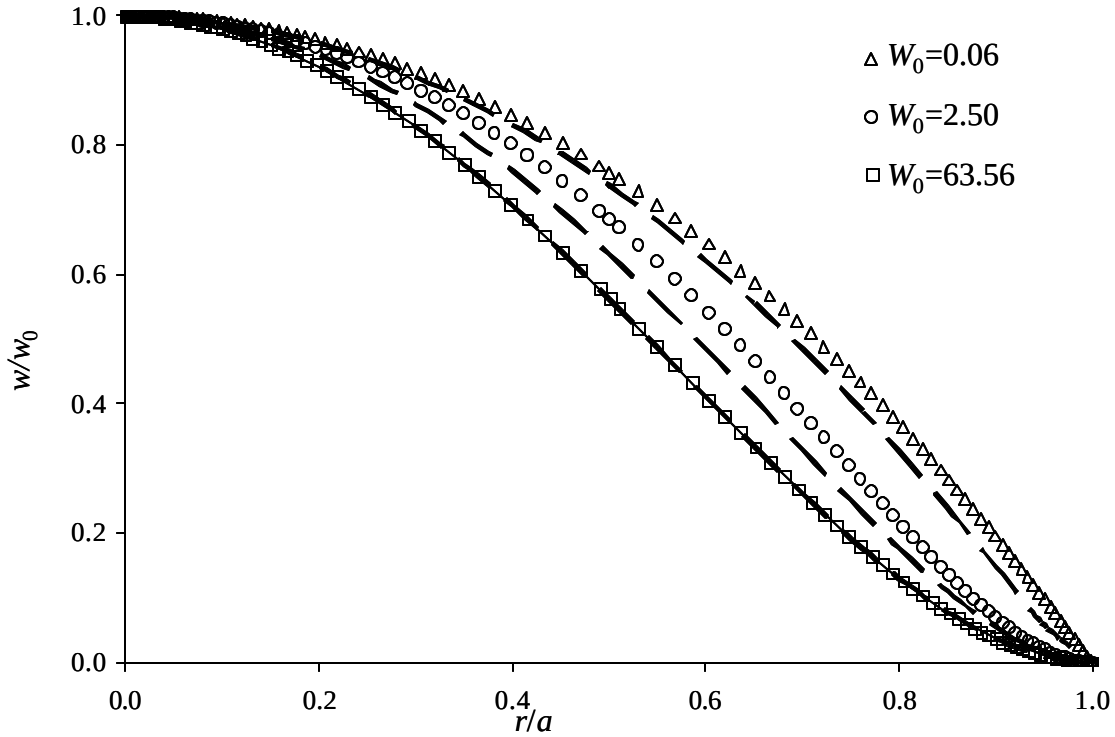

(a)

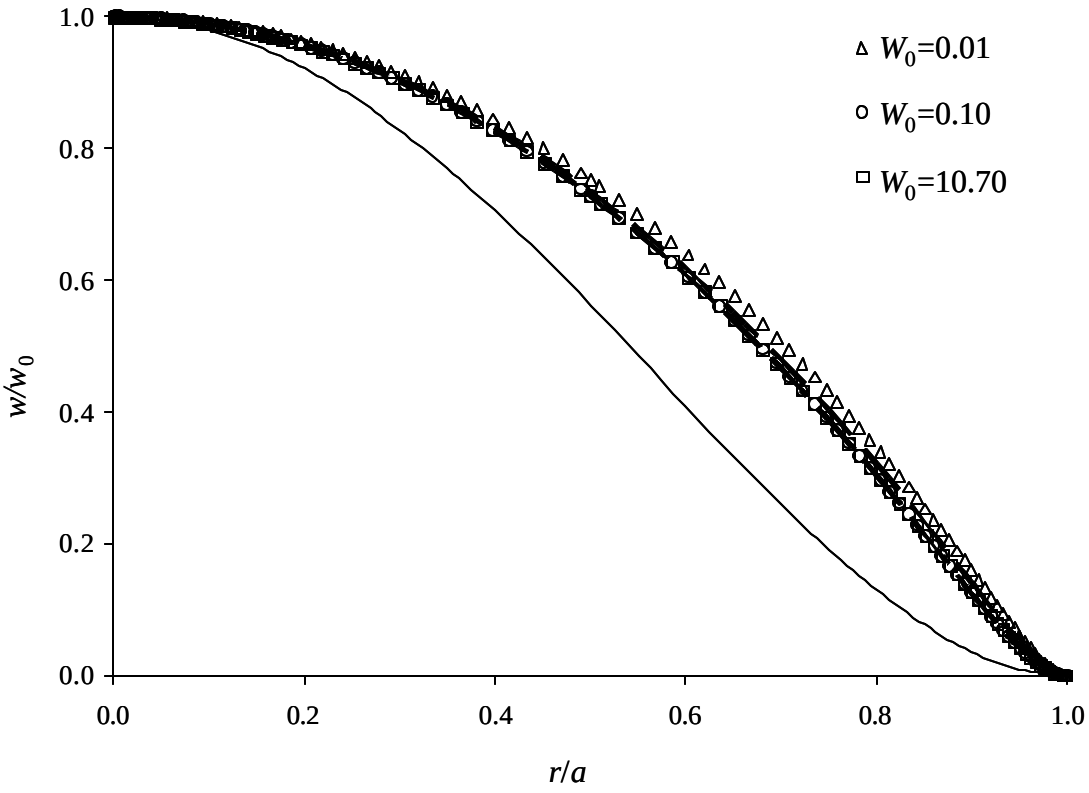

(b)

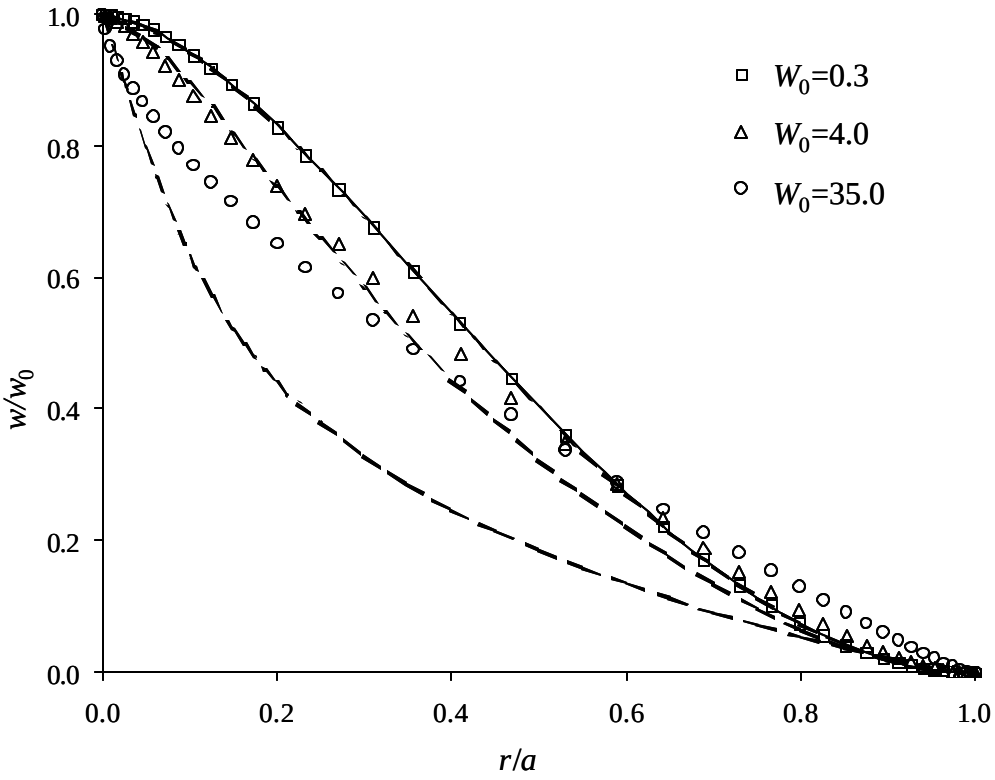

(c)

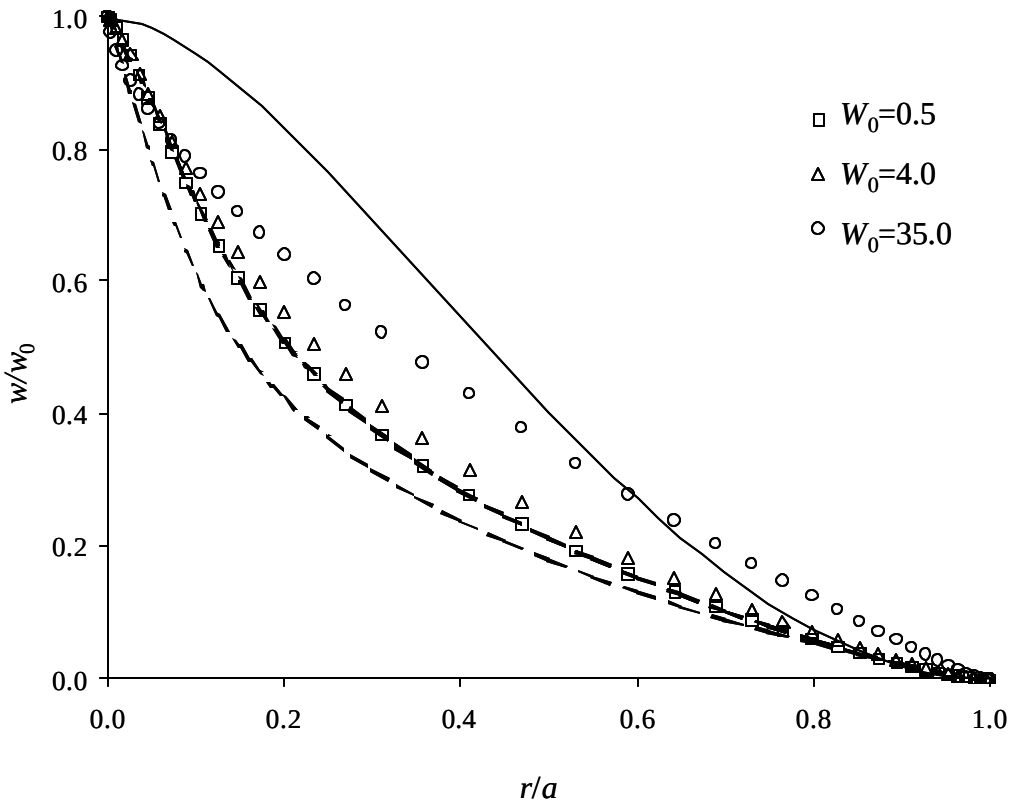

(d)

Figure 4.10 Normalized blister profile. Analytical solutions from Wan *et al.* [19] are shown as broken lines, solutions based on principle of virtual displacements as solid lines, and FEA as data points. (a) pressurized blister for β_0=0. (b) pressurized blister for β_0=25. (c) central point loaded blister for β_0=0. (d) central point loaded blister for β_0=25.

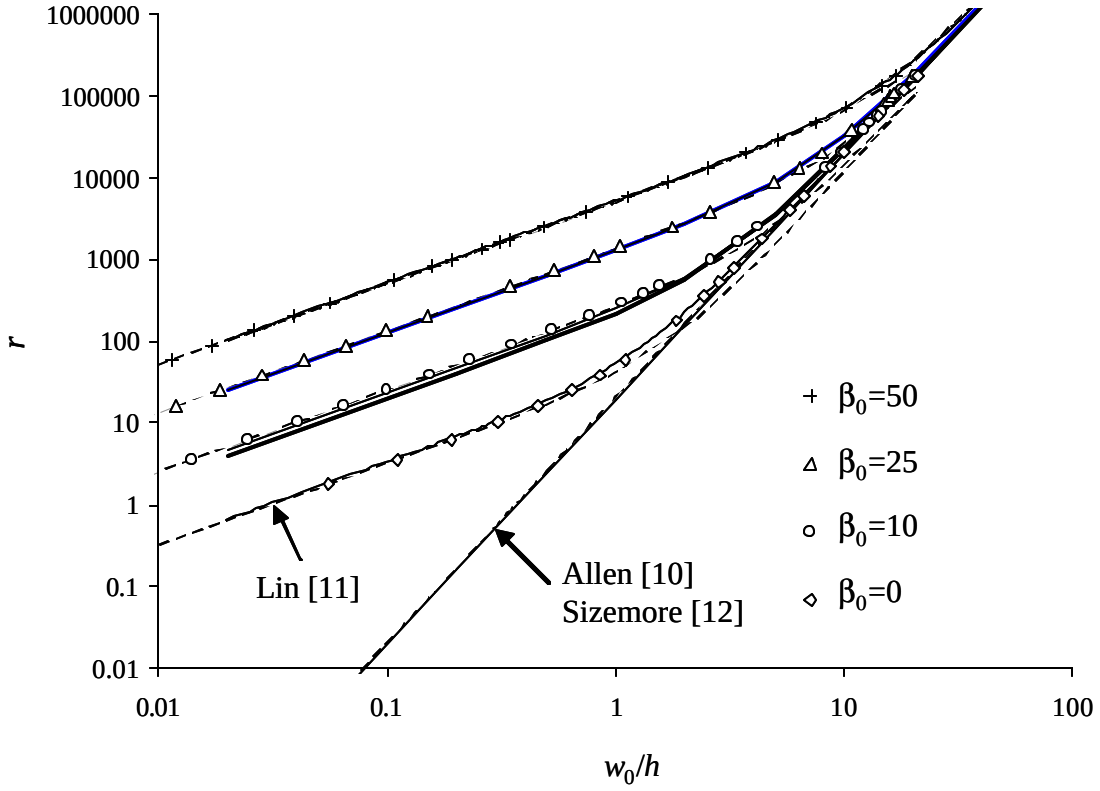

Figure 4.11 Constitute relations for the pressurized blister geometry from different solutions listed in Table 4.1. Data points are FEA results as comparison. The curves for non-zero β_0 from Allen [10], Sizemore [12] and Lin [11] superimpose with FEA results.

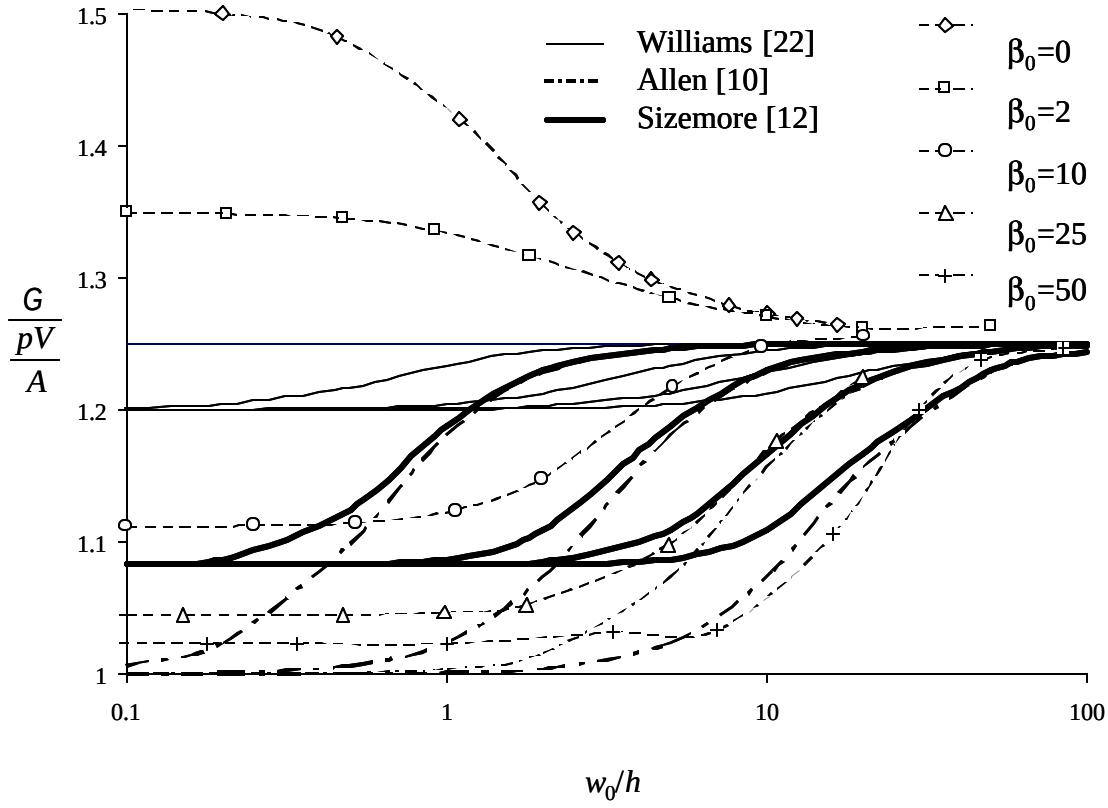

Figure 4.12 Normalized strain energy release rate as a function of central deflection W_0 from the solutions listed in Table 4.1. FEA results are shown as data points for comparison.

CHAPTER 5

INVESTIGATION ON THE BOUNDARY CONDITIONS OF A SINGLE-LAP JOINT

(To be submitted to *Journal of Adhesion Science and Technology*)

5.1 Abstract

The mechanics of a single-lap joint with different boundary conditions subjected to tensile loading are investigated. Closed-form solutions are obtained for a specimen configuration considering different clamping methods. Based on the approach pioneered by Goland and Reissner, the solutions reported in this paper provide a simple but useful way to understand the effects of boundary conditions on this test geometry. The solutions in this study suggest that different grip configurations mainly affect the response of the specimens if the grip position is close to the joint edge or the loads are small. Generally, the influence caused by different gripping methods is only limited to the boundary region, and the behavior of the joint part subjected to tensile loading is almost the same as that for a simply-supported case.

Keywords: single-lap joint, boundary conditions, clamp, simply-supported, spacer.

5.2 Introduction

Single-lap joints are widely used for adhesively bonded specimens and industrial products. Due to simplicity in testing, the single-lap joint has been adopted as a standard mechanical test method for determining the apparent shear strength (ASTM D1002) and shear modulus (ASTM D3983) of adhesive bonds. For the purpose of determining material properties and structural bonding application, the single-lap joint must be analyzed in detail in order to obtain the correct understanding of the stress distributions in both adhesive layers and adherends. Stress analysis of single-lap joints has undergone a long development and refinement for more than half a century. The earliest analysis of a single-lap joint geometry was conducted by Volkersen [1]. This simple shear lag model was based on the assumption of pure tensile deformation in the adherends and no axial stiffness of the adhesive. Later, Goland and Reissner [2] published their classic paper where a cylindrically bent, plate model was adopted to facilitate their analysis. Their paper can be divided into two parts. In part one, Goland and Reissner determined the internal loads (bending moment and shear force) at a joint edge. They assumed that the adhesive was so thin compared with adherends' thickness that the adhesive thickness could be ignored for the geometric determination of bending moment and transverse shear. The analysis took account of the large deflection for the adherends and bonded joint. The bending flexural rigidity of the overlap was calculated by assuming that the two adherends were lumped together. In part two, the peel and shear stress distributions along the joint were analyzed for two cases: thin stiff adhesive and thicker soft adhesive. For the case of a thin, stiff adhesive, the overall overlap was treated as a single deformed body, with the same material properties as the adherend for such joints. An approximate solution was derived by solving the elastic boundary-value problem with a given moment and tensile load at the end of overlap, and neglecting the transverse shear force. For the case of a thicker soft adhesive, the stress analysis was conducted based on the assumption that the deformation of adherends arises only from the longitudinal stresses, since the transverse normal strain and shear strain in adherends were relatively small compared with those in the adhesive. Although Goland and Reissner were inconsistent with the sign of shear force, they still obtained the correct result for transverse normal stress by a

second inconsistency in their analysis [3]. Sneddon [4] pointed out the inconsistency, but failed to obtain the correct solutions by using the equation with inconsistent sign. Later, Hart-Smith [5] proposed an modified model that removes the lumped overlap assumption by treating the adherends as beams on elastic foundations, and gave the stress solution for linear elastic and elastic-plastic adhesives. In the early 1990s, Oplinger [6] developed a layered beam analysis, which included treatment of large deflection of the joint overlap. Along with the one-dimensional analysis, several researchers have employed energy methods for obtaining the two-dimensional solutions [6-8]. They mainly focused on the joint and overlap, and ensured the stress-free boundary conditions at the free end. Besides analytical approaches, the finite element method has been used either linearly [9, 10], or nonlinearly [11, 12] (both geometrically and materially). As a review, Tsai and Morton [3] gave a comprehensive evaluation of both the analytical and numerical solutions to single-lap joints. Another application branch of single lap joints is to measure the debonding strength of adhesive joints, thus, fracture mechanics of the cracked lap-joint specimens was also studied extensively [12-14], in addition to the deformation and stress analysis. Using the approach of Goland and Reissner [5], Lai, *et al.* [15] reported a closed-form solution for cracked lap shear specimens with different boundary conditions, showing that the energy release rate was significantly affected by end conditions and debond length.

Most researchers analyzed SLJ by assuming that the specimens were simply supported. The effect of boundary conditions in a single-lap joint was only studied briefly by Penado [16] using the approach of Goland and Reissner. Penado conducted a stress analysis for a SLJ made of composite adherends, and claimed that the deformation of a single-lap joint is not sensitive to the support conditions at the end of the adherends. However, the grip conditions during the actual tests are not always the same as in the solutions available. Figure 5.1 shows the schematic of two typical grip methods used in testing single-lap joints. It is obvious that the boundary conditions for these two configurations are different due to the offset between two adherends. This difference becomes more significant when the adherends are thick and adhesion is weak. The analysis on this special, yet common configuration in experiments has not been found in

the literatures. Therefore, in this chapter, the analytical solutions to a single-lap joint with the two grip conditions will be studied using Goland and Reissner's approach.

5.3 Mathematical Formulations

5.3.1 Clamped-clamped configuration with an initial end deflection

The configuration of a single-lap joint specimen and related parameters are shown in Figure 5.2. Following Goland and Reissner's method, the adhesive layer is assumed to be so thin compared with the adherends that it is ignored in the following analysis. An end deflection of $(t\text{-}\Delta)/2$ is introduced to simulate the gripping configuration, in which a spacer with thickness of Δ is inserted between each end of the specimen, where t is the adherends' thickness. If $\Delta=t$, no bending moment is produced by gripping prior to loading, as the analysis available [16]. If there are no applied spacers, $\Delta=0$. In actual testing configuration, one of the two grips is sometimes free to rotate during pulling, however, this feature is not considered in this study due to mathematical difficulty.

Now consider the static equilibrium of the single-lap joint that is divided into two regions, with origins denoted by x_1 and x_2 respectively. The initial end deflection, $(t\text{-}\Delta)/2$, end moment, M_0, and shear force, V_0, depend on the clamping conditions of the grips of the testing machine and will be discussed in detail later. Setting M_1,the moment in the sheet in region 1 and M_2, the moment in the joint region, each per unit width, then

$$\begin{aligned} M_1 &= -T\left[w_1 - \frac{1}{2}(t-\Delta) \right] + V_0 x_1 + M_0 \\ M_2 &= -T(w_2 + \Delta) + V_0(L + x_2) + M_0 \end{aligned} \tag{1}$$

The positive convention chosen for moments and transverse shear forces are illustrated in Figure 5.2. According to the theory for the small bending of thin,

cylindrically bent plates, the differential equations for the transverse deflections of the sheet and joint become

$$\begin{aligned} \frac{d^2 w_1}{dx_1^{\,2}} &= -\frac{M_1}{D_1}, \quad 0 \le x_1 \le L \\ \frac{d^2 w_2}{dx_2^{\,2}} &= -\frac{M_2}{D_2}, \quad 0 \le x_2 \le c \end{aligned} \tag{2}$$

where D_1 and D_2 are the flexural rigidities of the sheet and joint, respectively, and D_2=8D_1.

The two proceeding equations have solutions of the form

$$\begin{aligned} w_1 &= A_1 \cosh u_1 x_1 + B_1 \sinh u_1 x_1 + \frac{1}{2}(t-\Delta) + \frac{1}{T} V_0 x_1 - \frac{1}{T} M_0 \\ w_2 &= A_2 \cosh u_2 x_2 + B_2 \sinh u_2 x_2 + \Delta + \frac{V_0}{T}(L + x_2) - \frac{M_0}{T} \end{aligned} \tag{3}$$

where

$$u_1 = \sqrt{\frac{T}{D_1}} \quad \text{and} \quad u_2 = \sqrt{\frac{T}{D_2}}$$

There exist six unknowns in this solution, A_1, B_1, A_2, B_2, V_0, and M_0. They can be readily determined by incorporating the following six boundary conditions.

$$\text{at } x_1 = 0 \qquad\qquad w_1 = \frac{1}{2}(t-\Delta)$$

$$\text{at } x_1 = 0 \qquad \frac{dw_1}{dx_1} = 0$$

$$\text{at } x_1 = L, x_2 = 0 \qquad w_1 = w_2$$

$$\text{at } x_1 = L, x_2 = 0 \qquad \frac{dw_1}{dx_1} = \frac{dw_2}{dx_2}$$

$$\text{at } x_2 = c \qquad w_2 = 0$$

$$\text{at } x_2 = c \qquad \frac{d^2 w_2}{dx_2^{\,2}} = 0$$

After determining these unknowns, the internal forces in the specimen can be obtained using the solutions in (3). Here, the lengthy expressions are not listed.

5.3.2 Simply-Simply supported configuration

For completeness, the analysis for the simply supported SLJ configuration is listed in this subsection. The details are from Goland and Reissner's classic work[2].

The moment in the sheet region and overlap region are as follows:

$$\begin{aligned} M_1 &= -T(w_1 - a_n x_1) \\ M_2 &= -T\left[w_2 + \frac{t}{2} - a_n(L + x_2)\right] \end{aligned} \tag{4}$$

where α_n represents the angle between x_1 (or x_2) axis and the line of load action, and is approximately given by

$$a_n = \frac{1}{2}\frac{t}{L + c}$$

The equilibrium equations for the two regions are the same as (3), and the solutions for the simply supported case are

$$\begin{aligned} w_1 &= A_1 \cosh u_1 x_1 + B_1 \sinh u_1 x_1 + a_n x_1 \\ w_2 &= A_2 \cosh u_2 x_2 + B_2 \sinh u_2 x_2 + a_n x_1 (L + x_2) + -\frac{t}{2} \end{aligned} \tag{5}$$

where the variables are the same as defined in (3).

The four unknowns can be obtained by applying the following boundary conditions

$$\begin{aligned} \text{at } x_1 = 0 \qquad & w_1 = 0 \\ \text{at } x_1 = L, x_2 = 0 \qquad & w_1 = w_2 \\ \text{at } x_1 = L, x_2 = 0 \qquad & \frac{dw_1}{dx_1} = \frac{dw_2}{dx_2} \\ \text{at } x_2 = c \qquad & w_2 = 0 \end{aligned}$$

The complete solutions for the simply-simply supported case can be found in Goland and Reissner's classic paper [2]. Because the emphasis of this chapter is on the gripping of a SLJ, the following sections mainly discuss how a specimen responds if spacers of different thickness are added.

5.4 Discussion

5.4.1 Moment at the transition section

A crucial parameter in almost all the analyses available is the joint edge moment M_t. Thus it is instructive to present how grip conditions affect M_t. The formulation of M_t from Goland and Reissner's solution, the modified Goland and Reissner's solution by Tsai and Morton [3], and the results obtained in this dissertation are discussed here. By applying the approximations of

$$\sinh u_1 L \approx \cosh u_1 L \approx \frac{1}{2} Exp[u_1 L]$$

Goland and Reissner found the edge moment to be:

$$M_t = k \frac{Tt}{2}$$

where

$$k = \frac{1}{1 + 2\sqrt{2} \tanh(\frac{u_2 c}{2\sqrt{2}})} \tag{6}$$

Releasing the above approximation, Tsai and Morton obtained k as

$$k = \frac{1}{1 + 2\sqrt{2} \tanh(\frac{u_2 c}{2\sqrt{2}}) \cosh(u_2 L)} \tag{7}$$

Using the solutions obtained in the preceding section for the clamped-clamped boundary conditions with a spacer of thickness of $t/2$,

$$k = \frac{-2\sqrt{2}\tanh(u_2 c) + [u_1(L+c) - \tanh(u_1 L)]}{[u_1(L+c) - \tanh(u_1 L)] + 2\sqrt{2}\tanh(u_2 c)[u_1(L+c)\tanh(u_1 L) - 1]} \tag{8}$$

Equations (6) ~ (8) are plotted in Figure 5.3 as functions of $u_1 c$. Goland and Reissner [2] suggested using $u_1 c$ to characterize joint length. However, $u_1 c$ represents both load level and joint length. On one hand, $u_1 c$ may be much bigger than one if the joint is under sufficiently high loads, though c/t could be sufficiently small, while on the other hand, $u_1 c$ is still in a small region if the load is small, though the joint may be sufficiently long (large c/t). Therefore, this definition is more appropriate for the joint with either low failure loads, or very thick adherends, in which $u_1 c$ remains small.

Generally, k is a function of both $u_1 c$ and L/c for both boundary conditions. However, for the case of very long unsupported adherends (L/c>100), k no longer depends on L/c, thus Goland and Reissner's formulation in (4) is sufficiently accurate. Furthermore, all the curves converge asymptotically to k=0.26 for large $u_1 c$. Hart-Smith [4] claimed that k approaches zero if L is infinitely long and the adhesive layer is modeled as an elastic foundation beam in his solutions. Tsai and Morton [3] showed that Goland and Reissner's solution is more accurate than that of Hart-Smith.

Clamping the ends of a SLJ specimen tends to relieve the moment at the joint edge, but it only works effectively on the specimens with short unsupported adherends (small L/c), or small $u_1 c$, which represent either small loads, or short joints (small c). When L/c>100, or $u_1 c$ >>1, no difference in k can be noticed between the two types of boundary conditions.

If a specimen is clamped without including spacers, reactive moments are generated at the ends during the mounting step. The influence of spacers on k is demonstrated in Figure 5.4 for three typical specimen configurations with different lenghs of the unsupported adherends. If no spacer is included between a specimen and grips, or the spacer is thinner than the adherend's thickness (here, the thickness of adhesive layer is ignored), the reactive moment at the gripping ends transfers to the joint edge, thus k is infinite at u_1c=0 (T=0) because k is defined as $M_t/(T\ t/2)$. If the length of the unbonded adherend sheets is similar to that of overlap, the moment at the joint edge is strongly sensitive to the thickness of the spacer if u_1c <1. However, for the specimens with very long unbonded sheets (L/c>100), the spacer's contribution to k is again nearly zero, except k is infinite when u_1c=0, as shown in Figure 5.4 (c).

5.4.2 Deflection and rotation profiles

Figure 5.5 demonstrates the influence of the spacer on the transverse deflections of the specimens, and the discussions are made on the joints with three typical different adherends. When a joint's length is similar to the length of the extended adherends, the specimen's deflection is significantly reduced by adding a space between the grips and specimen. Furthermore, the reduced deflection subsequently decreases the bending moment at the transition section. On the other hand, the improvement is dependent on the thickness of the spacer. When the spacer has the same thickness with the adherend (ξ=0.5), the deflection can be almost totally removed if the loading is not so high (u_1c=1 is adopted in this figure). However, if the unsupported adherends are sufficiently long (L/c>100), the spacer does not affect the specimen's response under longitudinal loadings. Actually, the difference between a clamped case and simply-supported one disappears as well if long extended adherends are used. For completeness, the rotation angles are drawn in Figure 5.6.

5.4.3 Internal moment

Figure 5.7 illustrates the bending moment distribution along the extended adherend part of a specimen. Clamping boundary conditions cause negative bending moments at the specimen's ends, but the spacers applied between the grips and specimen

ends tend to transform the negative moments to positive ones. If a spacer with the thickness of the adherends is included, the moment at the gripping end is always positive. However, the different bending moments in the adherend caused by the spacers of different thickness have a trend to merge together at the joint edge. This phenomenon becomes more evident in the long adherend cases, where the different clamping boundary conditions produce a very localized effect. Therefore, for a specimen with very long extended adherends, no serious attention needs to be paid to gripping method.

5.5 Conclusions

This chapter reports a closed-form, geometrically nonlinear solution to single-lap joint specimens with practical clamping conditions where a spacer is inserted between the grips and the specimen. The solution is derived based on the cylindrically-bent plate approach pioneered by Goland and Reissner. The transverse deflection and bending moment along the specimen and at the transition section were emphasized although the stress distribution along the bondline could have been obtained. It is found that adding the spacers tends to reduce the deflection along the specimen, and minimize negative end moment. However this effect is important only if the clamping position is close to joint edge, or the external load is very small. If the grips are located far from the joint (L/c>10), or the load is very high ($u_1 c >> 1$) the experimental operators do not need to add spacers to release the extra loads from gripping in fixed grip machines.

5.6 References

1 Volkersen, O. (1938) Die Niekktraftverteiling in Zugbeanspruchten mit Konstanten Laschenquerschritten, *Luftfahrtforschung*, **15**, 41-47.

2 Goland, M. and Reissner, E. (1944) The stress in cemented joints, *Journal of Applied Mechanics*, **55**, 109-115.

3 Tsai, M. Y. and Morton, J. (1994) An evaluation of analytical and numerical solution to single-lap joint, *International Journal of Solids and Structures*, **31**, 2537-2563.

4 Sneddon, I. (1961) The distribution of stress in adhesive joints, *Adhesion*, Edited by D. D. Eley, Chapter 9, Oxford University Press, U.K.

5 Hart-Smith, L. J. (1973) *Adhesive-bonded single-lap joints.* NASA CR-112236.

6 Oplinger, D. W. (1991) A layer beam theory for single-lap joints, *U.S. Army Materials Technology Laboratory Report*, MTL TR91-23.

7 Allman, D. J. (1977) A theory for elastic stresses in adhesive bonded lap joints, *Quarterly Journal of Mechanics and Applied Mathematics*, **30**, 415-436.

8 Chen, D. and Cheng, S. (1983) An analysis of adhesive-bonded joints, *Journal of Applied Mechanics*, **50**, 109-115.

9 Adams, R. D. and Peppiatt, N. A. (1974) Stress analysis of adhesively bonded lap joints, *Journal of Strain Analysis*, **9**, 185-196.

10 Wooley, G. R. and Carver, D. R. (1971) Stress concentration factors for bonded lap joints, *Journal of Aircraft*, **8**, 847-821

11 Harris, J. A. and Adams R. D. (1984) Strength prediction of bonded single lap joints by non-linear finite element methods, *International Journal of Adhesion and Adhesives*, **4**, 65-78.

12 Brussat, T. R., Chiu, S. T. and Mostovoy, S. (1977) Fracture Mechanics for Structural Adhesive Bonds, *AFNL-TR-77-163, Air Force Materials Laboratory*, Wright-Patterson AFB, Ohio.

13 Lin, C., and Liechti, K. M. (1987) Similarity concepts in the fatigue fracture of adhesively bonded joints, *Journal of Adhesion*, **21**, 1-24.

14 Schmueser, D. W. and Johnson, N. L. (1990) Effect of bondline thickness on mixed-mode debonding of adhesive joints to electroprimed steel surfaces, *Journal of Adhesion*, **23**, 215-231.

15 Lai, Y-H., Rakestraw, M. D. and Dillard, D. A. (1996) The cracked lap shear specimen revisited-a closed form solution, *International Journal of Solids and Structures*, **33**, 1725-1743.

16 Penado, F. E. (1998) A simplified method for geometrically nonlinear analysis of the single lap joint, *Journal of Thermoplastic Composite Materials*, **11**, 272-287.

5.7 Figures

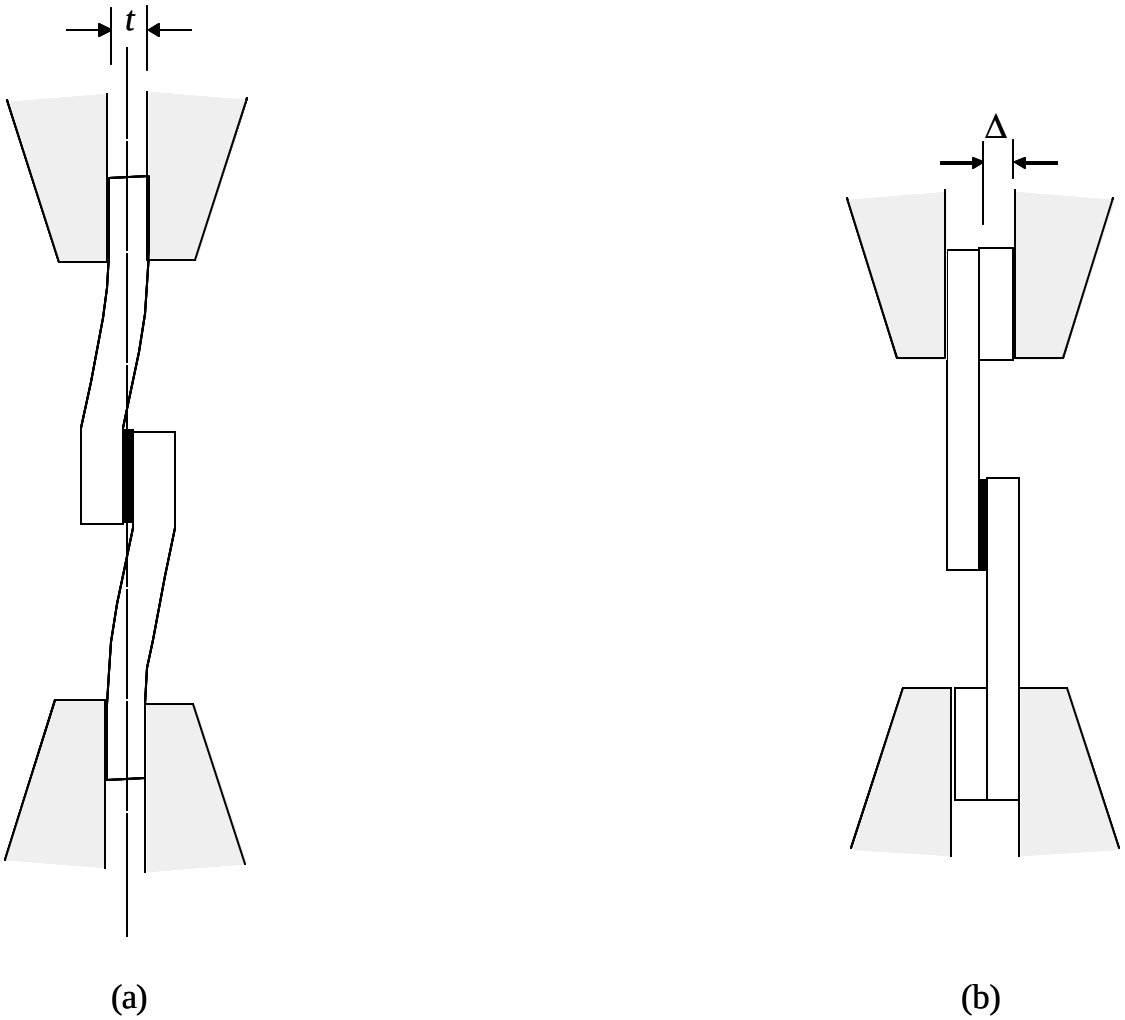

Figure 5.1 Schematics of two typical gripping conditions for a single-lap joint specimen. (a): The configuration without spacers. (b): Spacers are added to relieve the bending moments at the ends of the specimen.

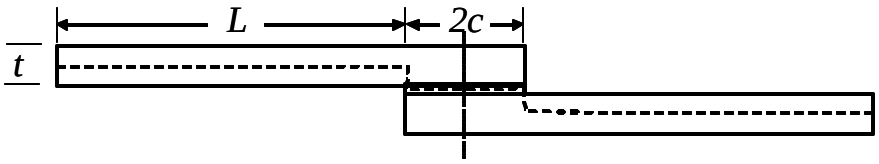

(a) Configuration of a single-lap joint specimen

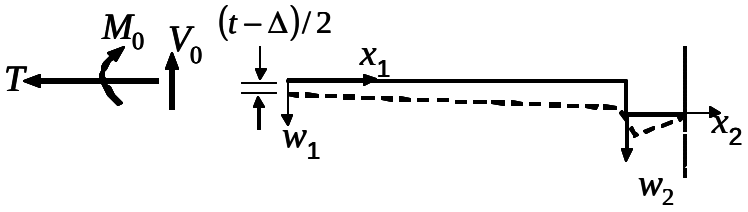

(b) Applied load, reactive forces and moments

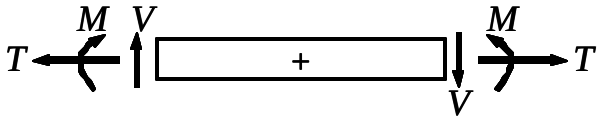

(c) Sign convention

Figure 5.2 Illustration of the single-lap joint configuration

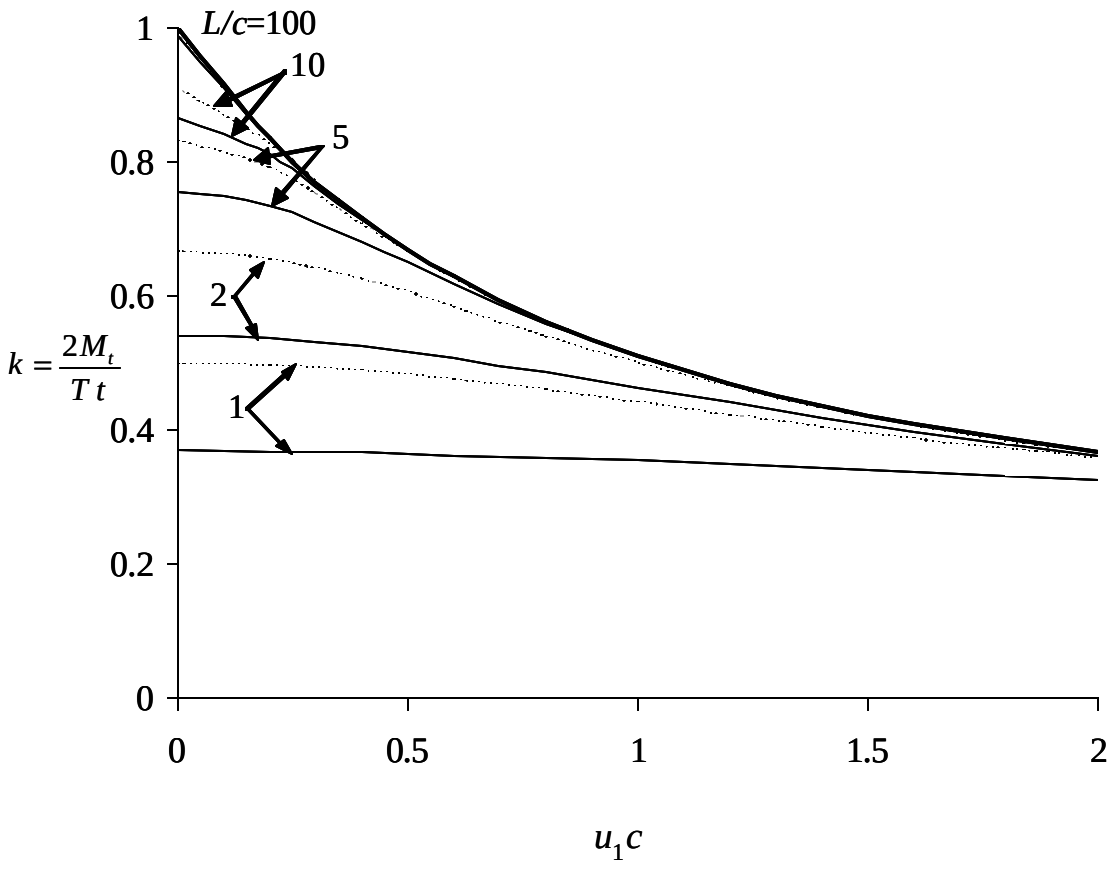

Figure 5.3 The normalized edge moment k as functions of normalized loads $u_1 c$ with variation of L/c. Solid lines stand for clamped cases with $\Delta=0$, and dotted lines represent simply-supported solution of Goland and Reissner.

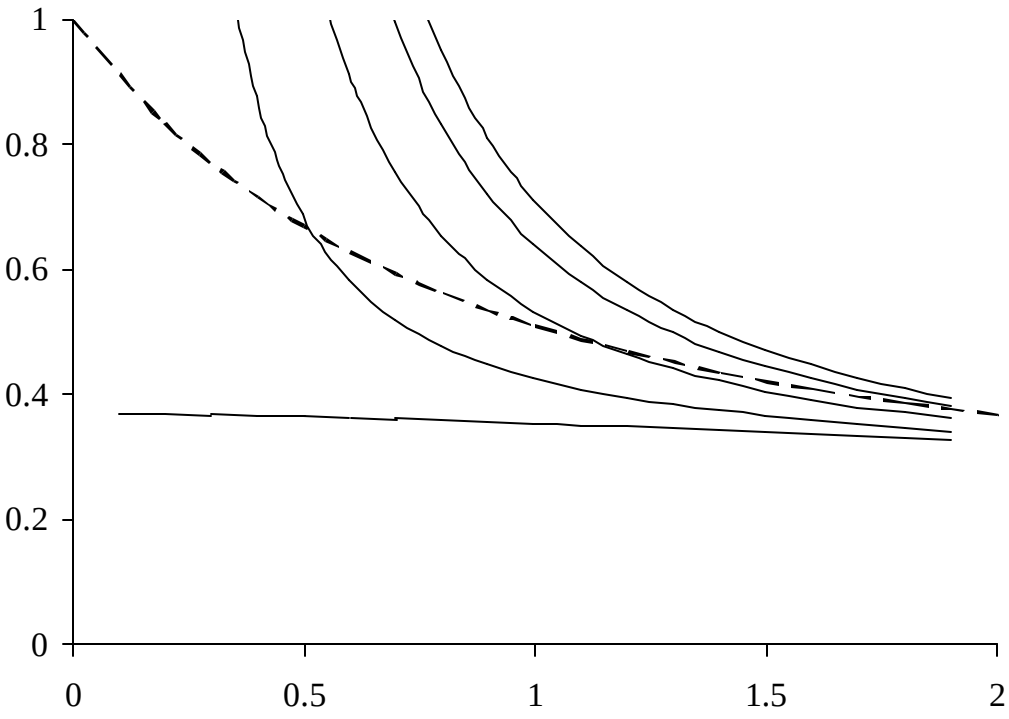

(a)

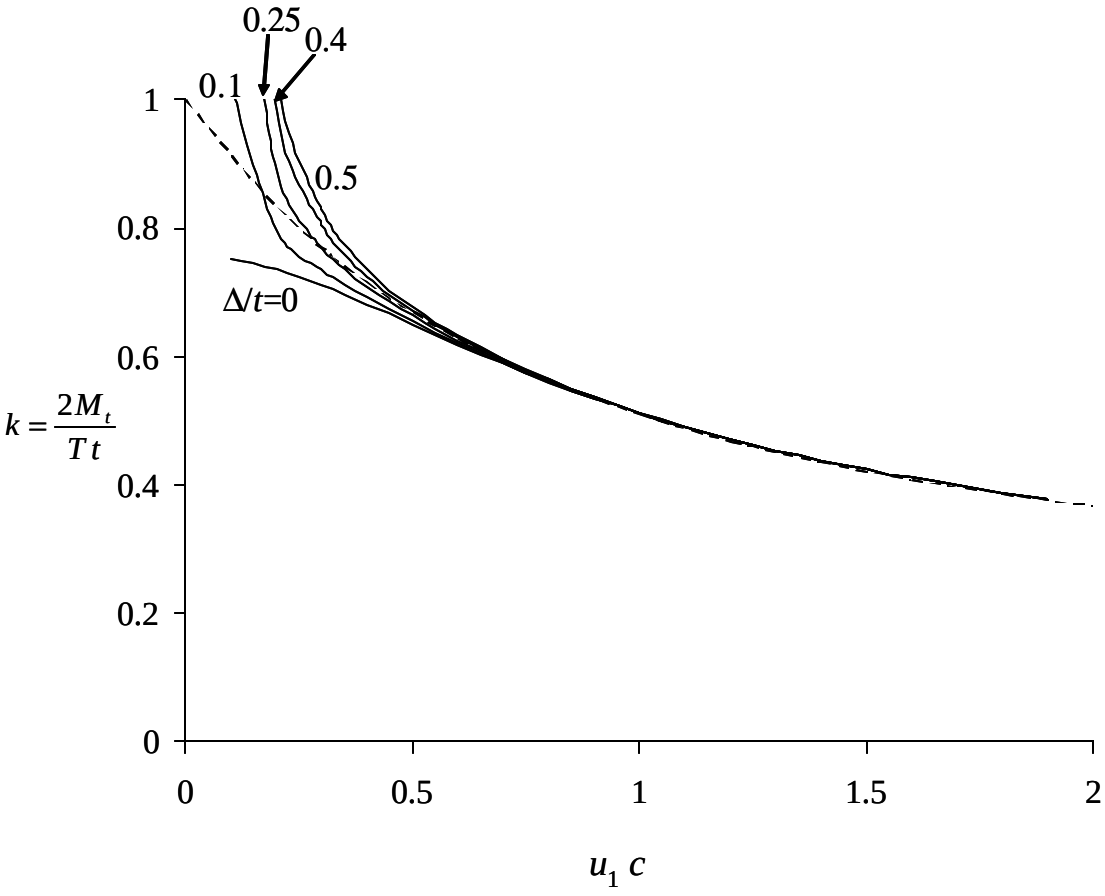

(b)

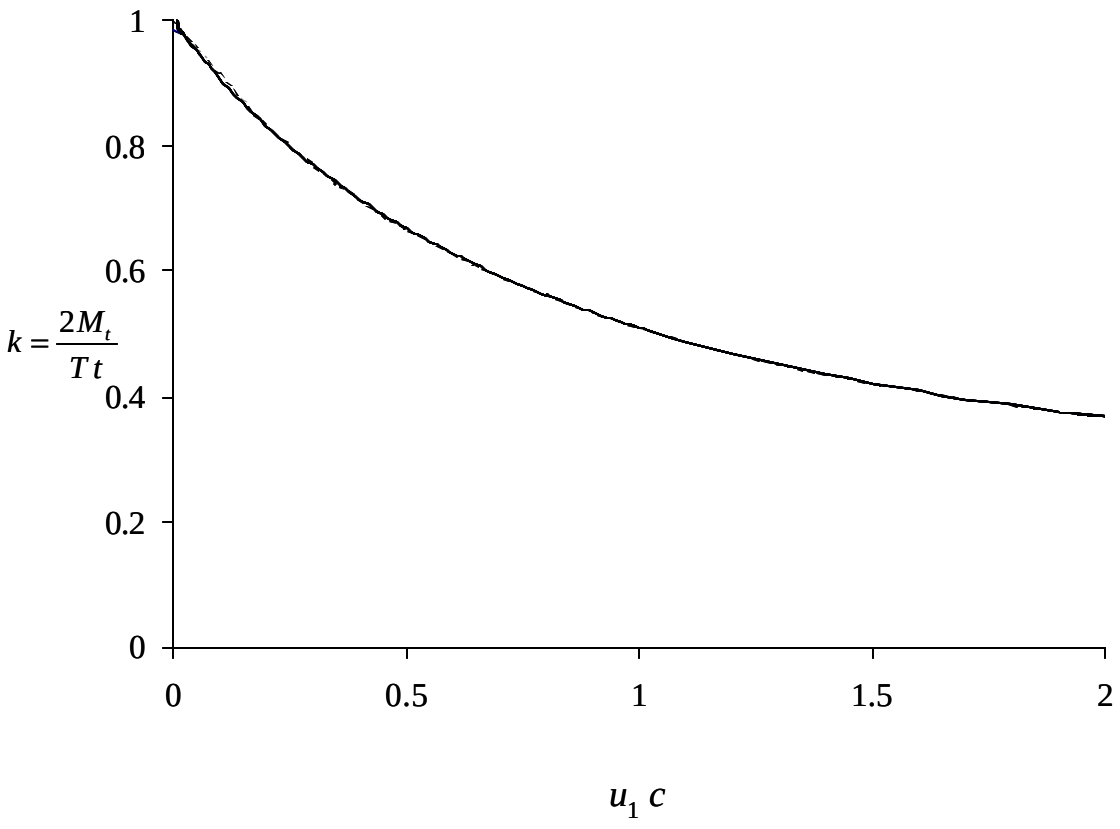

(c)

Figure 5.4 The normalized edge moment as function of normalized load u_1c with variation of ξ for clamped conditions of three typical adherend lengths. The dashed lines stand for the solution of Goland and Reissner. (a): Short unsupported adherend (L/c=1). (b): Intermediate unsupported adherend (L/c=5). (c): Long unsupported adherend (L/c=10).

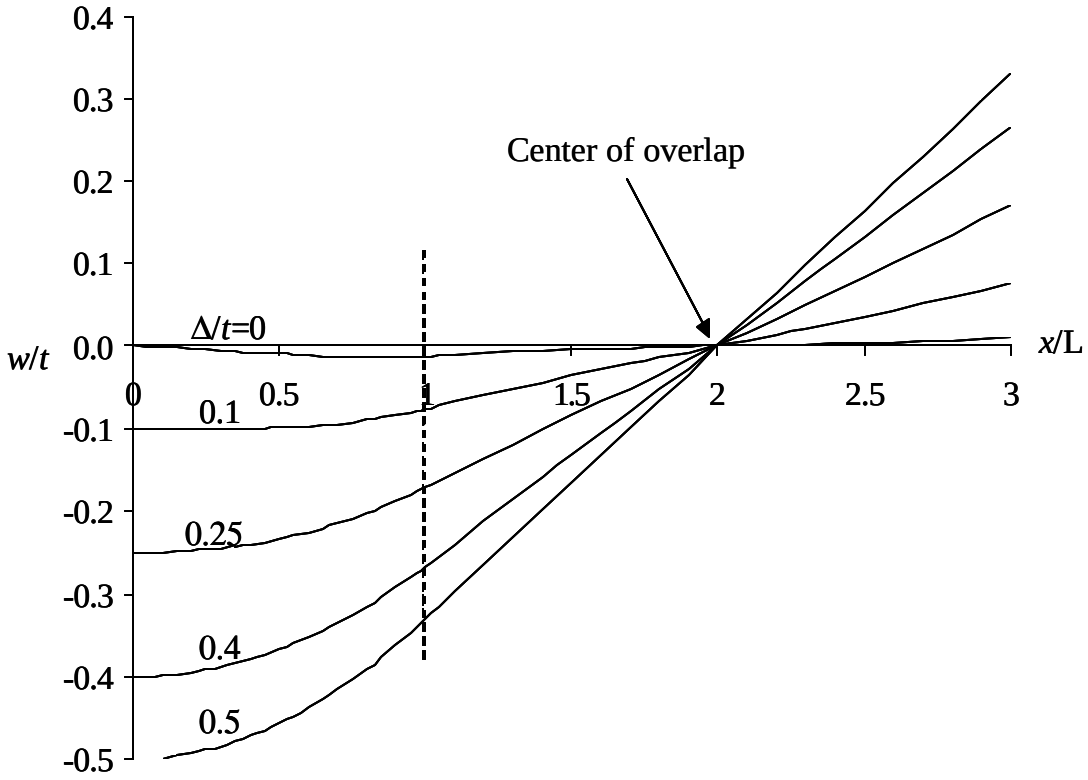
0.4
0.3
0.2
0.1
0.0
-0.1
-0.2
-0.3
-0.4
-0.5
w/t
Center of overlap
Δ/t=0
0.1
0.25
0.4
0.5
0
0.5
1
1.5
2
2.5
3
x/L

(a)

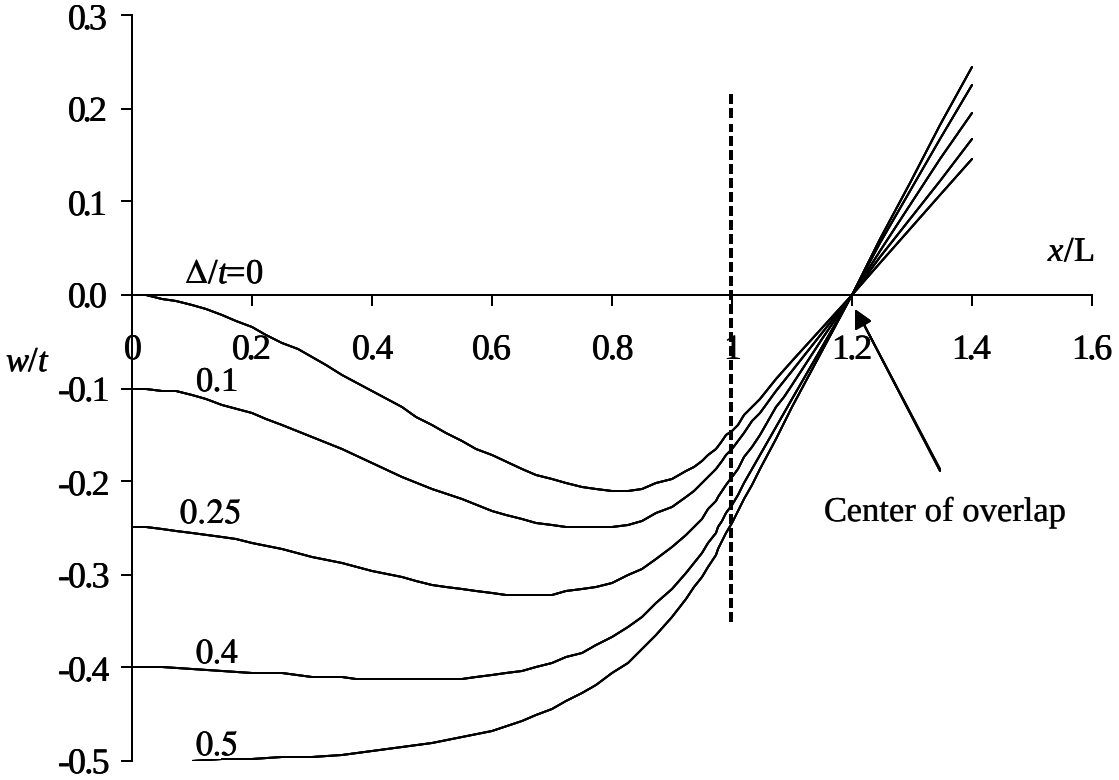
0.3
0.2
0.1
0.0
-0.1
-0.2
-0.3
-0.4
-0.5
w/t
0
0.2
0.4
0.6
0.8
1
1.2
1.4
1.6
x/L
Δ/t=0
0.1
0.25
0.4
0.5
Center of overlap

(b)

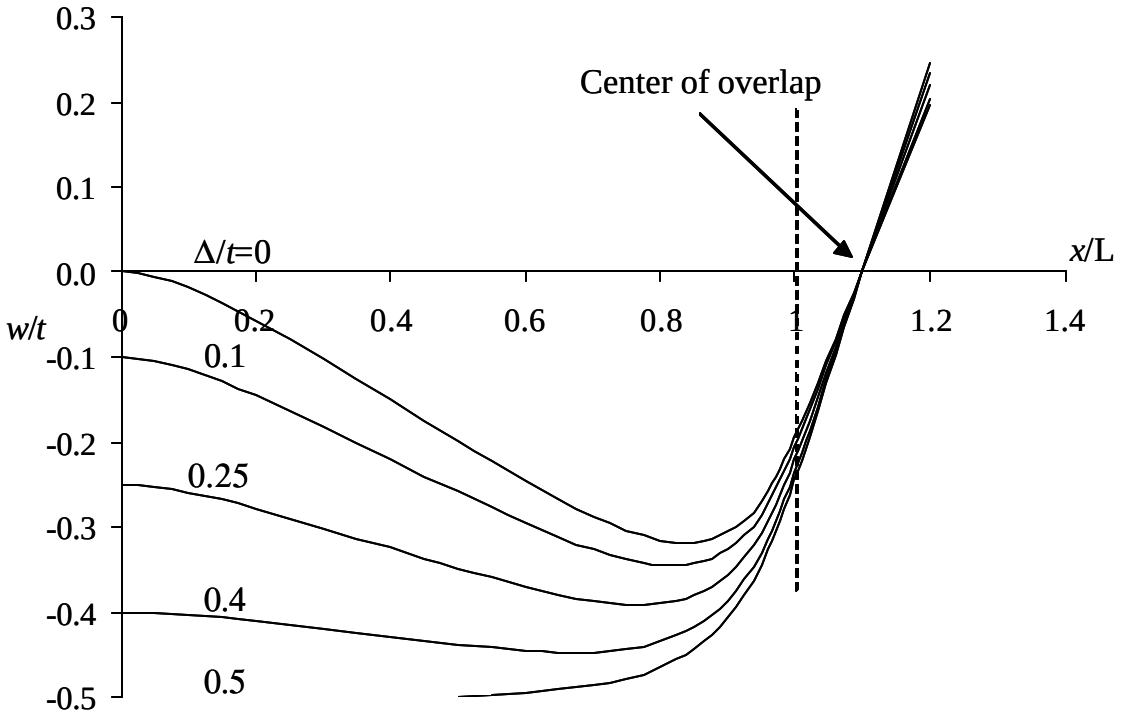

(c)

Figure 5.5 Transverse deflections for different boundary conditions. The dotted lines indicate the position of joint edge. (a): Short unsupported adherend (L/c=1). (b): Intermediate unsupported adherend (L/c=5). (c): Long unsupported adherend (L/c=10).

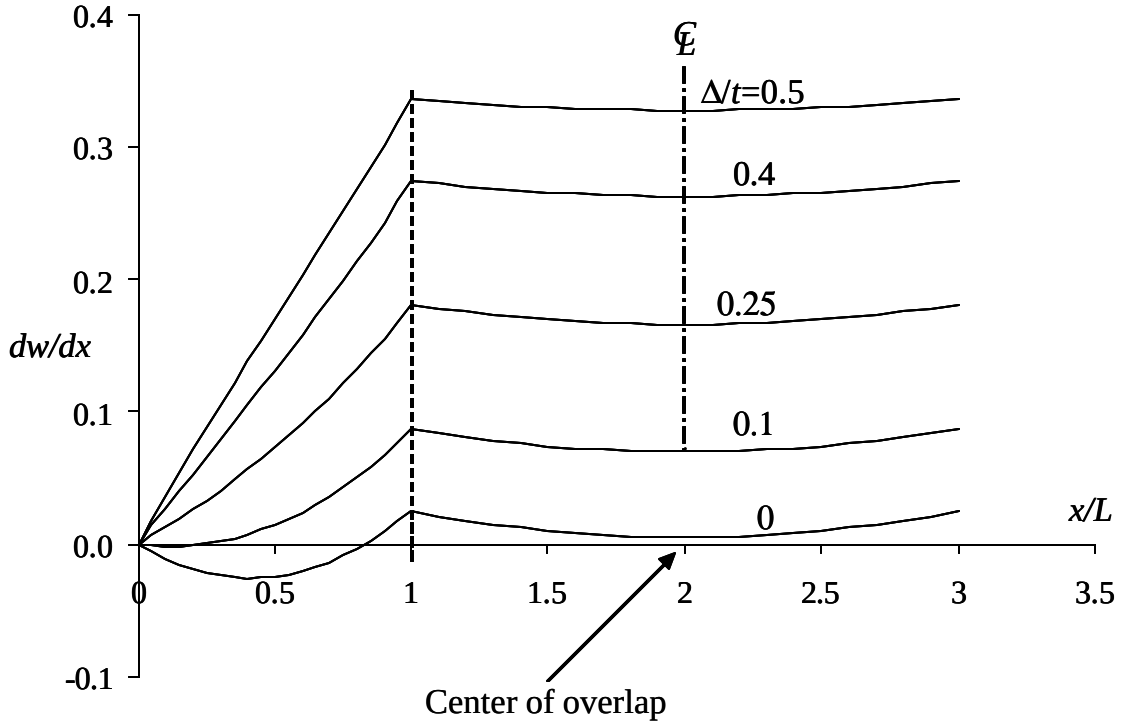
0.4
0.3
0.2
0.1
0.0
-0.1
dw/dx
0
0.5
1
1.5
2
2.5
3
3.5
x/L
℄
Δ/t=0.5
0.4
0.25
0.1
0
Center of overlap

(a)

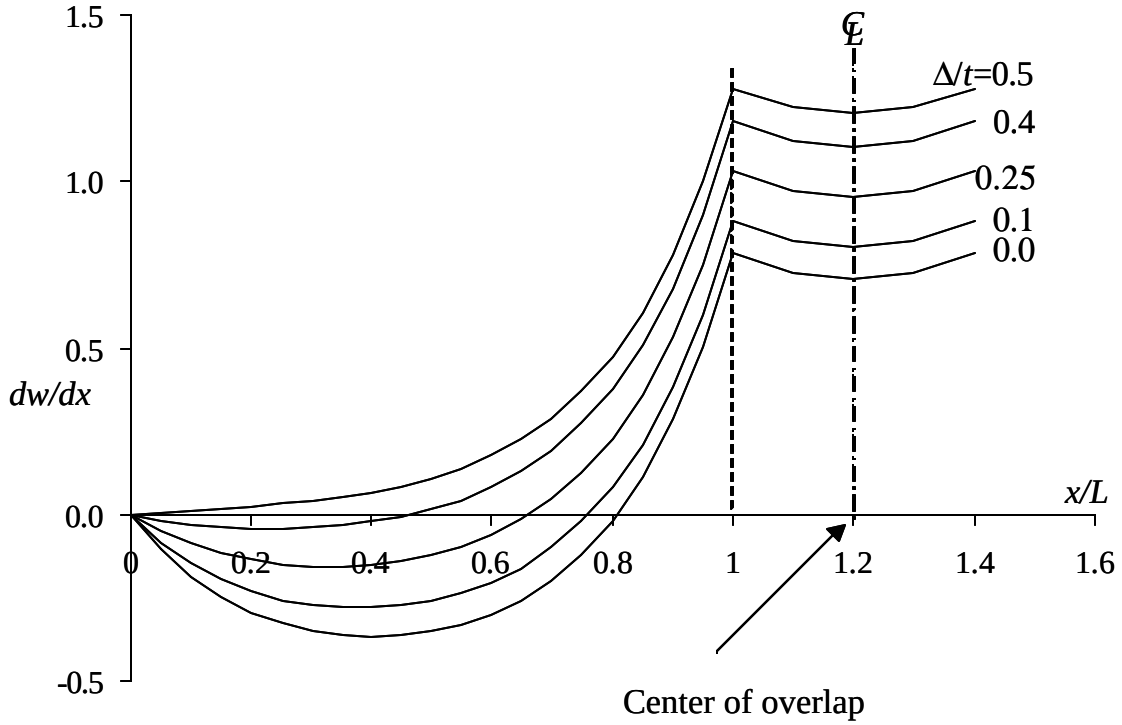
1.5
1.0
0.5
0.0
-0.5
dw/dx
0
0.2
0.4
0.6
0.8
1
1.2
1.4
1.6
x/L
℄
Δ/t=0.5
0.4
0.25
0.1
0.0
Center of overlap

(b)

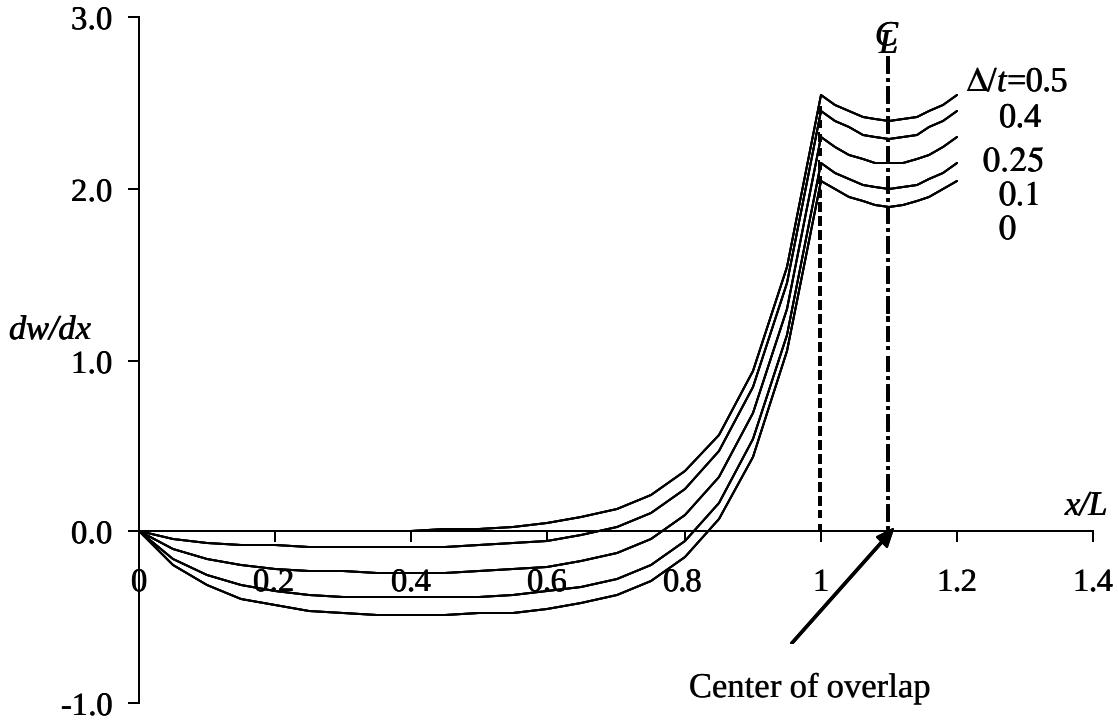

(c)

Figure 5.6 Rotations along the specimen for different boundary conditions. The dotted lines indicate the position of joint edge. (a): Short unsupported adherend (*L*/*c*=1). (b): Intermediate unsupported adherend (*L*/*c*=5). (c): Long unsupported adherend (*L*/*c*=10).

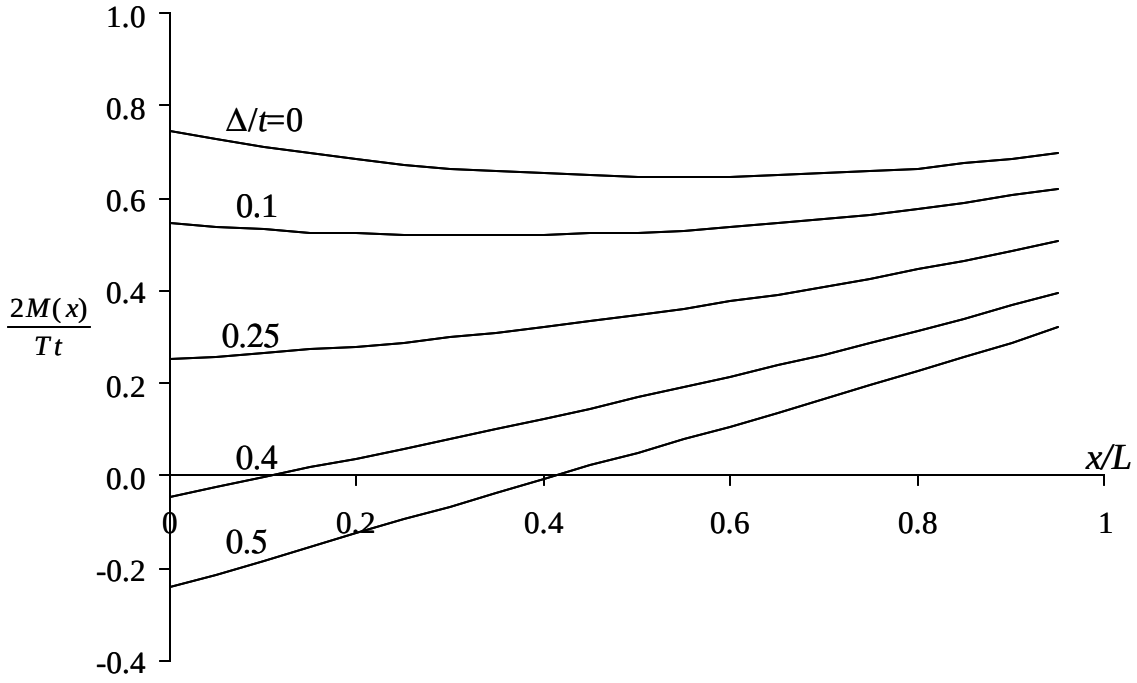

(a)

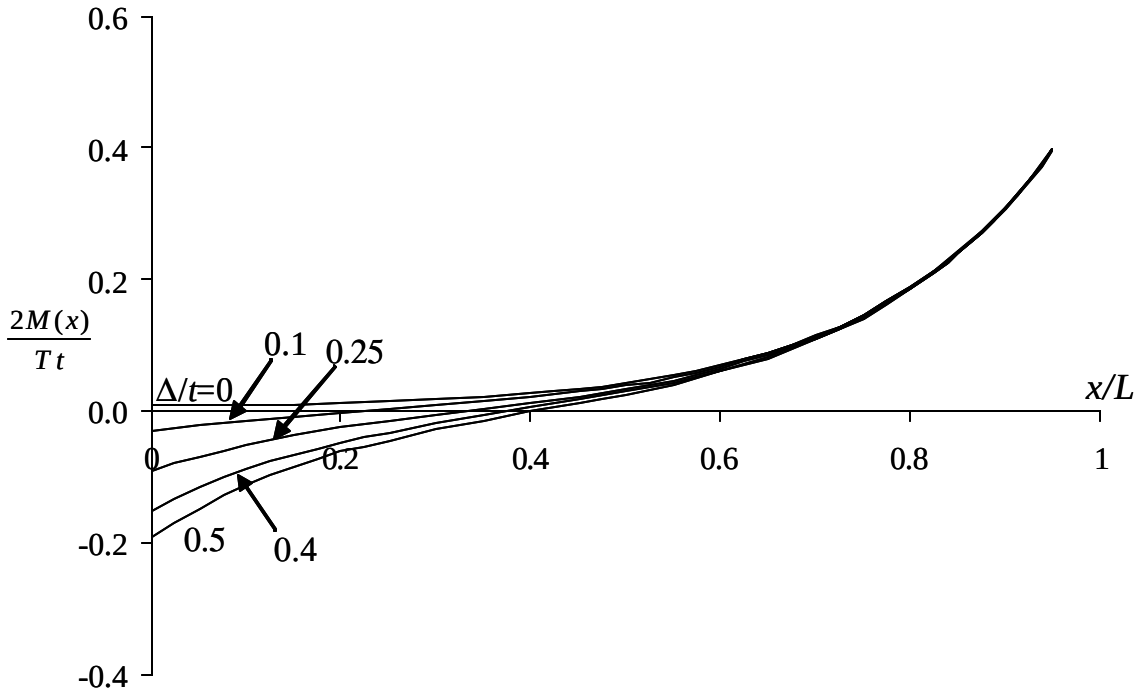

(b)

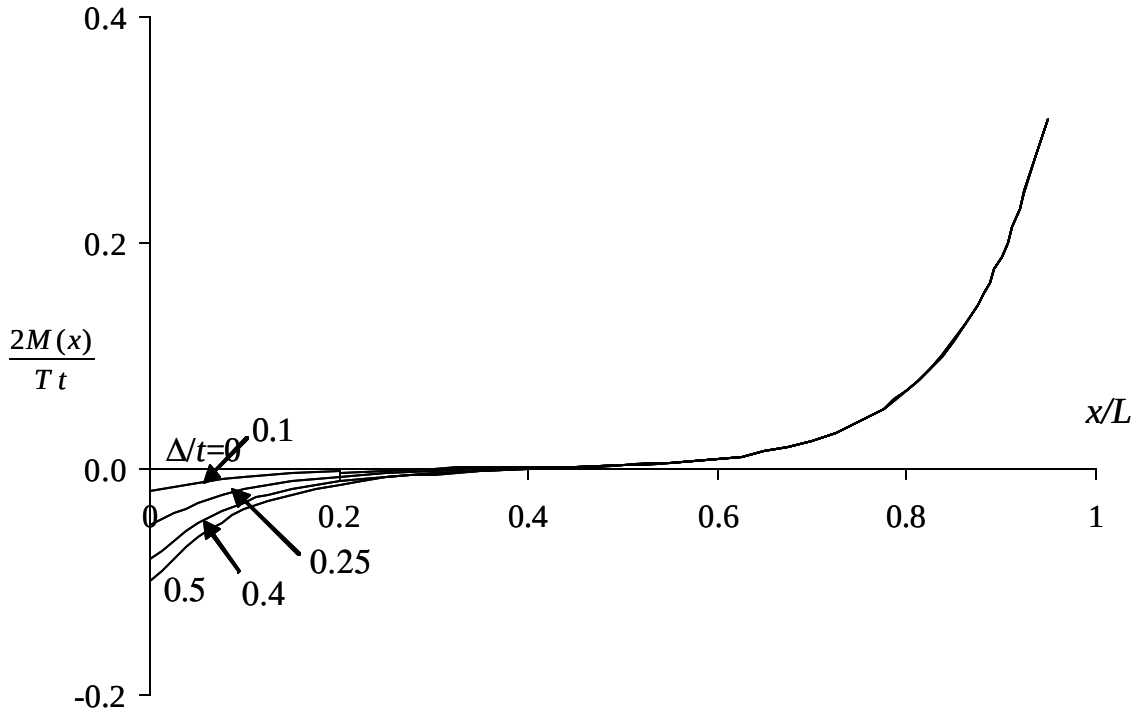

(c)

Figure 5.7 Comparison of bending moments for different gripping conditions. (a): Short unsupported adherend (L/c=1). (b): Intermediate unsupported adherend (L/c=5). (c): Long unsupported adherend (L/c=10).

CHAPTER 6

CONCLUSIONS

6.1 Summary

Polymers have been used in electronics applications for a long time, and are still gaining much attention because of their unique properties. Epoxy resin systems are used extensively in such diverse as matrix resin for printed circuit board, die-attach adhesives, and encapsulants for different levels of packaging. Adhesion between polymeric materials and various kinds of inorganic, even polymer materials, and the corresponding durability property against environmental attack of the bonded structures are among the key requirements for such materials for their successful service application. Subcritical failure of the adhesively bonded devices is very common in the products composed of different materials, and the initialed debond may propagate with subjected to both mechanical stress and environmental attack. Furthermore, due to involving materials of different mechanical and thermal properties, thermal residual stresses are often present in the multi-material system after fabrication and during service life. Many methods have been proposed to measure the residual stress, and blister test is especially useful for the system with thin film and coatings.

In this dissertation, we have tried to generate an in-depth understanding of the mechanics of adhesively bonded systems, which may provide insights to the application of polymers in the electronics industry. Four relatively independent topics were explored in this dissertation: subcritical debond propagation along an epoxy/glass interface; effect of residual stress on the strain energy release rate in a wedge specimen; bending to stretching analysis of a blister specimen with residual stresses; boundary conditions of a single lap joint specimen. The following sections summarize this research, detail some of the findings, and suggest some future work related to this study.

6.2 Conclusions

6.2.1 Water assisted crack propagation along the epoxy-glass interface

We have used wedge tests to measure the water-assisted subcritical crack growth velocity along a proprietary epoxy/glass interface. Two testing methods were conducted: *in situ* tests and *ex situ* (preconditioned) ones. The *in situ* testing results do not illustrate the typical stress corrosion cracking behavior. The investigation of residual stress and observation of crack blunting in the *in situ* tests at elevated temperatures (up to 60°C) qualitatively reveals that, the evolution of residual stress during testing and crack blunting due to plastic deformation in the vicinity of crack front cause the crack cease unexpectedly, and threshold value of strain energy release rate G_{th} and debond velocity don't present temperature dependence. A modified *ex situ*, or pre-conditioned wedge test was conducted to investigate the effect of moisture concentration along the epoxy/glass interface on G_{th}. The testing results from three temperatures all show that G_{th} decreases with preconditioning time and temperature accelerates this degradation process. Based on the thermal activation barrier concept, a model was developed to capture the mechanism. This model takes account of primary variables in this system: geometry, interfacial diffusion coefficient, activation energy, pre-conditioning time, and residual stress.

6.2.2 Thermally induced strain energy release rate in a wedge test specimen

The energy release rate, G_T, associated with thermal residual stresses in a wedge geometry is found to be a constant independent of debond length. However, the nature of the residual stress determines the value of the value G_T. Because the curvature of a bimaterial beam was used to characterize residual stress in the method proposed in this work, it is especially useful for the situation in which residual stress changes during the experiments, such as measuring subcritical debond propagation of the bonded structures with the existence of moisture or solution at elevated temperatures.

6.2.3 Residual stress in blister specimen

The deformation and delamination behavior of a circular blister under both uniform pressure and central rigid shaft load were investigated over a wide range of transverse loadings and initial in-plane uniform tensile stresses. The study showed that if the blister is really thin or flexible, stretching is dominant, thus the residual stress can be ignored for G calculation using either measured load or displacement data. However, when bending or bending-to-stretching transition behavior is present during the debonding process, the residual stress must be taken into account, and the correct equations should be adopted for measuring the adhesion energy. The proposed solutions for the pressurized blister geometry fit well with FEA results, thus can be applied in practice safely. Although the solutions for the central point loaded case don't demonstrate promising agreement with numerical predictions due to poor profile assumption, the qualitative trend can still be obtained using them.

6.2.4 Influence of gripping conditions in single-lap joints

In Chapter Five a closed form, geometrically nonlinear solution was reported to describe a single-lap joint specimen with a practical clamping condition where a spacer is inserted between the grips and specimen. The solution is derived based on the beam-column approach developed by Goland and Reissner. The transverse deflection and bending moment along the specimen and at the transition section were emphasized although the stress distribution along the bondline could have been obtained. It is found that adding a spacer tends to reduce the deflection of the specimen, and produce a negative reactive moment. However this effect is only of concern when the grips are located very close to the joint edge, or the applied load is small.

6.3 Future directions

6.3.1 Subcritical crack propagation

The study in this dissertation indicated that residual stress in the wedge specimens caused by CTE mismatch between the epoxy adhesive and glass substrates has a

significant influence on the measurement. Although some related qualitative analysis was given, more extensive work needs to be conducted along this direction.

The surface pretreatment prior to bonding is believed to enhance the joint durability significantly. For ceramic substrate materials the application of silane coupling agents (SCA) is a popular and valid treatment technique for the strength and durability enhancement of the interface. Therefore, the work to study the effect of such method on the behavior of subcritical crack propagation along the adhesive-substrate interface would be worthwhile both fundamentally and practically.

6.3.2 Residual stresses in thin-film systems

The actual residual stresses in a structure containing thin films are always in a non-uniform state, thus the study of the unequal bi-axial tensile stress and in-plane shear stress affect the measurement would be more useful. The compressive residual stress could be found in some thin-film specimens, and it would be very interesting to see how the compression affects the behavior of the blister specimen.

The method based on the principle of virtual displacements requires the presumed deflection profile, but the solutions of linear, small deformation that are used in this study cannot be successfully extended to nonlinear cases, thus significant disagreement was observed in delamination results. If more accurate expressions can be found to represent the deflected shapes of blisters on subject to both hydrostatic pressure, or rigid shaft load, the energy method can be applied more effectively because it provide an explicit and simple solutions that should attract the engineering researchers.

6.3.3 Boundary conditions in the single-lap joint geometry

As more and more composite materials are used to replace traditional monolithic materials, the material properties that are able to reflect such materials are more important. Anisotropy is one important feather of the composite, and its effect on the performance of SLJ received a limited attention to date.

The effect of any boundary conditions on the single-lap joint would work through changing the stress state in the structure. The work on stress distribution would be a reasonable extended work. The analytical solutions with numerical results, such as that obtained with FEA, would provide a valid way to verify the analytical solution, and find the errors.

Vita

Shu Guo was born on November 26, 1969 in Shanxi, China. He received his B.S. degree in Civil Engineering in July 1992 and his M.S. degree in Engineering Mechanics in April 1995, both from Zhejiang University, China. After graduation, he enrolled in the doctoral program in Engineering Science and Mechanics at Virginia Tech, working under the guidance of Professor David A. Dillard. He completed his doctoral program requirements in August, 2003.